UNIVERSITÀ DI VENEZIA CÀ FOSCARI

SCUOLA DOTTORALE DI ATENEO

GRADUATE SCHOOL

DOTTORATO DI RICERCA IN SCIENZE E GESTIONE DEI CAMBIAMENTI CLIMATICI

CICLO XXVIII - ANNO 2016

Stream di Climatologia Dinamica

PATH INTEGRAL, FOKKER-PLANK EQUATION AND TRANSITION MATRICES IN CLIMATE DYNAMICS

SETTORE SCIENTIFICO DISCIPLINARE DI AFFERENZA: FIS/06

Candidato: Giovanni CONTI (matr. 956002)

PhD Coordinator: Prof. Carlo BARBANTE

Tutore: Prof. Antonio NAVARRA

ABSTRACT

The Stochastic Ordinary and Partial Differential Equations turn out to be a very important tool in the understanding and modeling the Climate System. The resolution of this kind of problems is far from trivial. The only meaningful quantities are those derived by ensemble mean over the noise using the probability density function of the problem computed . In order to address these issues, three different methods of investigation are presented.

The first one is inspired by the Statistical Mechanics and Quantum Field Theory. Its power resides in the fact that it introduces a generating functional, from whom, using functional differentiation, all the n-points functions of the problem can be found. This technique has been used in Navarra et al. (2013b) to find correlation and variance of a (0d+1) simple model of ENSO with stochastic forcing. In this work, I have applied this method to a more complicated system, (2d+1), described by the Stochastic Barotropic Vorticity Equation into a channel. Periodic boundaries in the longitudinal direction and rigid walls bounding the channel to the north and south are used. I have solved the problem of finding the generating functional and I have used it to get analytical expressions for variance and correlation functions. I have presented here the study for three configurations of the Stochastic Barotropic Vorticity Equation, obtained adding or neglecting damping and mean flow. I have shown that this technique is applicable but with many technical difficulties. For this reason I have preferred to use a simple ENSO model to test the other two techniques and to study in depth ENSO itself.

The second method is based on the resolution of the Fokker-Planck equation related to the stochastic system via eigenfunctions expansion. The ENSO model studied has been derived using a rotation in the space of variables of the Recharge Oscillator. It is suggested a new way to consider ENSO, as a system that can jump between two states, one positive and one negative, represented by a double potential wells which arise by the non-linearity that damps the system. The jumps are possible thanks to the stochastic fluctuations. It is suggested a possible mechanism that could explain the asymmetry in the Sea Surface Temperature Anomalies probability density function in the ENSO zone. In particular, taking into account the MJO effect, the double well potential is modified becoming asymmetric producing an asymmetric probability density function for the anomalies. Using this model, exploiting a periodic growth rate, also the possible cause of the predictability barrier is studied, another important feature of ENSO.

The investigation prompted the idea that ENSO could be a system described by a sequence of state, rather than a simple oscillation. To check this idea, the third method has been introduced. It shows how the transition probability matrices can be used to deal climatic phenomena. Temperature anomalies are divided into four blocks, states, and the probability to move from one state to another has been calculated both for observations and General Circulation Model. In particular, these matrices have been used to define a predictability index of ENSO using their entropy. Not only the long-time seasonal PDF could be checked, but also the single transitions for different states in different periods.

CONTENTS

LIST OF FIGURES

LIST OF TABLES

Acknowledgment:

I wish to remind all those who helped me in the writing of the thesis with suggestions, criticisms and comments: to them goes my gratitude, though I am responsible for any error contained in this thesis.

I first thank Professor Antonio Navarra, my advisor, for introducing me into a fascinating world. Without his support, his wise and expert guidance, this thesis would not exist.

My sincere thanks also goes to Dr. Joe Tribbia, for interesting tips and support during the period of study at NCAR that allowed me to focus on an important part of the thesis. Thanks for his comments and suggestions in the revision of the document.

I would like to thank also Professor Valerio Lucarini for having revised my thesis and spent encouraging words on the work done.

Thanks go to all the professors and researchers of the CMCC. They taught me new things with great competence and have allowed me to address, with a different awareness, the problems treated in the thesis.

Thanks to my fellow travelers in the Ph.D. world: Elena Argiriadis, Irene Mavilia, and Daniele Peano. Solo adventure would not have been so funny.

Special thanks go to the person dearest to me, my wife Sarah, for the support and forbearance.

CHAPTER 1

INTRODUCTION

Some of the most important aspects that strongly characterize weather and climate are variability and chaos. The equations that govern the evolution of the atmosphere and the ocean have been known for a long time and they have been extensively investigated. These equations showed a strong sensitivity to small perturbations, both in the initial conditions and in the parameters that define them, giving rise to the entire field of dynamical chaos (Lorenz, 1963). The temporal and spatial scales, associated with changes in weather and climate, include a wide range of values. For example, tornados are characterized by spatial scales of a few hundred meters and time scale of the order of the hour, or planetary waves with a time scale of months and spatial scales of the order of tens of thousands kilometers. Other climatic phenomena, that can appear as fluctuations in specific patterns of pressure and temperature on Earth, can be identified only with annual, decadal or multi-decadal time scales.

It is now well known that important variations in atmospheric and oceanic circulation in some regions may actually be the result of a connection with specific variations of atmospheric variables that happen in a different part of the Earth, as happens for El Niño Southern Oscillation (ENSO). This phenomenon is a large scale oceanic warming in the tropical Pacific Ocean correlated to a see-saw in the tropical sea level pressure between the western and eastern Pacific, that dramatically affects the Earth's climate

on a global scale.

The chaotic nature of the dynamics has stimulated the application of methods and ideas derived from statistics and statistical dynamics. For instance, to make weather predictions, extensive ensemble systems are recently used, that are designed to sample the phase space around the initial conditions. Such an approach has been shown to substantially improve the usefulness of the forecasts, allowing forecasters to issue probability-based forecasts. The implicit assumption is that the presence of various sources of errors, coupled with the intrinsic sensitivity of the evolution equations to small errors (Lorenz, 1963), makes a single forecast not very useful (Epstein, 1969; Leith, 1974). Ensemble experiments are now commonly used in numerical experiments driven by external forcing, like those used with prescribed SST (Sea Surface Temperature) or even prescribed concentration of greenhouses gases in climate change experiments, (Rodwell and Doblas-Reyes, 2006; Toth and Kalnay, 1993). These works have been modifying the dominant paradigm of interpretation of the evolution of atmospheric flows (and to some extent also of the ocean, see (Pinardi et al., 2008)), attributing more and more importance to the probability distribution of the variables of interest rather than to a single representation. Chaos is an important aspect when the equations of the atmosphere and ocean are considered, even if it is not the only one.

It has been shown (Hasselmann, 1976) that "the slow climate variability can be explained as the response to continuous integral random excitations due to short-term weather disturbance". Stochastic Partial Differential Equations (SPDE) seem to be a basic tool for modeling climate systems. The deterministic climate/weather evolution equations with a stochastic component can be considered to correctly describe some aspects of the atmosphere in mechanical models (Farrell and Ioannou, 1995; DelSole, 2001; Penland, 2003; Duane and Tribbia, 2004; Schneider and Fan, 2007; Sura and Newman, 2008). Extensive works have been done also in estimating the stochastic component from observations (Kravtsov et al., 2005; Gritsun and Branstator, 2007).

The main goal of this work is to study ENSO, as a model system to test these ideas and methods. Because of ENSO irregularities, that let suppose the presence of a stochastic forcing component, this study is conducted using stochastic equations to describe the system. These mathematical entities are closely linked to a deterministic evolution equation for the Probability Density Function (PDF) of the system, namely

the equation of Fokker-Planck (FP). In this way it is possible to study directly the only real fundamental quantity, from which all the statistical information needed to describe the system under consideration, as the mean, variance, skewness and correlation function, could be derived. For such a system, the only meaningful variables are those found using ensemble averages over the noise. If you could find a generating function as in Statistical Mechanics, all the interesting quantities could be written using a simple derivation.

The analytical analysis of this kind of equations is far from trivial. Hochberg et al. (1999) showed how, from the formal solution of the FP equation, associated to a generic SPDE, it is possible to derive a generating functional, which can be written in terms of Path Integral (PI). This generating functional is analogous to the one well known in Quantum Field Theory (QFT), by using functional differentiation on it, one can obtain all the meaningful quantity describing the stochastic system. Fortunately, as it often happens, it is possible to apply the formalism and technology already developed in a particular branch of physics, to treat different problems. The application of this framework to the dynamics of ocean and atmosphere could lead to important results. This method has been used in (Navarra et al., 2013b) to find correlation and variance of a (0d+1) simple model of ENSO with stochastic forcing. In this work, I have applied this method to a more complicated system, (2d+1), described by the Stochastic Barotropic Vorticity Equation (SBPVE) into a channel. The periodic boundary condition in the longitudinal direction has been considered. This problem could be considered as a starting point to study a more complex model of ENSO with stochastic forcing in a future work. The simplest (2d+1) system of equations that is able to describe the equatorial dynamics is the Shallow Water Equations (SWE), from which, using the QG approximation, the Barotropic Vorticity Equation can be derived. The effect of the boundary reflections can not be seen using the channel structure, but I have solved the problem of finding the generating functional and I have used it to get analytical expressions for variance and correlation functions. In general with this method I have been able to find all the n-points functions of the problem. I have presented here the study for three configurations of the SBPVE, obtained adding or neglecting damping and mean flow. I have shown that this method is applicable to the SBPVE but with many technical difficulties, even if the interesting analytical expressions for variance and correlation functions have been found.

The ENSO model has been extensively studied. The works written about it can be loosely grouped into two big frameworks: a deterministic one, for example (Cane and Zebiak, 1985; Cane et al., 1986; Zebiak and Cane, 1987) and a stochastic one. Both frameworks involve a positive ocean-amosphere feedback (Bjerknes, 1969). Bjerknes hypothesized that an initial positive Sea Surface Temperature Anomaly (SSTA) in the equatorial eastern Pacific reduces the east-west SST gradient and hence the strength of the Walker circulation, resulting in weaker trade winds around the equator. The Walker circulation is the typical wind circulation across the tropical Pacific Ocean. It can be schematized as rising air in the tropical western Pacific, upper-level winds blowing from the west to the east, and the sinking air returned back to the surface in the tropical eastern Pacific. The reduction of SST gradient and the weakening of the Walker circulation drive the ocean circulation changes that further reinforce SSTA. This positive ocean-atmosphere feedback leads the equatorial Pacific to a warm state, i.e., the warm phase of ENSO called El Niño.

In the former case, ENSO is seen as a self-sustained, naturally oscillatory mode of the coupled ocean-atmosphere system (Wang et al., 2012). Several mechanisms, able to reproduce the basic characteristic of ENSO, have been proposed for this deterministic oscillation, explaining the dynamics in terms of delayed oscillator (Schopf and Suarez, 1988; Suarez and Schopf, 1988; Battisti and Hirst, 1989; Philander, 1990; Jin and Neelin, 1993; Neelin et al., 1994; Tziperman et al., 1994a; Jin et al., 1994a; Neelin et al., 1998), in terms of a recharge mechanism (Jin, 1996, 1997a), in terms of advective-reflective oscillator (Picaut et al., 1997) and other conceptual models. These models basically differ in the negative feedback used to limit the growth of the oscillation, respectively using reflected Kelvin waves, discharging process due to Sverdrup transport, or anomalous zonal advection. Wang (2001) showed the existence of the unified oscillator model that includes the physics of all oscillator models discussed above.

Since the ENSO indices present lots of irregularities, changes of phase and intensity, the second framework was proposed. In this view, ENSO is considered as a stable or damped mode interacting with stochastic forcing, in particular a linear system forced by noise is used (Penland and Sardeshmukh, 1995; Moore and Kleeman, 1999b,a; Thompson and Battisti, 2000, 2001; Penland, 1996). Some authors (Tziperman et al., 1994a; Jin et al., 1994a) suggested that all those irregularities could be the manifesta-

tion of the quasi-periodic route to chaos. The natural oscillator (a delayed oscillator) of the equatorial Pacific Ocean could non-linearly interact with the seasonal cycle and manifests non-linear resonance at several periods of the oscillator. The jumps between these periods result in chaotic behaviour. However, Stone (1998) showed that the same natural oscillator, driven by natural environmental fluctuation, could explain aperiodicity and chaos in the ENSO index, and it also results in burst and change of regime, common in the more complex ENSO model.

Probably the right framework and mechanism is a mixture of both (Chang et al., 1996; Philander and Fedorov, 2003). However, Jin, (Jin, 1997b), showed that the model containing a time delay can not be derived theoretically from a shallow water model with the wind forcing (with the addition of a further equation which takes into account thermodynamics), if not ignoring the boundary east of reflection, in practice ignoring the South America, that is really a strong assumption.

For these reasons, the second method used to study ENSO is based on a model with a lower dimensionality that contains the positive Bjerknes feedback, non-linearity and stochastic forcing. Part of these results have been published in (Navarra et al., 2013a). The Recharge Oscillator with the non-linear damping term and noise has been considered as a starting point. From this model with a rotation in the space of variables, one single stochastic equation has been obtained. The associated FP equation has studied by eigenfunctions expansion. A new way to consider ENSO is suggested. It can be seen as a system that can jump between two states, one positive and one negative, thanks to the stochastic forcing. These two states are represented by a potential generated by the non-linearity that damps the system. In this framework, the natural way of thinking is the one that refers to the potential that arises from the drift term of the FP equation. Using this tool, it has been shown that the Madden-Julien Oscillation (MJO) (Madden and Julian, 1971b) can be considered at least one of the causes that generate the asymmetry in the PDF that characterize SSTA of the ENSO region. It has also been shown that a periodic growth rate is able to produce the predictability barrier that affects this phenomenon. Usually the coupling parameter introduced in all these models assumes values that allow the system to oscillate. Even if the damped oscillations are not considered, this simple model shows that also a strong coupling between atmosphere and ocean, that would bring to decay oscillation, by means stochastic fluctuation, would

allow again a finite motion between two stable points.

Although I have used additive noise as stochastic component, it has not been advocated as the only forcing mechanism for ENSO. However, the used framework is completely general and allows a theoretical investigation of various kind of noise, additive, or multiplicative, or colored that can be involved to developed a fully ENSO theory.

The investigation prompted the idea that ENSO could be a system described by a sequence of state, rather than a simple oscillation. For this reason, I have presented a third method of study. Temperature anomalies are divided into four blocks, states, and the probability to move from one state to another has been calculated both for observations and General Circulation Model (GCM). Transition probability matrices for the ENSO process has been built in this way highlighting which were the most likely transitions, with the changing seasons, and which ones, if not forbidden, very rare. From these matrices, it is possible to build a Markovian process allowing the study of the mean sojourn time and variance for the four states. Comparing the matrices obtained from the observations and from the model, I have been able to classify the capability of numerical model to reproduce and make good forecast of ENSO. This kind of comparison has been done using the CMCC-CMS couple model, (Davini et al., 2013), that is a Coupled General Circulation Model (CGCM). I have used a 500-years simulation to build the matrices.

One of the most interesting things that emerge from this kind of analysis is the so called Spring Predictability Barrier (SPB), the reduced capability to make good forecast passing through the spring, that in some way evens out the possibility to go in any state. I have suggested a way to define a predictability index based on the entropy of these matrices.

In chapter 2, the PI method and the results inherent the SBPVE in a channel are presented. In chapter 3 and 4, it is shown the simple rotated model of ENSO with whom it is investigated, by means the FP equation, the possible mechanisms that could explain the asymmetry that characterizes SSTA of the ENSO region, and the one that produces the predictability barrier that affects this phenomenon. In chapter 5, it is shown the work on the transition probability matrices, how they have been found and how they can be used to characterize ENSO and compare model with observations. It is

also suggested a way to define a predictability index. In chapter 6 the conclusions are shown.

CHAPTER 2

PATH INTEGRAL AND THE STOCHASTIC BAROTROPIC VORTICITY EQUATION

2.1 Introduction

Some of the peculiar features of climate and weather are variability and chaos. The Lorenz's works (Lorenz, 1963, 1984, 1987), to quote some of them, have marked a fundamental step in the history of the last century physics. Chaos is an important aspect when the equations of the atmosphere and ocean are considered, even if it is not the only one.

The study of the equations of atmosphere, ocean and their interaction, requires approximations deducted from the spatial and temporal scales of the phenomenon under study. For some of them, the non-linear effects, proper of the dynamical equations, can be considered as a disturbance, a stochastic forcing. It has been shown (Hasselmann, 1976) that " the slow climate variability can be explained as the response to continuous integral random excitations due to short-term weather disturbances". The deterministic climate/weather evolution equations with a stochastic component can be considered to correctly describe some aspects of the atmosphere in mechanical models (Farrell and Ioannou, 1995; DelSole, 2001; Penland, 2003; Duane and Tribbia, 2004; Schnei-

der and Fan, 2007; Sura and Newman, 2008), and extensive works have been done also in estimating the stochastic component from observations (Kravtsov et al., 2005; Gritsun and Branstator, 2007). Hartmann (2001) used a stochastic linearized barotropic model to investigate the relationship between wind variation associated to the Madden Julien Oscillation (MJO), and the eddy kinetic energy in the tropics. Another important effect that a stochastic forcing can have, is the generation of the zonostrophic instability (Srinivasan and Young, 2012).

The Stochastic Partial Differential Equations (SPDE) seem to be a basic tool for modeling climate systems. It is clear that for such a system the only meaningful variables are those found using ensemble averages over the noise. If you could find a generating function as in Statistical Mechanics, all the interesting quantities could be written using simple derivations.

The analytical analysis of this kind of equations is far from trivial. It has been presented (Martin et al., 1973) a formalism to write SPDE as a field theory formulated using the Path Integral, (PI). Zinn-Justin (1993) have shown that the SPDE is associated to a Fokker-Plank (FP) equation, whose formal solution can be written in term of PI and can be used to write a generating functional. After these works, a simple way to extend this method and handle a generic SPDE has been shown (Hochberg et al., 1999, 2000a,b). This method has been used in (Navarra et al., 2013b) to find correlation and variance of a (0d+1) linear and non-linear simple model of ENSO with stochastic forcing.

In this work, I have applied this method to a more complicated system, (2d+1), described by the Stochastic Barotropic Vorticity Equation (SBPVE) into a channel. The periodic boundary condition in the longitudinal direction is used. This problem could be considered as a starting point to study a more complex model of ENSO with stochastic forcing in a future work. The simplest (2d+1) system of equations that is able to describe the equatorial dynamics is the Shallow Water Equations (SWE), from which, using the QG approximation, the Barotropic Vorticity Equation (BPVE) can be derived. The effect of the boundary reflections can not be seen using the channel structure, but I have solved the problem of finding the generating functional and I have used it to get analytical expressions for variance and correlation functions. In general with this method I have been able to find all the n-points functions of the problem. I have

presented here the study for three configurations of the SBPVE, obtained adding or neglecting damping and mean flow. I have shown that this method is applicable to the SBPVE but with many technical difficulties, even if the interesting analytical expressions for variance and correlation functions have been found.

For this work I have used Gaussian white noise, but the framework is generalizable to a generic kind of noise. It has been shown that the generating functional can be written in terms of particular Green's functions, and then the problem of finding the variance and correlation for the stochastic system has been basically traced back to find these Green's functions.

2.2 Method

The deterministic part of the equation object of this chapter, as mentioned in the introduction, is the barotropic vorticity equation in β plaining approximation

$$\frac{\partial}{\partial t}\nabla^2\psi + \mathcal{J}(\psi, \nabla^2\psi) + \beta\frac{\partial}{\partial x}\psi + \alpha^{-1}\nabla^2\psi = 0, \tag{2.1}$$

where $\mathcal{J}$ here indicates the Jacobian operator

$$\mathcal{J}(A, B) = \frac{\partial A}{\partial x}\frac{\partial B}{\partial y} - \frac{\partial A}{\partial y}\frac{\partial B}{\partial x}. \tag{2.2}$$

$\psi(\mathbf{x}, t)$ is the stream function, from which it is possible to recover the information about the zonal and meridional component of the wind by simple derivation

$$u = -\frac{\partial\psi}{\partial y} \tag{2.3}$$

$$v = \frac{\partial\psi}{\partial x}, \tag{2.4}$$

and the last two terms of Eq. (2.1) represent the effect of the Earth curvature and the Rayleigh damping, that is a damping that takes into account the effect of the surface friction and radiation. If U is a characteristic scale for the horizontal velocity, L the characteristic scale length for the system, then, ψ is scaled with UL , x and y are scaled with L, while t is scaled with $\frac{1}{\beta L}$, and the governing equation (2.1) after the scaling

becomes:

$$\frac{\partial}{\partial t}\nabla^2\psi + \epsilon\mathcal{J}(\psi, \nabla^2\psi) + \frac{\partial}{\partial x}\psi + \mu^{-1}\nabla^2\psi = 0\,. \tag{2.5}$$

Now all the variables are dimensionless and

$$\epsilon = \frac{U}{\beta L^2} = \left(\frac{\delta_I}{L}\right)^2 \tag{2.6}$$

$$\mu^{-1} = \frac{\alpha^{-1}}{\beta L} = \left(\frac{\delta_s}{L}\right). \tag{2.7}$$

The two parameters ϵ, and μ^{-1} measure the relative importance of non-linearity, and damping due to friction and radiation. Each of them can be written as a ratio between two length scales to some power (Pedlosky, 1996). The major atmospheric phenomena, like the large scale waves, have a characteristic horizontal scale of $L \approx 10^4$ km, $U \approx 10$ m s^{-1} and at high latitude the beta parameter is $\beta \approx 10^{-}11\ s^{-1}L^{-1}$. The typical value for the damping term is $\alpha \approx 10^{-6}\,s^{-1}$, that corresponds to eleven days. With this choice of the scale, $\epsilon \approx 10^{-2}$ and $\mu^{-1} \approx 10^{-2}$.

To simplify the computation, I have chosen a unique spatial scale, so $x \in [0,\ 1]$ and $y \in [0,\ 1]$. I have considered the structure of a channel, then the following boundary condition for ψ should be used

$$\psi(0, y, t) = \psi(1, y, t) \tag{2.8}$$

$$\psi(x, 0, t) = \psi(x, 1, t) = 0, \tag{2.9}$$

that means periodic boundary in the longitudinal direction and rigid wall at north and south of the channel.

Even if it is difficult to manage the full non-linear BPVE, it is possible to characterize the basic flow and consider a particular situation. This allows to linearize Eq. (2.5) around a mean flow. Introducing the decomposition,

$$\psi(x, y, t) = \bar{\psi}(\mathbf{x}, t) + \psi'(\mathbf{x}, t), \tag{2.10}$$

it is possible to characterize the flow as a background $\bar{\psi}(\mathbf{x}, t)$, plus a perturbation

$\psi'(\mathbf{x}, t)$. After the decomposition, Eq. (2.5) gets the following form:

$$\frac{\partial}{\partial t}\nabla^2\psi' + \frac{\partial}{\partial x}\psi' + \epsilon\Big(\frac{\partial}{\partial x}\psi'\frac{\partial^3}{\partial y^3}\bar{\psi} - \frac{\partial}{\partial y}\bar{\psi}\frac{\partial}{\partial x}\nabla^2\psi'\Big) + \mu^{-1}\psi' = 0\,,$$

If the background flow profile depends only on y, it is possible to write

$$\frac{\partial^3\bar{\psi}}{\partial y^3} = -\frac{\partial^2\bar{U}}{\partial y^2} \tag{2.11}$$

$$\frac{\partial\bar{\psi}}{\partial y} = -\bar{U}, \tag{2.12}$$

where $\bar{U}$ is the zonal mean velocity, and Eq. (2.5) becomes:

$$\frac{\partial}{\partial t}\nabla^2\psi' + \frac{\partial}{\partial x}\psi' - \epsilon\Big(\frac{\partial^2\bar{U}}{\partial y^2}\frac{\partial}{\partial x}\psi' - \bar{U}\frac{\partial}{\partial x}\nabla^2\psi'\Big) + \mu^{-1}\psi' = 0\,. \tag{2.13}$$

Eq. (2.13) is completely general, and it is correct for the whole class of stream functions, describing the basic flow, depending only on the y variable.

Note that the particular case of a constant mean flow, $\bar{U} = const$, can be traced back to an equation with zero zonal mean flow using a Galilean transformation; in fact, if the equation can be written as

$$\left[\frac{\partial}{\partial t} + \bar{U}\frac{\partial}{\partial x} + \mu^{-1}\right]\nabla^2\psi' + \frac{\partial}{\partial x}\psi' = 0, \tag{2.14}$$

using the Galielan transformation of variables

$$\begin{cases} t' = t \\ x' = x - \bar{U}t, \end{cases} \Rightarrow \begin{cases} \frac{\partial}{\partial x} = \frac{\partial}{\partial x'} \\ \frac{\partial}{\partial t} = \frac{\partial}{\partial t'} - \bar{U}\frac{\partial}{\partial x'}, \end{cases} \tag{2.15}$$

and then

$$\left[\frac{\partial}{\partial t'} \cancel{- \bar{U}\frac{\partial}{\partial x'}} + \cancel{\bar{U}\frac{\partial}{\partial x'}} + \mu^{-1}\right]\nabla'^2\psi' + \frac{\partial}{\partial x'}\psi' = 0. \tag{2.16}$$

The effect of stochastic forcing can be taken into account adding the noise $\eta(x, y, t)$ in the right hand side of Eq. (2.13). From now on, it is assumed that the noise is Gaussian and in particular white. This is to simplify the computation. Then it is possible to

characterize the noise writing:

$$\langle \eta(\mathbf{x},t)\rangle = 0 \tag{2.17}$$

$$\langle \eta(\mathbf{x},t)\eta(\mathbf{x}',t')\rangle = Q\delta(t-t')\delta(\mathbf{x}-\mathbf{x}')\,, \tag{2.18}$$

where Q is a constant that represents the strength of the noise correlation. Following Hochberg (1999), the Eq. (2.13) with stochastic forcing is

$$D\psi(\mathbf{x},t) = F\psi(\mathbf{x},t) + \eta(\mathbf{x},t) \tag{2.19}$$

where I have neglected the apex over the stream function, and

$$D = \frac{\partial}{\partial t}(\nabla^2 - \lambda^{-2}) + \frac{\partial}{\partial x} + \mu^{-1} \tag{2.20}$$

$$F = \epsilon\Big(\frac{\partial^2 \bar{U}}{\partial y^2}\frac{\partial}{\partial x}\psi - \bar{U}\frac{\partial}{\partial x}\nabla^2\psi\Big). \tag{2.21}$$

The separation in F and D is arbitrary, physics does not change. However, if you consider D as a linear differential operator involving arbitrary time and space derivatives (eventually linear terms in the field), while F is considered as an operator that can be linear or not (but it does not contain time derivatives), the computation of the PDF $P[\psi(\mathbf{x},t)]$, and the generating functional $\mathcal{Z}[\mathcal{J}]$, related to the system, presents less problems.

A particular FP equation, that governs the evolution for the PDF of the stochastic field $\psi(\mathbf{x},t)$, (Zinn-Justin, 1993; Hochberg et al., 1999), is associated to the stochastic Eq. (2.19), whose formal solution, in case of Gaussian white noise, is

$$P[\psi(\mathbf{x},t)] = \mathcal{N}\exp\left(-\frac{1}{2Q}\mathcal{S}(\psi(\mathbf{x},t))\right) = \mathcal{N}\exp\left(-\frac{1}{2Q}\int d\mathbf{x}dt\Big(D\psi(\mathbf{x},t) - F\psi(\mathbf{x},t)\Big)^2\right), \tag{2.22}$$

where $\mathcal{N}$ is a normalization constant and $\mathcal{S}$ can be considered as the action of the system. It is useful separating the two operators D and F now mixed into the action.

To do this, I have applied the so called *Hubbard-Stratonovich* transformation

$$\exp\left(-\frac{1}{2Q}\mathcal{S}(\psi(\mathbf{x},t))\right) = \mathcal{C}\int \mathcal{D}[\phi]\exp\left[-\int d\mathbf{x}dt\,\frac{Q}{2}\phi(\mathbf{x},t)^2 - i\phi(\mathbf{x},t)\Big(D\psi(\mathbf{x},t) - F\psi(\mathbf{x},t))\Big)\right]. \quad (2.23)$$

This allows to linearize the action integral introducing a fictitious field ϕ, that is defined over the entire time and space axes. The transformation introduces new integrations that can be summarized as $\mathcal{D}[\varphi]$. This symbol means that the integration must be carried out considering all the possible configurations of the field, or better, all the possible paths that the field can follow. The probability density function becomes

$$P[\psi(\mathbf{x},t)] = \mathcal{N}'\int \mathcal{D}[\phi]\exp\left[-\int d\mathbf{x}dt\,\frac{Q}{2}\phi(\mathbf{x},t)^2 - i\phi(\mathbf{x},t)\Big(D\psi(\mathbf{x},t) - F\psi(\mathbf{x},t))\Big)\right]. \quad (2.24)$$

It is useful to consider the F term separately as another forcing term aside from the noise, and separate the action integral in a free part and an interacting part as

$$\begin{aligned} P[\psi] &= \mathcal{N}'\int \mathcal{D}[\phi]\exp\Big(-\mathcal{S}_{free}[\psi,\phi]\Big)\exp\Big(-\mathcal{S}_i[\psi,\phi]\Big) \\ &= \mathcal{N}'\int \mathcal{D}[\phi]\exp\left(-\int d\mathbf{x}dt\,\frac{Q}{2}\phi(\mathbf{x},t)^2 - i\phi(\mathbf{x},t)D\psi\right) \\ &\qquad \exp\left(-\int d\mathbf{x}dt\,i\phi(\mathbf{x},t)F\psi(\mathbf{x},t)\right), \end{aligned} \quad (2.25)$$

with obvious meaning of the quantity $\mathcal{S}_{free}[\psi,\phi]$ and $\mathcal{S}_i[\psi,\phi]$. Once the PDF is known, all the ensemble averages over the noise can be computed. As in statistical mechanics or in QFT, maybe the most important quantity that it is possible to obtain is the generating functional, from which all the statistical quantity, for example variance, correlation function, and in general the n-moment describing the system, can be obtained by derivation of this functional.

The generating functional is nothing more than the expectation value over the noise

of the following functional

$$\exp\left(\mathcal{J}(\mathbf{x},t)\cdot\Phi(\mathbf{x},t)^{\top}\right)=\exp\left(\int J_{\psi}(\mathbf{x},t)\psi(\mathbf{x},t)+J_{\phi}(\mathbf{x},t)\phi(\mathbf{x},t)]\right), \tag{2.26}$$

where $\Phi(\mathbf{x},t)=(\psi(\mathbf{x},t),\phi(\mathbf{x},t))$ and $\mathcal{J}(\mathbf{x},t)=(J_{\psi}(\mathbf{x},t),J(\mathbf{x},t)_{\phi})$ is the so called source vector. The expectation values of this functional is the generating functional

$$\mathcal{Z}[\mathcal{J}]=\mathcal{N}'\int\mathcal{D}[\phi]\mathcal{D}[\psi]\exp\Big(-\mathcal{S}_{free}[\psi,\phi]\Big)\exp\Big(-\mathcal{S}_{i}[\psi,\phi]\Big)\exp\left(\mathcal{J}(\mathbf{x},t)\cdot\Phi(\mathbf{x},t)^{\top}\right) \tag{2.27}$$

and since $\mathcal{Z}[0]=1$, $\mathcal{N}'=\mathcal{Z}^{-1}[0]$. The advantage to have introduced the generating functional consists in transforming the computation of correlation function from complicated integral to functional derivation. For example, to compute the so called two-points function at equal time, from which you can find the variance and correlation at equal time, it is possible using the following equation

$$\langle\psi(\mathbf{x},t)\psi(\mathbf{x}',t)\rangle=\frac{\delta}{\delta J_{\psi}(\mathbf{x},t)}\frac{\delta}{\delta J_{\psi}(\mathbf{x}',t)}\mathcal{Z}[\mathcal{J}]\bigg|_{\mathcal{J}=0}. \tag{2.28}$$

Acting on the generating functional with more functional derivative of the source field, all the other statistical moments can be found.

If $F=0$, $\mathcal{Z}[\mathcal{J}]=\mathcal{Z}_0[\mathcal{J}]$ is Gaussian and it is possible to perform the integration on the fields bringing back the problem to that of finding some Green's functions. Let's consider

$$\mathcal{Z}_0[\mathcal{J}]=\mathcal{M}\int\mathcal{D}[\phi]\mathcal{D}[\psi]\ \exp\Big(-\mathcal{S}_{free}[\psi,\phi]\Big)\exp\left(\mathcal{J}(\mathbf{x},t)\cdot\Phi(\mathbf{x},t)^{\top}\right), \tag{2.29}$$

the generating function of the free part, with $\mathcal{M}$ the normalization constant. If

$$\Delta^{-1}=\begin{pmatrix}0 & (iD)^{\dagger}\\ -iD & Q\end{pmatrix}, \tag{2.30}$$

where the hermitian product is implied,

$$\mathcal{Z}_0[\mathcal{J}] = \mathcal{M}\int \mathcal{D}[\Phi]\exp\left(-\int d\mathbf{x}dt\,\frac{1}{2}\Phi(\mathbf{x},t)\Delta^{-1}\Phi^{\top}(\mathbf{x},t) - \mathcal{J}(\mathbf{x},t)\cdot\Phi(\mathbf{x},t)^{\top}\right), \quad (2.31)$$

where $\mathcal{D}[\Phi] = \mathcal{D}[\psi]\mathcal{D}[\phi]$. The last functional integral is clearly gaussian and it is possible to perform explicitly the computation of the integral, obtaining

$$\mathcal{Z}_0[\mathcal{J}] = \mathcal{M}\sqrt{\det(2\pi\mathcal{G})}\exp\left(\frac{1}{2}\int\int d\mathbf{x}dt\,d\mathbf{x}'dt'\,\mathcal{J}(\mathbf{x},t)\mathcal{G}(\mathbf{x},\mathbf{x}',t,t')\mathcal{J}(\mathbf{x}',t')\right), \quad (2.32)$$

where $\mathcal{G}(\mathbf{x},\mathbf{x}',t,t')$ is the matrix

$$\mathcal{G}(\mathbf{x},\mathbf{x}',t,t') = \begin{pmatrix} \mathcal{G}_{\psi\psi}(\mathbf{x},\mathbf{x}',t,t') & \mathcal{G}_{\psi\phi}(\mathbf{x},\mathbf{x}',t,t') \\ \mathcal{G}_{\phi\psi}(\mathbf{x},\mathbf{x}',t,t') & \mathcal{G}_{\phi\phi}(\mathbf{x},\mathbf{x}',t,t') \end{pmatrix}, \quad (2.33)$$

that satisfies

$$\Delta^{-1}\mathcal{G}(\mathbf{x},\mathbf{x}',t,t') = \delta(t-t')\delta(\mathbf{x}-\mathbf{x}')\mathbf{I}\,, \quad (2.34)$$

and $\mathcal{M} = \left(\sqrt{\det(2\pi\mathcal{G})}\right)^{-1}$ since $\mathcal{Z}_0[0] = 1$. The problem is reduced to the search of Green's functions.

When $F \neq 0$, the computation of the statistical moment is complicated. However, it is possible to prove that

$$\mathcal{Z}[\mathcal{J}] = \mathcal{N}'\exp\left(-\mathcal{S}_i\left[\frac{\delta}{\delta J_\psi(\mathbf{x},t)},\frac{\delta}{\delta J_\phi(\mathbf{x},t)}\right]\right)\mathcal{Z}_0[\mathcal{J}]. \quad (2.35)$$

The computation of this quantity is quite hard and usually is done expanding in power series both the functional operator that represents the interacting action with fields derivatives in place of the fields, and $\mathcal{Z}_0[\mathcal{J}]$. An example of this procedure is shown in the next section.

I have applied this tool to Eq. (2.13) considering three particular situations. At the beginning I have set the mean flow equal to zero and studied the equation in case the damping term is present or not. Then I have added also the mean flow.

2.3 Application

2.3.1 SBPVE with $\mu^{-1} = 0$ and $\bar{\psi} = 0$

The D operator without damping is

$$D = \frac{\partial}{\partial t}\nabla^2 + \frac{\partial}{\partial x}\,. \tag{2.36}$$

The operator, Δ^{-1}, that must be inverted to find the Green' functions in this case, can be read as

$$\Delta^{-1} = \begin{pmatrix} 0 & iD \\ -iD & Q \end{pmatrix}. \tag{2.37}$$

The problem that must be solved is

$$\begin{cases} iD\mathcal{G}_{\phi\psi} = \delta(\mathbf{x}-\mathbf{x}')\delta(t-t') \\ D\mathcal{G}_{\phi\phi} = 0 \\ -iD\mathcal{G}_{\psi\psi} + Q\mathcal{G}_{\phi\psi} = 0 \\ -iD\mathcal{G}_{\psi\phi} + Q\mathcal{G}_{\phi\phi} = \delta(\mathbf{x}-\mathbf{x}')\delta(t-t')\,, \end{cases} \tag{2.38}$$

with $0 < \mathbf{x}, \mathbf{x}' < 1$, $0 < y < 1$ and $0 < t, t'$, where the boundary conditions are

$$\begin{cases} \mathcal{G}(0, y, \mathbf{x}', t, t') = \mathcal{G}(L, y, \mathbf{x}', t, t') \\ \lim_{\substack{y\to 0 \\ y\to 1}} |\mathcal{G}(\mathbf{x}, \mathbf{x}', t, t')| = 0\,, \end{cases} \qquad 0 < t', t \tag{2.39}$$

and the conditions in time are homogeneous

$$\mathcal{G}(\mathbf{x}, \mathbf{x}', 0, t') = 0\,. \tag{2.40}$$

To find the elements of the $\mathcal{G}$ matrix it must be noted that, since the channel structure is considered, all the functions could be expressed by a Sine Fourier series in the meridional component y. Looking at the Δ^{-1} operator in the Fourier space, that means transforming the operator in a common matrix with complex number, it is possible to guess that $\mathcal{G}_{\psi\phi} = -\mathcal{G}_{\phi\psi}$ and $\mathcal{G}_{\phi\phi} = 0$.

A decoupled equation for $\mathcal{G}_{\psi\psi}$ is found applying the operator iD to both sides of

the third equation in the system (2.38) and then using the first equation

$$D^2\mathcal{G}_{\psi\psi} = -Q\delta(\mathbf{x}-\mathbf{x}')\delta(t-t') \tag{2.41}$$

where

$$D^2 = \frac{\partial^2}{\partial t^2}\nabla^4 + \frac{\partial^2}{\partial x^2} + 2\frac{\partial^2}{\partial t \partial x}\nabla^2\,, \tag{2.42}$$

and ∇^4 represents the Laplacian of a Laplacian. To solve this equation, together with Eq. (2.40,2.39), another condition in time is used,

$$\mathcal{G}(\mathbf{x},\mathbf{x}',T,t') = 0\,. \tag{2.43}$$

Once $\mathcal{G}_{\psi\psi}$ is found, $\mathcal{G}_{\phi\psi}$ is determined from the third equation of the system above. Let's start to solve Eq. (2.41). Taking into account the following expansion series for the Dirac delta functions

$$\delta(y-y') = 2\sum_{n=1}^{+\infty}\sin(l_n y)\sin(l_n y')\,, \quad 0<y,y'<1\,, \tag{2.44}$$

$$\delta(x-x') = \sum_{m=-\infty}^{+\infty} e^{ik_m(x-x')}\,, \quad 0<x,x'<1\,, \tag{2.45}$$

with $l_n = n\pi$ and $k_m = 2\pi m$, to ensure the proper boundary condition, it is possible expanding $\mathcal{G}_{\psi\psi}$ in a Sine Fourier series in y and in a Fourier series along the x direction

$$\mathcal{G}_{\psi\psi}(\mathbf{x},\mathbf{x}',t,t') = \sum_{m=-\infty}^{\infty}\sum_{n=1}^{\infty} e^{ik_m x}\sin(l_n y) g_{mn}(\mathbf{x}',t,t') \tag{2.46}$$

with

$$g_{mn}(\mathbf{x}',t,t') = 2\int_0^1\int_0^1 dxdy\,\mathcal{G}_{\psi\psi}(\mathbf{x},\mathbf{x}',t,t')e^{ik_m x}\sin(l_n y)\,. \tag{2.47}$$

Substituting the series above into Eq. (2.41), an ordinary differential equation for the coefficient g_{mn} is found

$$\frac{\partial^2 g_{mn}}{\partial t^2} - 2i\frac{k_m}{k_m^2+l_n^2}\frac{\partial g_{mn}}{\partial t} - \frac{k_m^2}{(k_m^2+l_n^2)^2}g_{mn} = -\frac{2Q\sin(l_n y')e^{-ik_m x'}}{(k_m^2+l_n^2)^2}\delta(t-t') \tag{2.48}$$

The solution, with the proper time condition, Eq. (2.40), is

$$g_{mn}(\mathbf{x}',t,t') = \frac{2Q\sin(l_n y')(T(t'-t)\Theta(t-t')+t(T-t')\Theta(T-t'))e^{-ik_m x'}e^{\frac{ik_m}{k_m^2+l_n^2}(t-t')}}{T\left(k_m^2+l_n^2\right)^2}. \tag{2.49}$$

Here Θ is the Heaviside function. For equal time $t=t'$, this expression is reduced to

$$g_{mn}(\mathbf{x}',t,t) = \frac{2Qte^{-ik_m x'}(T-t)\Theta(T-t)\sin(l_n y')}{T\left(k_m^2+l_n^2\right)^2}\,. \tag{2.50}$$

Considering the evolution for a semi-infinite domain, when T becomes very large, I have obtained

$$g_{mn}(\mathbf{x}',t,t) = \frac{2Qte^{-ik_m x'}\sin(l_n y')}{\left(k_m^2+l_n^2\right)^2}\,. \tag{2.51}$$

Reassuming the Green's function of the problem:

$$\mathcal{G}_{\psi\psi}(\mathbf{x},\mathbf{x}',t,t') = \sum_{m=-\infty}^{\infty}\sum_{n=1}^{\infty}\frac{2Qe^{ik_m(x-x')}\sin(l_n y)\sin(l_n y')e^{\frac{ik_m}{k_m^2+l_n^2}(t-t')}}{T\left(k_m^2+l_n^2\right)^2}$$
$$(T(t'-t)\Theta(t-t')+t(T-t')\Theta(T-t')), \tag{2.52}$$

$$\mathcal{G}_{\phi\psi} = \frac{i}{Q}D\mathcal{G}_{\psi\psi} \tag{2.53}$$

$$\mathcal{G}_{\psi\phi} = -\mathcal{G}_{\phi\psi} \tag{2.54}$$

$$\mathcal{G}_{\phi\phi} = 0\,. \tag{2.55}$$

The two-points correlation function for the stream function ψ is found simply considering

$$\begin{aligned}\langle\psi(\mathbf{x}',t')\psi(\mathbf{x},t)\rangle &= \frac{\delta}{\delta J(\mathbf{x}',t')}\frac{\delta}{\delta J(\mathbf{x},t)}\mathcal{Z}_0[\mathcal{J}]\Big|_{\mathcal{J}=0}\\ &= \frac{1}{2}\frac{\delta}{\delta J(\mathbf{x}',t')}\left(\iint d\mathbf{z}d\tau d\mathbf{z}'d\tau'\delta(\mathbf{x}-\mathbf{z})\delta(t-\tau)\mathcal{G}_{\psi\psi}(\mathbf{z},\mathbf{z}',\tau,\tau')J(\mathbf{z}',\tau')\right.\\ &\left.+\iint d\mathbf{z}d\tau d\mathbf{z}'d\tau' J(\mathbf{z},\tau)\mathcal{G}_{\psi\psi}(\mathbf{z},\mathbf{z}',\tau,\tau')\delta(\mathbf{x}-\mathbf{z}')\delta(t-\tau')\right)\mathcal{Z}_0[\mathcal{J}]\Big|_{\mathcal{J}=0}\\ &= \frac{1}{2}\big(\mathcal{G}_{\psi\psi}(\mathbf{x},\mathbf{x}',t,t')+\mathcal{G}_{\psi\psi}(\mathbf{x}',\mathbf{x},t',t)\big)\,.\end{aligned} \tag{2.56}$$

Then if the variance is searched, $\mathbf{x} = \mathbf{x}'$ and $t = t'$

$$\langle \psi(\mathbf{x},t)\psi(\mathbf{x},t)\rangle = \sum_{m=-\infty}^{\infty}\sum_{n=1}^{\infty}\frac{2Q\sin^2(l_n y)}{T\left(k_m^2+l_n^2\right)^2}t(T-t)\Theta(T-t) \tag{2.57}$$

Considering the evolution for a semi-infinite domain, it is obtained

$$\langle \psi(\mathbf{x},t)\psi(\mathbf{x},t)\rangle = \sum_{m=-\infty}^{\infty}\sum_{n=1}^{\infty}\frac{2Q\sin^2(l_n y)}{\left(k_m^2+l_n^2\right)^2}t\,. \tag{2.58}$$

It would be nice finding a more compact expression for the variance. A simple upper limit can be found with the help of the following inequality

$$\frac{2\sin^2(l_n y)}{\left(k_m^2+l_n^2\right)^2} \leq \frac{2}{\left(k_m^2+l_n^2\right)^2}, \tag{2.59}$$

if

$$\begin{aligned} S_1 &= 2\sum_{m=-\infty}^{\infty}\sum_{n=1}^{\infty}\frac{1}{\left(k_m^2+l_n^2\right)^2} = \frac{2}{\pi^4}\sum_{m=-\infty}^{\infty}\sum_{n=1}^{\infty}\frac{1}{\left(4m^2+n^2\right)^2} \\ &= \frac{2}{\pi^4}\sum_{n=1}^{\infty}\left(\frac{\pi\coth\left(\frac{n\pi}{2}\right)}{4n^3}+\frac{\pi^2\mathrm{csch}^2\left(\frac{n\pi}{2}\right)}{8n^2}\right) \\ &< \frac{2}{\pi^4}\sum_{n=1}^{\infty}\left(\frac{\pi\coth\left(\frac{\pi}{2}\right)}{4n^3}+\frac{\pi^2\mathrm{csch}^2\left(\frac{\pi}{2}\right)}{8n^2}\right) \\ &= \frac{1}{24}\mathrm{csch}^2\left(\frac{\pi}{2}\right)+\frac{\zeta(3)}{2\pi^3}\coth\left(\frac{\pi}{2}\right) = S_1^M, \end{aligned} \tag{2.60}$$

then

$$\langle \psi(\mathbf{x},t)\psi(\mathbf{x},t)\rangle < t\,Q\,S_1^M = t\,Q\left(\frac{1}{24}\mathrm{csch}^2\left(\frac{\pi}{2}\right)+\frac{\zeta(3)}{2\pi^3}\coth\left(\frac{\pi}{2}\right)\right). \tag{2.61}$$

In Fig. (2.1) and in Fig. (2.2) the behavior in time of the variance and its analytical upper limit are found using Eq. (2.61), in the horizontal central line of the channel ($y_c = 0.5$), and out of it ($y = 0.2$). Using a noise fluctuation of order one, in respect to the tendency of the vorticity, after $t \approx 43$, that with our scaling means five days, the standard deviation into the central band of the channel is of the order of the stream function.

Since the upper limit found is not able to take into account the meridional structure of the variance, it is possible to refine a little bit the approximation used.

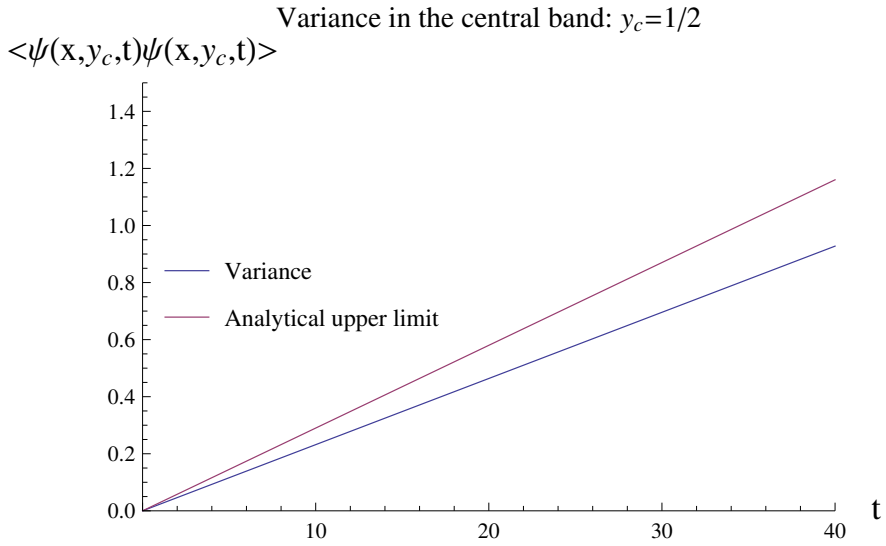

Figure 2.1: Behaviour in time of the variance and its analytical upper limit in the central horizontal line of the channel $y_c = 0.5$. $Q = 1$.

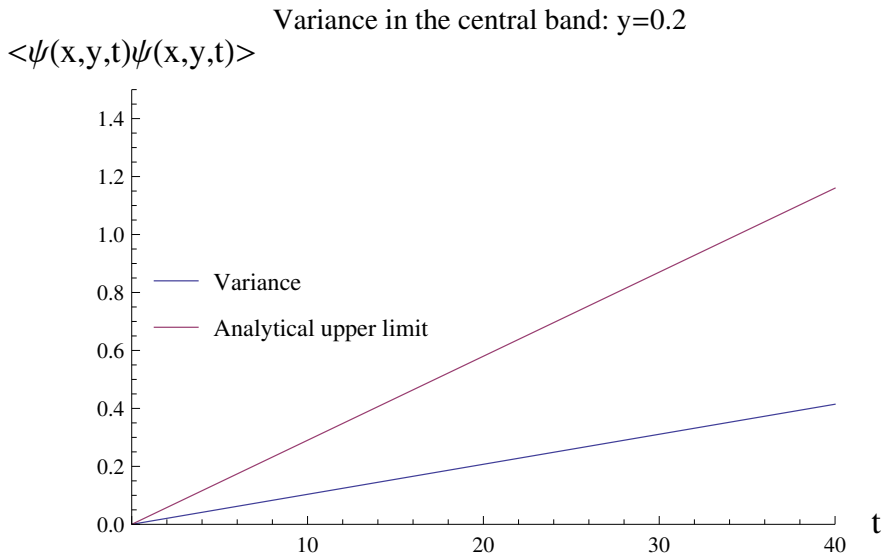

Figure 2.2: Behaviour in time of the variance and its analytical upper limit out of the central horizontal line of the channel $y = 0.2$. $Q = 1$.

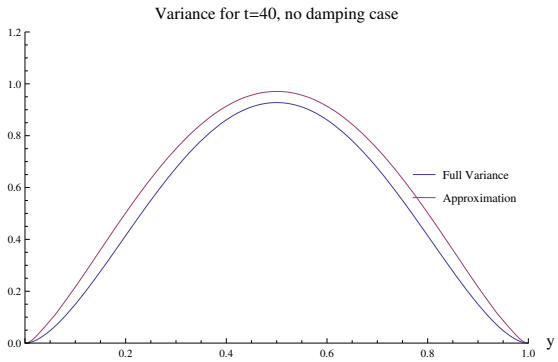

(a) *Variance for the case without damping..*

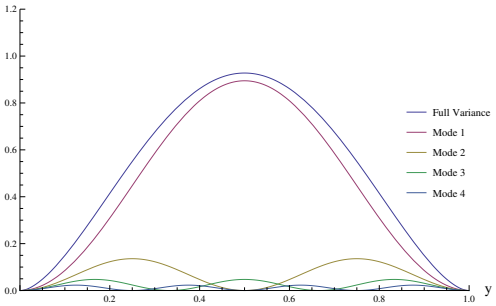

(b) *Modes of the variance.*

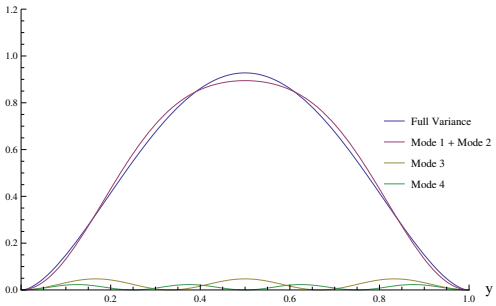

(c) *Using the first two modes the variance is well approximated.*

Figure 2.3: In Fig. 2.3a the full variance up to t=40 compared with Eq. (2.79) is shown, in which the summation on k_m has been carried out and an upper limit is considered for the hyperbolic functions. Fig. 2.3b shows the latitudinal modes of the variance found using Eq. (2.79). Using just the first two leading modes, the full variance is well approximated, Fig. (2.3c).

If

$$\begin{cases} A = \dfrac{\coth(\frac{\pi}{2})}{2\pi^3} \\ B = \dfrac{\operatorname{csch}^2(\frac{\pi}{2})}{4\pi^2}, \end{cases} \tag{2.62}$$

then

$$\langle \psi(\mathbf{x},t)\psi(\mathbf{x},t)\rangle < Q\,t \sum_{n=1}^{+\infty} \left(A\frac{\sin^2(n\pi y)}{n^3} + B\frac{\sin^2(n\pi y)}{n^2} \right). \tag{2.63}$$

Fig. 2.3a shows this upper limit at work. In Fig. 2.3b the first four modes of this upper limit are shown. The first two are clearly the biggest and then it is possible to approximate the whole variance using just $n = 1, 2$:

$$\langle \psi(\mathbf{x},t)\psi(\mathbf{x},t)\rangle \approx Q\,t \left[(A+B)\sin^2\left(\frac{\pi y}{\delta}\right) + \left(\frac{A}{8}+\frac{B}{4}\right)\sin^2\left(\frac{2\pi y}{\delta}\right) \right]. \tag{2.64}$$

In Fig. 2.3c, Eq. (2.64) is shown and compared with the correct variance.

In the free theory, the one that does not consider the interaction with the mean flow, the only interesting quantities are those that involve $\mathcal{G}_{\psi\psi}$. However, how it is showed in the following, when a perturbation expansion is considered, the other Green function are important and must be computed.

2.3.2 SBPVE with $\mu^{-1} \neq 0$ and $\bar{\psi} = 0$

In this case the operator D gets the following form

$$D = \frac{\partial}{\partial t}\nabla^2 + \frac{\partial}{\partial x} + \mu^{-1}\nabla^2 \,. \tag{2.65}$$

Now

$$\Delta^{-1} = \begin{pmatrix} 0 & (iD)^\dagger \\ -iD & Q \end{pmatrix}, \tag{2.66}$$

where

$$(iD)^\dagger = i\left(\frac{\partial}{\partial t}\nabla^2 + \frac{\partial}{\partial x} - \mu^{-1}\nabla^2\right). \tag{2.67}$$

The problem that must be solved to find the Green's functions is

$$\begin{cases} (iD)^\dagger \mathcal{G}_{\phi\psi} = \delta(\mathbf{x}-\mathbf{x}')\delta(t-t') \\ (iD)^\dagger \mathcal{G}_{\phi\phi} = 0 \\ -iD\mathcal{G}_{\psi\psi} + Q\mathcal{G}_{\phi\psi} = 0 \\ -iD\mathcal{G}_{\psi\phi} + Q\mathcal{G}_{\phi\phi} = \delta(\mathbf{x}-\mathbf{x}')\delta(t-t') \,, \end{cases} \tag{2.68}$$

with the boundary condition in space given by Eq. (2.39) and in time by Eq. (2.40). The problem (2.68) is a little bit more complicated.

The third equation can be decoupled multiplying it for the operator $(iD)^\dagger$

$$(iD)^\dagger(-iD)\mathcal{G}_{\psi\psi} = -Q\delta(\mathbf{x}-\mathbf{x}')\delta(t-t') \,, \tag{2.69}$$

that is

$$\left(\frac{\partial^2}{\partial t^2}\nabla^4 + 2\frac{\partial^2}{\partial t \partial x}\nabla^2 + \frac{\partial^2}{\partial x^2} - \mu^{-2}\nabla^4\right)\mathcal{G}_{\psi\psi} = -Q\delta(\mathbf{x}-\mathbf{x}')\delta(t-t') \,, \tag{2.70}$$

if

$$\mathcal{G}_{\psi\psi}(\mathbf{x},\mathbf{x}',t,t') = \sum_{m=-\infty}^{\infty}\sum_{n=1}^{\infty} e^{ik_m x}\sin(l_n y) g_{mn}^{\psi\psi}(\mathbf{x}',t,t')\,, \tag{2.71}$$

the equation for the coefficient $g_{mn}^{\psi\psi}$ is

$$\left(\frac{\partial^2}{\partial t^2} - \frac{2ik_m}{(k_m^2+l_n^2)}\frac{\partial}{\partial t} - \frac{k_m^2}{(k_m^2+l_n^2)^2} - \mu^{-2}\right) g_{mn}^{\psi\psi} = -\frac{2Q\sin(l_n y')e^{-ik_m x'}}{(k_m^2+l_n^2)^2}\delta(t-t')\,, \tag{2.72}$$

which has for solution

$$\begin{aligned} g_{mn}^{\psi\psi}(\mathbf{x}',t,t') = {} & \frac{2Q\sin(l_n y')e^{-ik_m x'}e^{\frac{ik_m(t-t')}{k_m^2+l_n^2}}}{\mu^{-1}\,(k_m^2+l_n^2)^2} \\ & \left(\Theta(T-t')\sinh\left(\mu^{-1}\,t\right)\operatorname{csch}\left(\mu^{-1}\,T\right)\sinh\left(\mu^{-1}\,(T-t')\right)\right. \\ & \left. - \Theta(t-t')\sinh\left(\mu^{-1}\,(t-t')\right)\right). \end{aligned} \tag{2.73}$$

and when the evolution for a semi-infinite domain is considered, when T becomes very large

$$\begin{aligned} g_{mn}^{\psi\psi}(\mathbf{x}',t,t') = {} & \frac{2Q\sin(l_n y')e^{-ik_m x'}e^{\frac{ik_m(t-t')}{k_m^2+l_n^2}}}{\mu^{-1}\,(k_m^2+l_n^2)^2} \\ & \left[e^{-\mu^{-1}\,t'}\sinh\left(\mu^{-1}\,t\right) - \Theta(t-t')\sinh\left(\mu^{-1}\,(t-t')\right)\right]. \end{aligned} \tag{2.74}$$

Note that for equal time, $t = t'$, this expression is reduced to

$$\begin{aligned} g_{mn}^{\psi\psi}(\mathbf{x}',t,t') &= \frac{2Q\sin(l_n y')e^{-ik_m x'}}{\mu^{-1}\,(k_m^2+l_n^2)^2}e^{-\mu^{-1}\,t'}\sinh\left(\mu^{-1}\,t\right) \\ &= \frac{Q\sin(l_n y')e^{-ik_m x'}}{\mu^{-1}\,(k_m^2+l_n^2)^2}\left(1-e^{-2\mu^{-1}\,t}\right). \end{aligned} \tag{2.75}$$

When $\mu^{-1}\to 0$, the damping disappears and Eq. (2.75) must reduce to Eq. (2.51). In fact, in this case the argument of the exponential function is approximately near to zero, and the Taylor expansion can be used

$$e^{-2\mu^{-1}\,t} \approx 1 - 2\mu^{-1}\,t + 2\mu^{-2}\,t^2 - \frac{4\mu^{-3}\,t^3}{3} + \mathcal{O}(\mu^{-4}t^4) \tag{2.76}$$

so that in the limit $\mu^{-1} \to 0$

$$g^{\psi\psi}_{mn}(\mathbf{x}', t, t') \approx \frac{2Q \sin(l_n y') e^{-ik_m x'}}{(k_m^2 + l_n^2)^2} \left(t - \mu^{-1}\, t^2 + \frac{2\mu^{-2}\, t^3}{3} + \mathcal{O}(\mu^{-4} t^2) \right). \tag{2.77}$$

The first term of the expansion gives exactly Eq. (2.51), while the others give the corrections for small value of the damping. However, in this case the whole series can be considered and the variance can be written

$$\langle \psi(\mathbf{x}, t)\psi(\mathbf{x}, t) \rangle = \frac{Q}{\mu^{-1}} \left(1 - e^{-2\mu^{-1}\, t} \right) \sum_{m=-\infty}^{\infty} \sum_{n=1}^{\infty} \frac{\sin^2(l_n y)}{(k_m^2 + l_n^2)^2}. \tag{2.78}$$

As before, you can try to sum or at least to eliminate one of the two summations

$$\langle \psi(\mathbf{x}, t)\psi(\mathbf{x}, t) \rangle \approx \frac{Q}{2\mu^{-1}} \left(1 - e^{-2\mu^{-1}\, t} \right) \left[(A + B) \sin^2 \left(\frac{\pi y}{\delta} \right) + \left(\frac{A}{8} + \frac{B}{4} \right) \sin^2 \left(\frac{2\pi y}{\delta} \right) \right], \tag{2.79}$$

where the coefficient A and B correspond to Eq. (2.62).

Another interesting quantity, is the two-points correlation function, when the evolution for a semi-infinite domain is considered

$$\begin{aligned} \langle \psi(\mathbf{x}, t)\psi(\mathbf{x}', t') \rangle = \frac{Q}{\mu^{-1}} \sum_{m=-\infty}^{\infty} \sum_{n=1}^{\infty} \frac{\sin(l_n y) \sin(l_n y')}{(k_m^2 + l_n^2)^2} \Bigg\{ \\ e^{ik_m(x - x')} e^{\frac{ik_m(t - t')}{k_m^2 + l_n^2}} \left[e^{-t'\mu^{-1}} \sinh\left(t\mu^{-1} \right) - \Theta(t - t') \sinh\left((t - t')\mu^{-1} \right) \right] \\ + e^{ik_m(x' - x)} e^{\frac{ik_m(t' - t)}{k_m^2 + l_n^2}} \left[e^{-t\mu^{-1}} \sinh\left(t\mu^{-1} \right) - \Theta(t' - t) \sinh\left((t' - t)\mu^{-1} \right) \right] \Bigg\} \end{aligned} \tag{2.80}$$

In Fig. (2.4), it is shown how the variance, computed from Eq. (2.80), changes with time and with different truncation of the series. Due to the damping term, there is not an infinite growth for the variance, which now settles at a plateau after $t \approx 200$, that are approximately twenty days with our scaling. In Fig. (2.5), it is possible to observe the periodic behaviour of the horizontal correlation for different truncations of the series. This correlation is obtained normalizing the two-points function with the variance. In Fig. (2.6), the space correlation at fixed $\mathbf{x}'$ and t is shown. In Fig. 2.7, it is shown a comparison of variances in the central band of the channel between the two cases studied, the BPVE with and without the damping term. When $\mu^{-1} t \ll 1$, the two

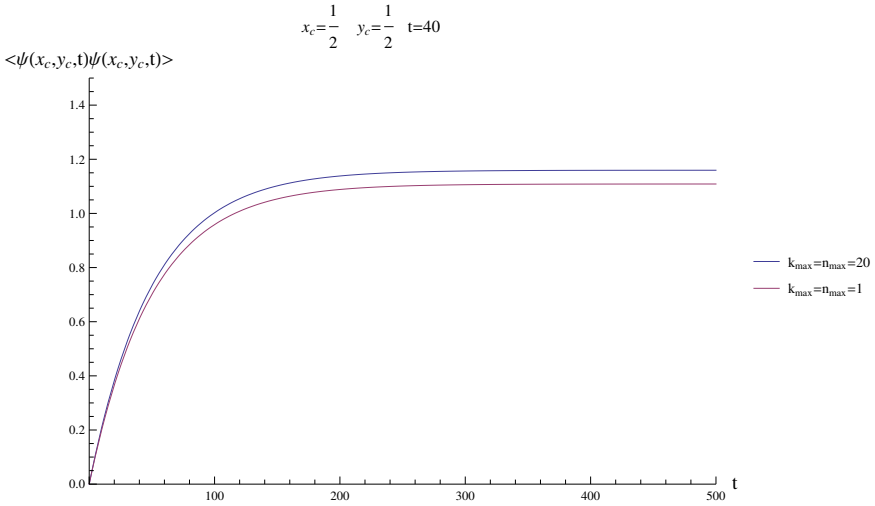

Figure 2.4: Variance for the damped case computed from Eq. (2.80). In this example it is used $y = y' = y_c = \frac{1}{2}$, $x = x' = x_c = \frac{1}{2}$, $Q = 1$ and $\mu^{-1} = 0.01$, and $t = t' = 40$.

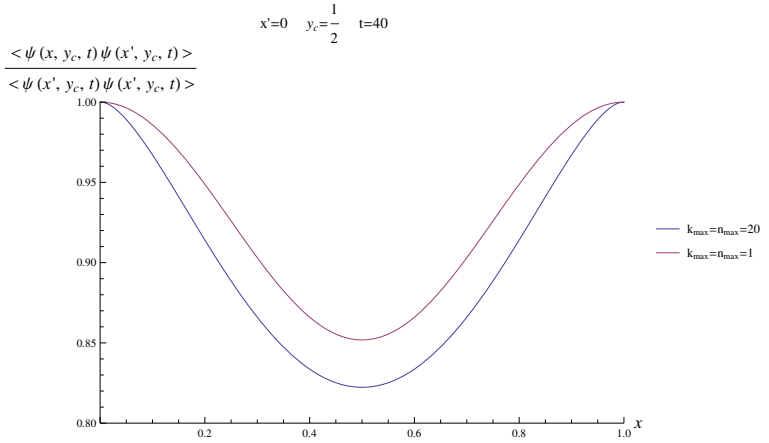

Figure 2.5: Horizontal correlation computed from Eq. (2.80). In this example it is used $y = y' = y_c = \frac{1}{2}$, $x' = 0$, $t = 40$, $Q = 1$ and $\mu^{-1} = 0.01$.

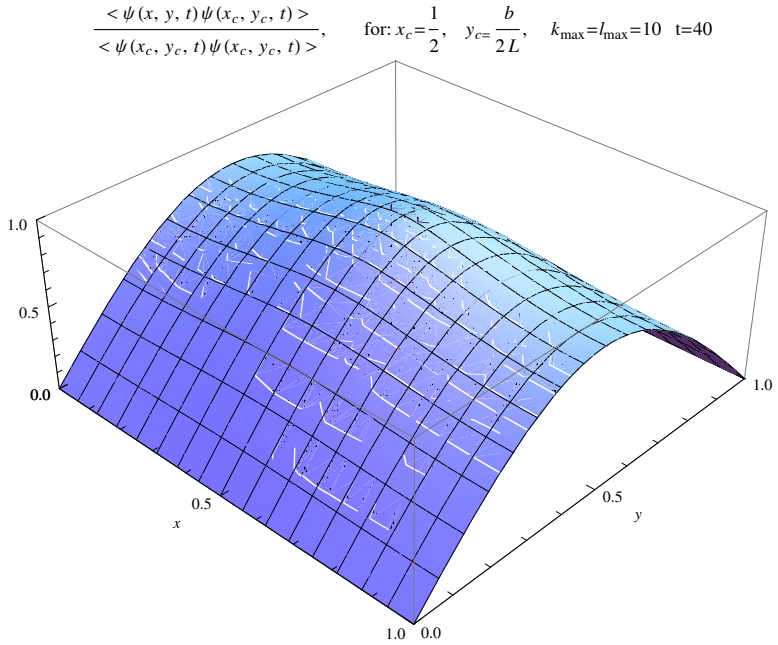

Figure 2.6: Space correlation for $x' = x_c = 0.5$, $y' = y_c \frac{1}{2}$, $t = 40$, $Q = 1$ and $\mu^{-1} = 0.01$.

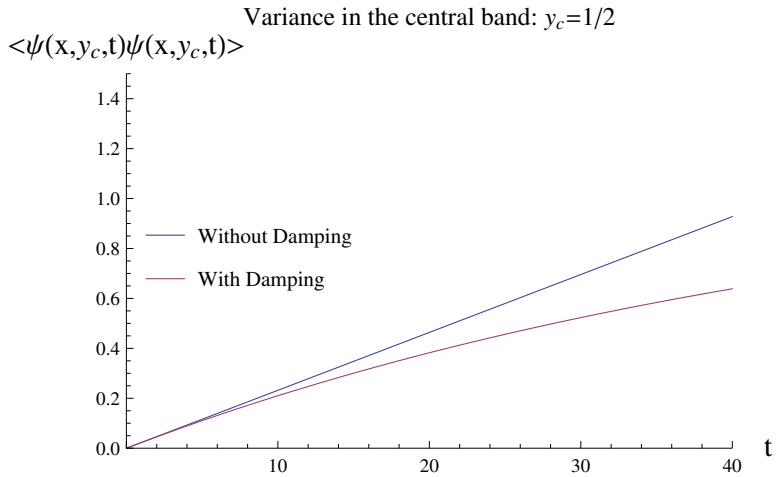

Figure 2.7: Comparison of the variance for the cases with and without damping. When $\mu^{-1}t \ll 1$, the two variances have the same linear behavior.

variances have the same linear behavior.

From the third equation of the system (2.68) it is possible to relate $\mathcal{G}_{\phi\psi}$ with $\mathcal{G}_{\psi\psi}$

$$\mathcal{G}_{\phi\psi} = \frac{i}{Q} D\mathcal{G}_{\psi\psi} \,. \tag{2.81}$$

A similar relation can be found for $\mathcal{G}_{\psi\phi}$. Subtracting the fourth equation of the system

(2.68) to the first

$$(iD)^\dagger \mathcal{G}_{\phi\psi} + iD\mathcal{G}_{\psi\phi} = 0\,, \tag{2.82}$$

and using Eq. (2.81)

$$(iD)^\dagger \frac{i}{Q} D\mathcal{G}_{\psi\psi} + iD\mathcal{G}_{\psi\phi} = 0\,, \tag{2.83}$$

multiplying from right for $-iD^{-1}$

$$\mathcal{G}_{\psi\phi} = -\frac{1}{Q}(iD)^\dagger \mathcal{G}_{\psi\psi}\,. \tag{2.84}$$

Note that when $\mu \to \infty$, $(iD)^\dagger = iD$ and then, thanks to the minus in the relation above, the asymmetry is restored $\mathcal{G}_{\psi\phi} = -\mathcal{G}_{\phi\psi}$. For a similar motivation done in the previous section $\mathcal{G}_{\phi\phi} = 0$.

Reassuming

$$\begin{aligned}\mathcal{G}_{\psi\psi}(\mathbf{x},\mathbf{x}',t,t) = \sum_{m=-\infty}^{\infty}\sum_{n=1}^{\infty} \frac{\mu 2Q e^{ik_m(x-x')}\sin(l_n y)\sin(l_n y') e^{\frac{ik_m(t-t')}{k_m^2+l_n^2}}}{(k_m^2+l_n^2)} \\ \left(\Theta(T-t')\sinh\left(\mu^{-1}t\right)\operatorname{csch}\left(\mu^{-1}T\right)\sinh\left(\mu^{-1}(T-t')\right)\right. \\ \left. -\,\Theta(t-t')\sinh\left(\mu^{-1}(t-t')\right)\right)\end{aligned} \tag{2.85}$$

$$\mathcal{G}_{\phi\phi}(\mathbf{x},\mathbf{x}',t,t) = 0 \tag{2.86}$$

$$\mathcal{G}_{\phi\psi}(\mathbf{x},\mathbf{x}',t,t) = \frac{i}{Q} D\mathcal{G}_{\psi\psi}(\mathbf{x},\mathbf{x}',t,t) \tag{2.87}$$

$$\mathcal{G}_{\psi\phi}(\mathbf{x},\mathbf{x}',t,t) = -\frac{1}{Q}(iD)^\dagger \mathcal{G}_{\psi\psi}(\mathbf{x},\mathbf{x}',t,t). \tag{2.88}$$

2.3.3 SBPVE with $\mu^{-1} \neq 0$ and $\bar{\psi} \neq 0$

Consider the full linear operator

$$D = \frac{\partial}{\partial t}\nabla^2 + \frac{\partial}{\partial x} - \epsilon\left(\frac{\partial^2 \bar{U}}{\partial y^2}\frac{\partial}{\partial x} - \bar{U}\frac{\partial}{\partial x}\nabla^2\right) + \mu^{-1}\,, \tag{2.89}$$

in which all terms are maintained. As for the damped example

$$\Delta^{-1} = \begin{pmatrix} 0 & (iD)^\dagger \\ -iD & Q \end{pmatrix}, \tag{2.90}$$

where

$$(iD)^\dagger = i\left(\frac{\partial}{\partial t}\nabla^2 + \frac{\partial}{\partial x} - \epsilon\left(\frac{\partial^2 \bar{U}}{\partial y^2}\frac{\partial}{\partial x} - \bar{U}\frac{\partial}{\partial x}\nabla^2\right) - \mu^{-1}\right). \tag{2.91}$$

The only interesting mathematical entity, if all the terms of the equation in the D operator are considered, is $\mathcal{G}_{\psi\psi}$, from which it is possible to find variance and correlations of the stream function. However, the decoupled equation that must be considered to find $\mathcal{G}_{\psi\psi}$, similarly to the Eq. (2.69) involves the operator $(iD)^\dagger(-iD)$. This kind of equation can be solved easily just for a constant mean flow; otherwise it is impossible to solve it analytically.

If the mean flow profile is not constant, it is better to take a step back and rewrite the initial equation as

$$\frac{\partial}{\partial t}\nabla^2\psi' + \frac{\partial \psi'}{\partial x} + \mu^{-1}\psi' = \epsilon\Big(\frac{\partial^2 \bar{U}}{\partial y^2}\frac{\partial \psi'}{\partial x} - \bar{U}\frac{\partial \nabla^2 \psi'}{\partial x}\Big) + \eta\,. \tag{2.92}$$

If the Rayleight condition for the stability is hold, that is

$$1 - \frac{\partial^2 \bar{U}}{\partial y^2}\frac{U}{L^2\beta} \tag{2.93}$$

doesn't change sign in the channel, no exponential growth from the Jacobian part of the equation will rise and then a perturbation expansion to find the generating functional, and the correlation functions, is possible. It is possible to define

$$D = \frac{\partial \nabla^2}{\partial t} + \frac{\partial}{\partial x} + \mu^{-1} \tag{2.94a}$$

$$F[\psi] = \epsilon\left(\frac{\partial^2 \bar{U}}{\partial y^2}\frac{\partial \psi'}{\partial x} - \bar{U}\frac{\partial \nabla^2 \psi'}{\partial x}\right) \tag{2.94b}$$

Considering these definition, I have been able to use the results already obtained for the free Green's functions. In fact, remembering Eq. (2.35), the whole generating func-

tional can be written as

$$\mathcal{Z}[\mathcal{J}] = \mathcal{N}' e^{-\epsilon i \int \frac{\delta}{\delta J_\phi(\mathbf{x},t)}\left(\frac{\partial^2 \bar{U}}{\partial y^2}\frac{\partial}{\partial x} - \bar{U}\frac{\partial \nabla^2}{\partial x}\right)\frac{\delta}{\delta J_\psi(\mathbf{x},t)}\mathbf{dx}dt} e^{\frac{1}{2}\iint \mathcal{J}^\top(\mathbf{x},t)\mathcal{G}(\mathbf{x},t,\mathbf{x}',t')\mathcal{J}(\mathbf{x}',t')\,\mathbf{dx}dt\mathbf{dx}'dt'}, \tag{2.95}$$

where $\mathcal{N}' = \mathcal{Z}[0]$. Eq. (2.95) is only a formal expression whose validity must be verified case by case. From a practical point of view, its series expansion, that can be eventually represented graphically using Feynman diagram is defined by means. Only connected graphs, that are not separated in different parts (basically the Green's functions involved must be linked together by means some common points of the space time), are interesting. All the others are simplified by the normalization. Since

$$\langle \psi(\mathbf{x},t)\psi(\mathbf{x}',t')\rangle = \frac{\delta}{\delta J_\psi(\mathbf{x},t)}\frac{\delta}{\delta J_\psi(\mathbf{x}',t')}\mathcal{Z}[\mathcal{J}]\bigg|_{\mathcal{J}=0}, \tag{2.96}$$

the first correction to the correlation function is of order ϵ, more precisely, it is obtained by the order ϵ of the interaction operator expanded perturbatively and the second order of the expansion in $\mathcal{J}$ of the free part. This is because the second order expansion of the free part gives terms containing exactly three sources J_ψ and one J_ϕ that will be hit by the correspondent functional derivatives coming from the expansion of the interaction part and from Eq.(2.96) . Then, when the source is put to zero, those terms will survive. To save writing, are introduced the abbreviations J^x_ψ for $J_\psi(\mathbf{x},t)$, $\int_x$ for $\int \mathbf{dx}dt$, $\mathcal{G}^{ab}_{\psi\psi}$ for $\mathcal{G}_{\psi\psi}(\mathbf{x},t,\mathbf{x}',t')$ and similarly for the other Green's functions. Since the interaction involves also derivatives, it will be useful to use $x = (x_0, x_1, x_2) = (t, x, y)$. With this in mind, it is possible to write down the correlation between two fields as follow:

$$\langle \psi^a \psi^b\rangle = \frac{1}{2}(G^{ab}_{\psi\psi} + G^{ba}_{\psi\psi}) - \frac{\epsilon i}{8}\frac{\delta}{\delta J^a_\psi}\frac{\delta}{\delta J^b_\psi}\int_c \frac{\delta}{\delta J^c_\phi}\left(\frac{\partial^2 \bar{U}_c}{\partial y^2}\frac{\partial}{\partial c_1} - \bar{U}_c\frac{\partial \nabla^2_c}{\partial c_1}\right)\frac{\delta}{\delta J^c_\psi}$$
$$\int_d\int_e\int_f\int_g 2J^d_\psi \mathcal{G}^{de}_{\psi\psi}J^e_\psi(J^f_\psi \mathcal{G}^{fg}_{\psi\phi}J^g_\phi + J^f_\phi \mathcal{G}^{fg}_{\phi\psi}J^g_\psi) + \mathcal{O}(\epsilon^2)\,. \tag{2.97}$$

If you call

$$O_c = \frac{\partial^2 \bar{U}_c}{\partial c_2^2}\frac{\partial}{\partial c_1} - \bar{U}_c\frac{\partial \nabla^2_c}{\partial c_1}, \tag{2.98}$$

and considering only connected graphs, you have

$$\langle \psi^a \psi^b \rangle = \frac{1}{2}(G^{ab}_{\psi\psi} + G^{ba}_{\psi\psi}) - \left(\frac{\epsilon i}{4} \int_c (\mathcal{G}^{bc}_{\psi\phi} + \mathcal{G}^{cb}_{\phi\psi}) O_c (\mathcal{G}^{ac}_{\psi\psi} + \mathcal{G}^{ca}_{\psi\psi}) + a \leftrightarrow b \right) + \mathcal{O}(\epsilon^2)\,, \quad (2.99)$$

The first term of the two-points function is independent by the mean flow that act only at ϵ.

A quick estimate of the behavior of the correction into Eq. (2.99) can be done making some simplifications. In particular, it is interesting to see how the variance changes with different mean flow, then $b = a$. I have considered just the leading harmonic, $n = 1$ and $m = -1, 0, 1$ for this estimate. It is easy to check that the quantity above is real. The complex exponentials into the Green's functions represent bounded oscillations, and to simplify further the computation, the time oscillations are substituted with the constant 1.

The basic Green's function used in the computation is

$$\mathcal{G}^{ac}_{\psi\psi} = \frac{2\mu Q}{\pi^4 25} \sin(\pi a_2) \sin(\pi c_2)\, f(a_0, c_0)\, (2\cos(2\pi(a_1 - c_1)) + 25)\,, \quad (2.100)$$

where

$$f(a_0, c_0) = e^{-c_0 \mu^{-1}} \sinh\left(a_0 \mu^{-1}\right) - \Theta(a_0 - c_0) \sinh\left((a_0 - c_0)\mu^{-1}\right). \quad (2.101)$$

The other functions appearing in Eq. (2.99) are computed starting from the equation above using the relations in Eq. (2.87) and in Eq. (2.88).

After the integration of c_1 between 0 and 1, also the first order correction appears to be independent by the longitudinal variable a_1 (at least considering just the leading modes), and remain

$$\mathcal{O}(\epsilon) = \frac{16\epsilon\mu^2 Q}{625\pi^6} \int_0^{+\infty} (f(a_0, c_0) + f(c_0, a_0))^2\, dc_0 \int_0^{\delta} \sin^2(\pi a_2) \sin^2(\pi c_2) \left(\frac{\partial U(c_2)}{\partial c_2^2} + 5\pi^2 U(c_2) \right) dc_2. \quad (2.102)$$

The temporal integration can be carried out easily dividing the integration interval in two parts and simplifying the integrand which contains the Heaviside functions

$\Theta(a_0 - c_0)$ and $\Theta(c_0 - a_0)$

$$\int_0^{+\infty} (f(a_0, c_0) + f(c_0, a_0))^2 \, dc_0 = \mu - e^{-2a_0\mu^{-1}}(2a_0 + \mu). \tag{2.103}$$

The integrations along c_1 and c_0 are equal for every kind of mean flow, if a mean flow that depends just on the meridional component and it is constant in time and longitude is considered. If you want to compute the correction for a generic stable mean flow, now, you just need to carry out the integration on the meridional variable:

$$\mathcal{O}(\epsilon) = \epsilon Q \frac{16\mu^2}{625\pi^6}(\mu - e^{-2a_0\mu^{-1}}(2a_0 + \mu)) \sin^2(\pi a_2) \int_0^1 \sin^2(\pi c_2) \left(\frac{\partial U(c_2)}{\partial c_2^2} + 5\pi^2 U(c_2) \right) dc_2. \tag{2.104}$$

In order to show a simple application of Eq. (2.104), a mean stream function with parabolic profile is used, Fig. 2.8, described by the following function:

$$\bar{\psi}(c_2) = -4(c_2 - 1)c_2. \tag{2.105}$$

From Eq. (2.105) you can read the zonal mean flow profile, which is a simple linear shear,

$$U(c_2) = -\frac{\partial \bar{\psi}(c_2)}{\partial c_2} = -4 + 8c_2, \tag{2.106}$$

and the second derivatives of the mean flow, which is a constant equal to zero meaning that the mean flow is stable. In this particular case, the integrand appearing in Eq. (2.104) depends just on the zonal mean flow, that is asymmetric along the meridional direction of the channel, and by the the square of the $\sin$ function, that is symmetric along the meridional direction. In this case the integral is null, and no corrections appear to the leading modes at $\mathcal{O}(\epsilon)$. For corrections different from zero, it is necessary to consider the interaction between different harmonic at higher order.

2.4 Summary

In this chapter I have shown how it is possible to associate a generating functional to SPDE in atmospheric field. The utility of this mathematical entity resides in the fact

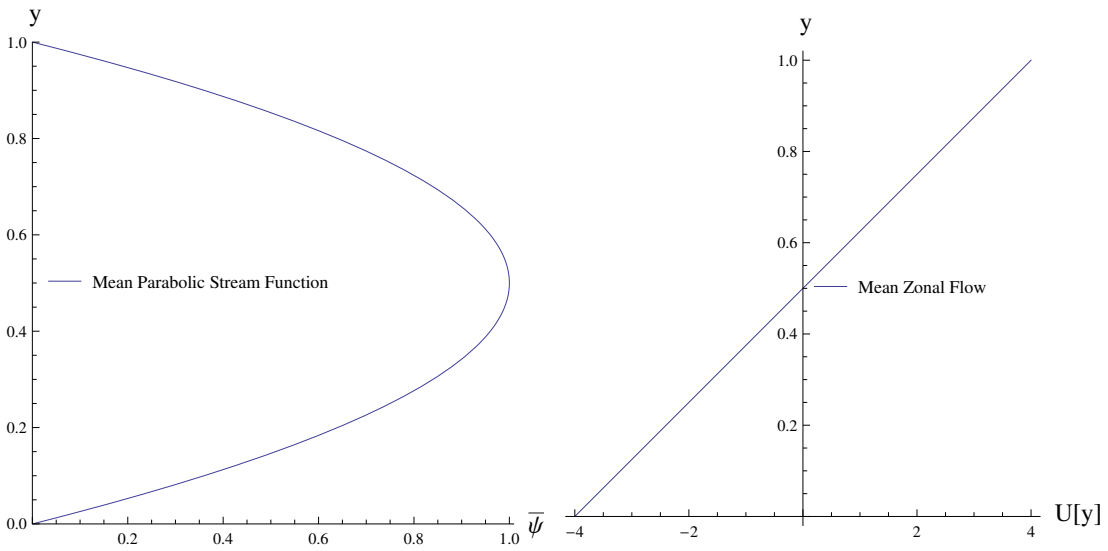

Figure 2.8: Parabolic meridional profile of the mean stream function used in the example on the left panel, the correspondent mean flow zonal velocity in the center panel, and the second meridional derivative of the mean flow profile on the right.

images/Path/

that, using simple functional differentiation, all the statistical quantities describing the stochastic field can be found.

This method has been used in (Navarra et al., 2013b) to find correlation and variance of a (0d+1) linear and non-linear simple model of ENSO with stochastic forcing. In this work, I have applied this method to a more complicated system, (2d+1), described by the Stochastic Barotropic Vorticity Equation (SBPVE) into a channel. Periodic boundaries in the longitudinal direction and rigid walls bounding the channel to the north and south are used. I have solved the problem of finding the generating functional and I have used it to get analytical expressions for variance and correlation functions. In general with this method I have been able to find all the n-points functions of the problem. I present here the study for three configurations of the SBPVE, obtained adding or neglecting damping and mean flow:

1. $\bar{\psi} = 0 \quad \mu^{-1} = 0$,
2. $\bar{\psi} = 0 \quad \mu^{-1} \neq 0$,
3. $\bar{\psi} \neq 0 \quad \mu^{-1} \neq 0$.

I have shown that this method is applicable to the SBPVE but with many technical difficulties.

The problem is reduced to find the Green's functions which reverse a particular operator. For each of these configurations the analytic form that describes the variance and correlation of the stochastic field is found. The first configuration, the simplest, shows a variance which grows linearly in time, the typical behavior of systems subject to white noise where there is not a term of damping. The meridional structure is expanded in series of sin, since the field must go to zero to the to meridionals boundaries. The solution is written using two summations, but fortunately, also using only the leading harmonics, you can well describe the variance and then find a more compact analytical form that describes it. If the term of damping is different from zero, variance and correlation are stable over time and do not grow indefinitely. When $\mu^{-1}t \ll 1$, i.e damping for the time is small, the expression for the variance is reduced to the one found for the first configuration. So initially there is a linear increase of the variance before changing behavior when time increases. As regards the third configuration, it is possible to write an approximate form of variance and correlation using a perturbation expansion of the generating functional. This functional can be written as an operator, which depends on the part considered to be interacting (in this case the part of the equation containing the mean flow), which acts on the free part of the generating functional (already studied in the previous configurations). By expanding the operator and the free functional, using a parameter ϵ which naturally arises from the scaling used, it is possible to find the searched expressions. For this third configuration I have used an average flow of example with a parabolic profile. The correction is reduced to the calculation of an integral in y, that, in this simple case, it is null if you use only the first harmonic of the Green's functions associated with the problem.

The interacting part considered here, is the Jacobian, that appears in the SBPVE linearized around the mean flow. I have had to assume that the fluid is stable, but also in case of instability, if you know the typical time scale associated with it, τ_i, you could apply this method considering $t < \tau_i$ for an initial investigation.

CHAPTER 3

ATMOSPHERE-OCEAN INTERACTIONS AT STRONG COUPLINGS IN A SIMPLE MODEL OF ENSO

The contents of this chapter have been published in Journal of Climate, (Navarra et al., 2013a).

3.1 Introduction

Simple models of ENSO (El Niño / Southern Oscillation) were able to reproduce the basic characteristic behavior and scale of ENSO (Cane and Zebiak, 1985; Cane et al., 1986; Zebiak and Cane, 1987) and a dynamical framework was developed to explain the underlying dynamics in terms of delayed oscillators (Schopf and Suarez, 1988; Suarez and Schopf, 1988; Battisti and Hirst, 1989; Philander, 1990; Jin and Neelin, 1993; Neelin et al., 1994, 1998) or in terms of the recharge mechanism (Jin, 1996, 1997a). Other conceptual models have also been proposed, like for instance the advective-reflective oscillator (Picaut et al., 1997), but they have been shown to be equivalent representation of a more general oscillatory dynamics (Wang, 2001).

However, the observations show that the time series of the ENSO indices is strongly irregular and the differentiation from one event to the next is strong, with significant

differences in the termination and start up of the different phases. These observations prompted the hypothesis that ENSO could instead be described as a stochastically forced linear system (Penland and Sardeshmukh, 1995; Moore and Kleeman, 1999b,a; Thompson and Battisti, 2000, 2001; Penland, 1996). It is still unclear if the nature of ENSO is therefore a deterministic system with strong nonlinearities or a linear systems stochastically forced (Chang et al., 1996; Philander and Fedorov, 2003).

The issue of the statistical distribution of the ENSO phenomenon has been considered several times. Early works (Burgers and Stephenson, 1999) showed there is considerable deviation from normality in the west and east Pacific, but some noticeable deviations exist also in the central Pacific region where widely used indexes like ENSO3 and ENSO3.4 are computed. They also showed that histograms are suitable to identify deviations from normality and to estimate the probability distribution of the SST in each point or region. Monahan and Dai (2004) investigated the nongaussian character of ENSO using principal component analysis. The skewness has been attributed to nonlinear interactions by An et al. (2005), showing that probably a clear distinction between the previous choices may not be necessary and the final conclusion is still unclear (Kapur et al., 2012).

A simple linear model proposed by Jin (1997a) can sustain oscillations as a function of the interaction parameter between the wind stress and the SST. A single oscillatory mode exists for most of the range of the parameter except for regions of large values, corresponding to a very tight coupling between SST and wind stress, and also for very small values, corresponding to relative independence. The model shows oscillations also when a cubic nonlinear terms is introduced following Suarez and Schopf (1988). Jin concentrated on the oscillatory range to develop further his theory deeming unphysical both weak and strong coupling since they could not sustain oscillations. Available evidence indicates that ENSO is indeed coupled, so it is reasonable to ignore the weak coupling limit, but the high end of the parameter range (strong coupling) is more puzzling. Strong dynamical constraints are required to prevent the system to exit the range of values for which oscillations exist, but no explanation has been put forward. On the other hand, the estimation of the interaction coefficient has proven elusive. It is difficult to reduce the complex relation between wind and SST to a single simple parameter that could be diagnosed from observation and models. It is possi-

ble that energy based approaches (Fedorov et al., 2003; Brown and Fedorov, 2010) can shed some light on the issue, but they have still to deliver a definitive answer that would allow to assess the interaction regime for observations or the models.

There is however a third possibility. It is possible that the coupled system is not so finely tuned, but it goes through different stages as the evolution of the basic state on longer time scales, like interdecadal variation and their interaction with anthropogenic climate change, progresses. It would be then conceivable that that there will be phases of strong interactions and phases of moderate interaction and so it is worthwhile to investigate more the strong interaction phase. In this phase the system does not have oscillations, but can have a number of stable or unstable critical points and in the case of Jin model it will have two stable points. Transitions from one point to the other are impossible in the deterministic dynamical system, but however becomes possible if we introduce a stochastic forcing that allows fluctuations between two different states. In this theory what we call ENSO events are the transitions between two different states driven by noise. We will develop in this paper a theory of a stochastic ENSO showing that we can get realistic probability distributions and that we can identify different ENSO states in the observations. A suitable equation for the evolution of the probability distribution will be developed. In this sense we are proposing that ENSO is stochastically driven system with strong nonlinearities.

Though we are using additive noise as the stochastic component, we do not advocate it as the only forcing mechanism for ENSO. Most probably multiplicative noise will need to be considered (Penland and Sardeshmukh, 1995; Penland, 2003; Sura et al., 2005; Berner, 2005), but the framework that we introduce here is not limited to additive noise and it can be extended to consider other kind of noises. It is a framework that allows a theoretical investigation of various kind of noise, additive, multiplicative or colored that can be involved in developing a full theory of ENSO. We show that even a drastically simplified model has some of the features found in the behaviour of a NINO index.

The asymmetry of the positive and negative ENSO events has also been discussed by several studies, though the issue has often been discussed together with the irregularity of the oscillations. Jin et al. (1994b, 1996) and Tziperman et al. (1994b) proposed that the interactions of the seasonal cycle with the chaotic dynamics of the system

caused the irregularity, whereas Penland and Sardeshmukh (1995), Moore and Kleeman (1999b,a), Kleeman (2010) and Thompson and Battisti (2000) discussed the effect of stochastic forcing onto the non normal modes of the linear system. The role played by the nonlinear component of the thermal advection has been investigated by Jin et al. (2003) and An and Jin (2004). Timmermann et al. (2003) proposed an intermittent nonlinear theory and Majda et al. (2006) investigated stochastic effects in deterministic systems. Other nonlinear mechanisms that generate an asymmetry between El Niño e La Niña cases have been proposed, such as vertical mixing processes (Wang and McPhaden, 2000) and asymmetric atmospheric responses (Kang and Kug, 2002).

Recently, some interest has arisen on the interaction of the Madden-Julian oscillation (Madden and Julian, 1971a)with ENSO (Kapur et al., 2012). The MJO can contribute to the generation of positive anomalies in the east and central Pacific (Zhang and Gottschalck, 2002; Zhang, 2001) and models tend to have a better representation of ENSO events if MJO variability is enhanced or better represented (Zavala-Garay et al., 2008; Lengaigne et al., 2004). Correlations between ENSO and MJO activity has been detected in the observations(Zhang and Gottschalck, 2002; Hendon et al., 2007), whereas models have advanced significantly the capability to describe MJO (Subramanian et al., 2011; Sperber et al., 2005; Gualdi et al., 1997) and recently models have shown a capacity to improve both MJO and ENSO (Neale et al., 2008). This correlation has led to the consideration of multiplicative stochastic noise as a generalization of the additive noise more generally used. However, many of the techniques that we are going to describe are not dependent on additive or multiplicative nature of the noise.

In this paper we are proposing a new approach to the ENSO variability that centers on the hypothesis that ENSO can be described as a non-linear system that can sustain oscillations as a function of the coupling strength, but that can also generate fluctuations when oscillations cannot be sustained between different states via stochastic fluctuations. The probability distribution of the ENSO will be obtained directly via solving the Fokker-Planck equation of a simplified model and it will be shown that the asymmetry can be explained in terms of a simple parameter that can be interpreted as related to the average seasonal MJO activity. The general picture that emerges is that ENSO is acted on by different mechanisms as coupling strength and intensity of the stochastic forcing varies, providing possible explanations for the variety of behaviour

that we experience in models and in the observations.

Though strict realism is not the purpose of this paper, we will be able to offer a new framework for investigating ENSO from a different angle and the model shows some interesting properties.

3.2 The probability distribution of ENSO

Considering the non normalized 1871-2011 NINO3.4 index[1] computed from the HadISST1 data set (Rayner et al., 2003) as the area averaged from 5S-5N and 170-120W, we can estimate the stationary component of the empirical probability distribution by computing the histogram of the NINO3.4 anomalies. A 5-month running mean to remove the high frequency components has been applied. The estimated probability distribution is an asymmetric shape with a marked shift toward negative anomalies that generates a peak around -0.2. A good fit can be obtained with a superposition of two normal distributions, suitably weighted,

$$P(x) = p\exp(-\frac{(x-x_1)^2}{s_1^2}) + (1-p)\exp(-\frac{(x-x_2)^2}{s_2^2}) \tag{3.1}$$

with the mixing parameter p constrained as $0 < p < 1$, resulting in the superposed line visible in Fig.3.1. The bottom panel shows also the same fit applied to the residual obtained subtracting the filtered components from the total anomalies. In this case there is no sign of a double gaussian nature and a single gaussian has a good fit. This result suggests that variability faster than 5-months may be described by gaussian stochastic fluctuations, whereas the slower variability is well captured by two states represented by the gaussians.

However, the models tell a different story. Just to give an appreciation of the variability that different models can exhibit we show in the the following figures the estimated probability distribution obtained from long simulations of the CMCC-SINTEX model (Navarra et al., 2008; Gualdi et al., 2003). In these experiments a different resolution atmospheric model was coupled to the same ocean model. It is a T106 spectral resolution for Fig.(3.2) and spectral T30 for Fig.3.3. It is possible to note that the T106

[1] Available from www.esrl.noaa.gov/psd/gcos_wgsp/Timeseries/Nino34

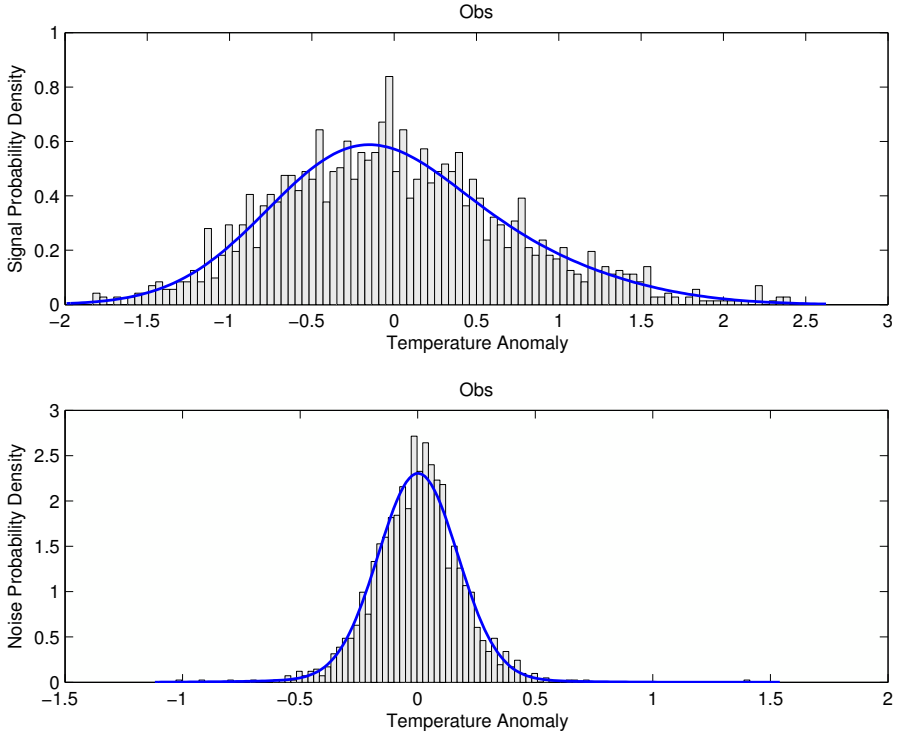

Figure 3.1: The estimated probability distribution of the NINO3.4 index for observations. The monthly mean NINO3.4 data have been obtained from Climate Predictions Center (NOAA) for the period 1871-2012, the seasonal cycle has been removed and a 5-months running mean has been applied. The top panel shows the PDF of the filtered data estimated as a normalised histogram. The bottom panel is the same estimate applied to the residual signal after the running mean has been subtracted. In both panels, the line represents the best fit of a mixture of two normal distributions. The deviations from the running mean appears to be represented well by a single normal distribution. The parameters of the fit have been determined at 99% confidence level.

models shows some signs of developing an asymmetry as the observations whereas the T30 model appear to be rather symmetric, resembling a pure normal distribution.

The results can also be understood in terms of the two gaussians composing the probability distribution. If we plot the individual states, combined with the weights obtained from the fit, we get Fig.3.4. The probability of a particular observed value can therefore be understood as the probability of being in one state or the other. It is interesting to note that the variability in the T30 case is so poor that the second state is almost disappearing, indicating that in fact there is little difference from a simple normal distribution with zero mean in this case.

We can shed some light on the interpretation of these results by considering some

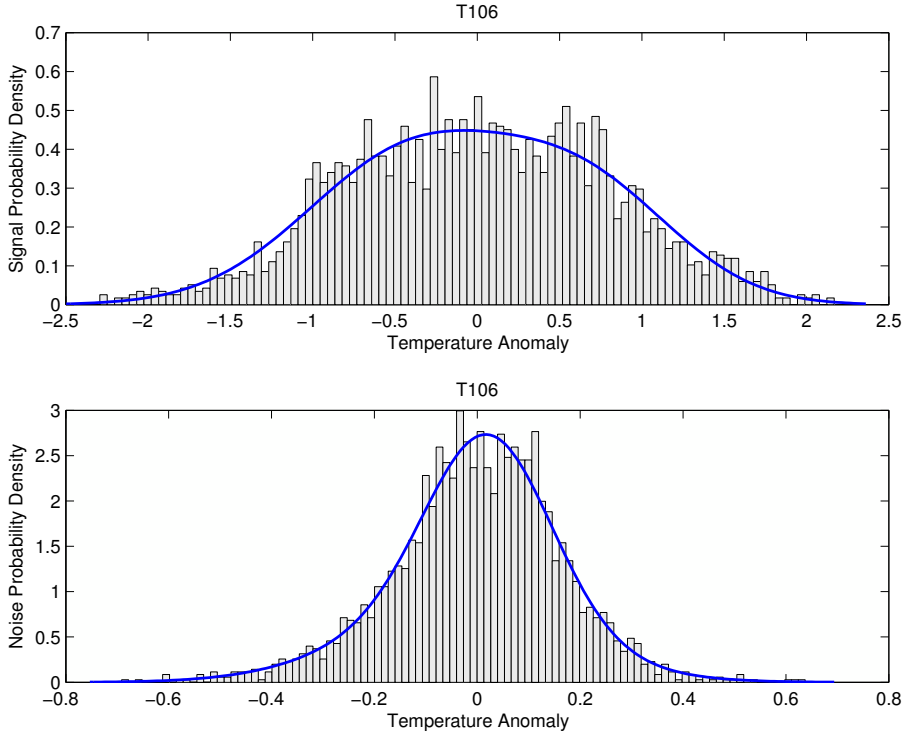

Figure 3.2: As in Fig.3.1, but for the monthly mean NINO3 index obtained from a 200-years simulations of the CMCC coupled spectral T106 model (Navarra et al., 2008; Gualdi et al., 2003)

simple idealized cases. Let us consider the case of an oscillation on which some gaussian white noise with zero mean is added (top panel, Fig.3.5). The time series of the oscillation shows variability, but the probability histogram has a noticeable two peak structure, that can be readily identified as two separate states. However, the states are symmetric, both in the location of their maximum and in the amount of probability they explain. The two states are equally probable. The result is rather insensitive to the amount of noise, as the histogram in this case easily capture the signature of the underlying oscillation even in the case of strong noise (not shown). As the noise becomes dominant the probability distribution loses track of the oscillation showing only the gaussian distribution of the noise. The result is rather insensitive to the particular shape of the oscillation, a square wave yields the same symmetric two-peak result, with a better separation between the peaks due to the faster transition between high and low states.

The only way to get an asymmetric distribution like the observations, within the as-

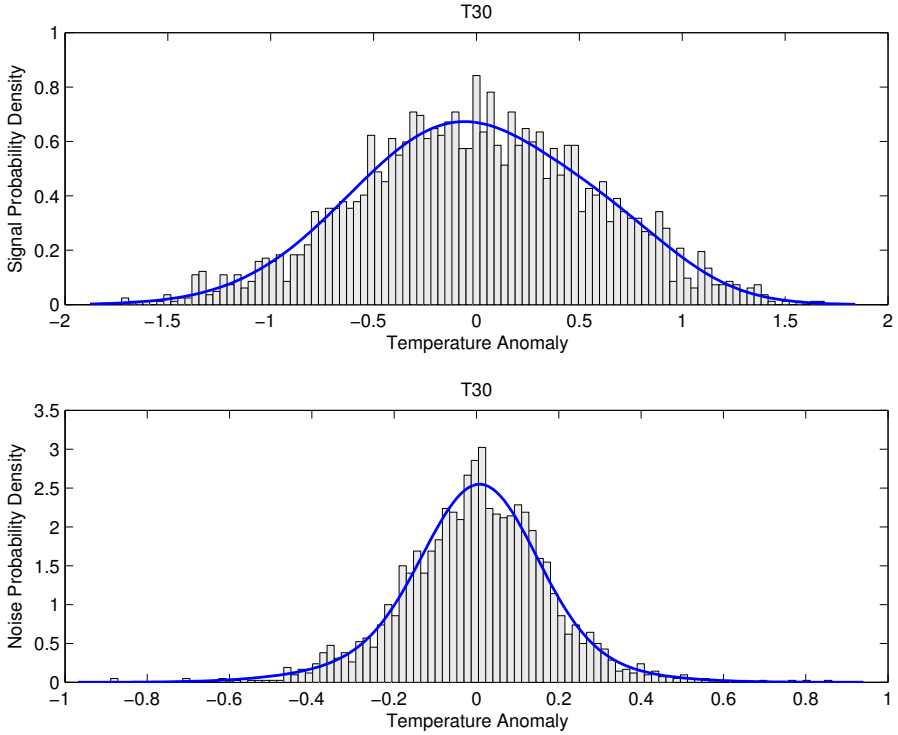

Figure 3.3: As in Fig.3.1, but for the monthly mean NINO3.4 index obtained from a 200-years simulations of the CMCC coupled spectral T30 model (Navarra et al., 2008; Gualdi et al., 2003)

sumptions of additive gaussian white noise and a two state ENSO, is to allow different resident times in the two different states. Fig.3.6 shows the same as in Fig.3.5 but in this case the noise has been superposed onto a square wave with different lengths of the extreme states. We can see how the asymmetry can be easily identified and the relative weight of the states found. The probability distribution signature of a pure oscillation can also easily be identified, even if there is a considerable amount of noise superposed. The observation seems to indicate the asymmetry is intrinsic and cannot be explained with stochastic forcing.

Visual inspection of the T30 time series will not give the same impression and also a false impression can be obtained from spectral analysis of the same experiments (Navarra et al., 2008) that yields peaks with some significance. In reality there is almost no oscillations in the case of the T30. This simple diagnostic is also showing a very powerful method to evaluate the quality of the performance of models.

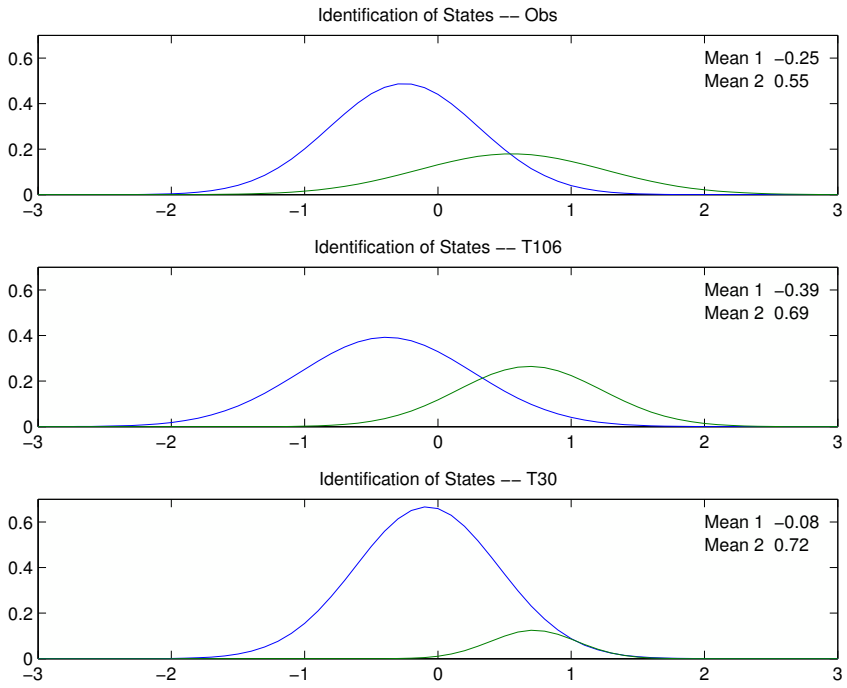

Figure 3.4: Representation of the two normal distribution entering the best fit in the previous pictures. The gaussians are well separated and they can be interpreted as possible states of the system. The pictures shows estimated states for Observations (top), T106 model (middle) and T30 (bottom). We can interpret the warm states as El Niño and and the cold state as La Niña .

3.3 An equation for the probability distribution

We will describe in this section how we can formulate an equation that will allow us to investigate the properties of the probability distribution itself. In general terms a system describing ENSO and an additive stochastic forcing can be written as a Langevin-like equation:

$$\dot{x}_\mu(t) = f_\mu(\mathbf{x}(t)) + \sqrt{Q}\epsilon_\mu(t) \tag{3.2}$$

where $\mathbf{x}(t) = (x_1(t), \cdots, x_K(t))$ represents the instantaneous state of the system and $f_\mu(\mathbf{x})$ a differentiable function of $\mathbf{x}$ for $\mu = 1, ..., K$. The noise functions $\epsilon_\mu(t)$ are defined by their correlation functions as

$$\gamma_{\mu\nu}(t, t') = \langle \epsilon_\mu(t)\epsilon_\nu(t')\rangle_\epsilon = 2Q\delta_{\mu\nu}\delta(t - t') \tag{3.3}$$

and they have zero means, $\langle . \rangle_\epsilon$ is an average with respect to the probability distribution

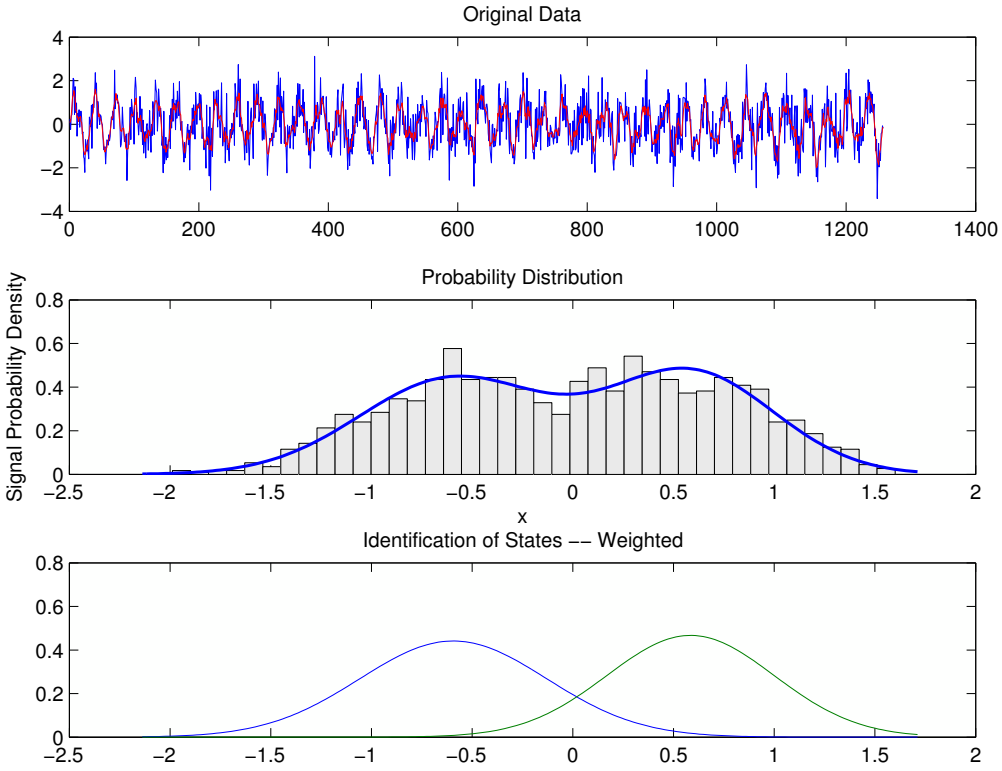

Figure 3.5: A time series for a sinusoidal oscillations with noise (top) for an arbitrary frequency and unit amplitude.The estimated probability distribution show clearly two peaks (middle), that can be readily identified as two symmetric, equal-amplitude states (bottom).

of the realizations of the stochastic variables $\epsilon_\mu(t)$.

3.3.1 The Fokker-Planck equation

We are interested in the transition probability distribution for the stochastic process $P(\mathbf{x}, t, \mathbf{x}_0, t_0)$, describing the probability for the system to be in $\mathbf{x}$ at time t, given that it was in $\mathbf{x}_0$ at time t_0. In what follows we shall often omit the dependence on the initial data and use the simplified notation $P(\mathbf{x}, t)$. Using the gaussian nature of the noise it is possible to write a Fokker-Planck equation for $P(\mathbf{x}, t)$ (Risken, 1989) with an implied summation over repeated indices:

$$\frac{\partial P(\mathbf{x},t)}{\partial t} = \frac{\partial}{\partial x_\mu}\left[Q\frac{\partial P(\mathbf{x},t)}{\partial x_\mu} - f_\mu(\mathbf{x})P(\mathbf{x},t)\right]. \tag{3.4}$$

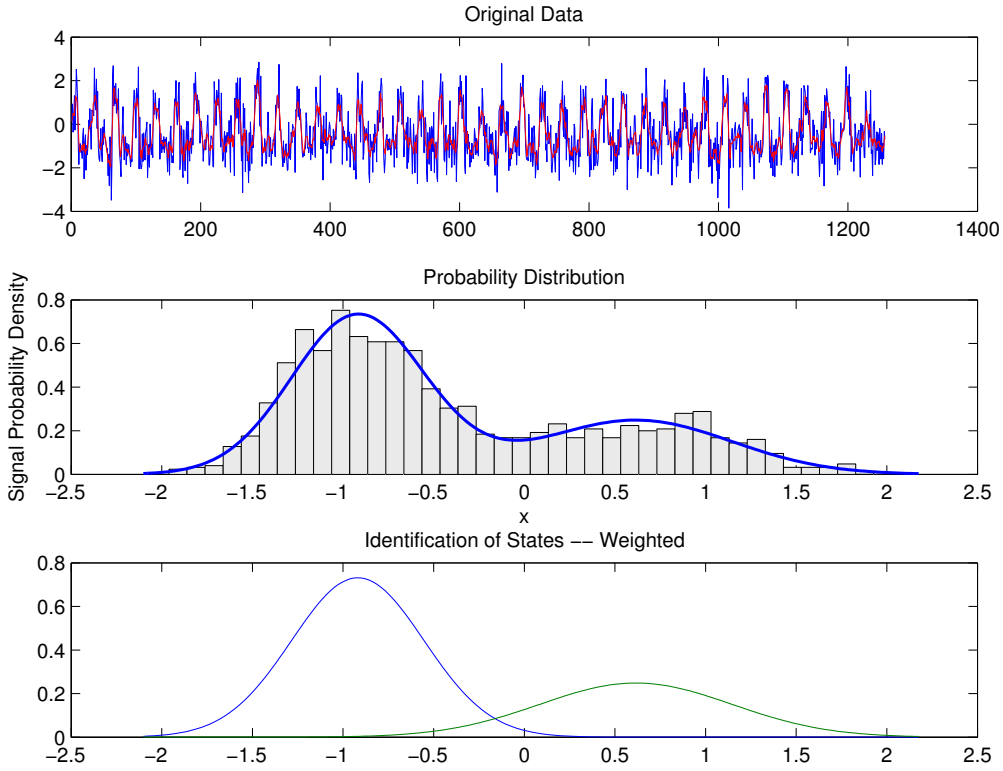

Figure 3.6: The same as in Fig.(3.5), but for the case of a square wave of the same frequency and amplitude, but with different staying time for the positive and negative values.

The Fokker-Planck equation can be written also for multiplicative noise, but we will consider only the additive case here, Q represent here a constant diffusion coefficient while f_μ is the drift term. In principle, the solution of this equation contains all the information we need on the probability distribution and its evolution in time, but explicit solution can often be very difficult except simple cases. However, we might see the situation from a different angle, by realizing that the solution of this equation can be written as a path integral (Haken, 1976; Navarra et al., 2012)

$$P(\mathbf{x},t) = \int [\mathcal{D}\mathbf{x}(\tau)] \exp(-S(\mathbf{x}))P(\mathbf{x},t_0) \tag{3.5}$$

where the integration is done over all paths $\mathbf{x}(t)$ that go from an initial state x_0 at time t_0 to a final state x_f at time t_f. The functional $S(\mathbf{x})$ is the continuous Onsager-Machlup action that can then be defined in the white noise case as

$$S(\mathbf{x}) = \frac{1}{4Q}\int_0^{t_f} \Big[[\dot{x}_\mu - f_\mu(\mathbf{x})]\delta_{\mu\nu}[\dot{x}_\nu - f_\nu(\mathbf{x})] + 2Q\frac{\partial f_\mu}{\partial x_\mu}\Big]dt. \tag{3.6}$$

The extra divergence term in the action is generated by the difficulty of defining the derivative of a stochastic process and it corresponds to the choice of the Stratonovich differentiation for the stochastic process. It is worthwhile to mention here that the introduction of noise into a differential equation changes profoundly the character of the equation. In particular individual realizations have little meaning and it opens a classification between quantities that can be measured in a repeatable and consistent manner (observables) and quantities that cannot really be measured.

Equation (3.4) can be solved by separating the time dependence and solving a stationary problem:

$$P(x,t) = \sum_{n=0}^{\infty} \exp\left(-\lambda_n t\right) \phi_n(x,t) \tag{3.7}$$

Where the ϕ are the eigenfunctions and eigenvalues of the Fokker-Planck stationary operator

$$L_{FP} = \frac{\partial}{\partial x_\mu} Q \frac{\partial}{\partial x_\mu} - \frac{\partial}{\partial x_\mu} \left[f_\mu(\mathbf{x})(.) \right] \tag{3.8}$$

L_{FP} is not self adjoint and therefore we would need to consider also the eigenvectors of its adjoint. However, a self-adjoint system can be obtained if the drift term can be expressed in terms of a drift potential $U(x,t)$ according to $f_\mu = -\frac{\partial U(x,t)}{\partial x_\mu}$. In this case it is then possible to use the transformation

$$P(x,t) = \exp\left(-\frac{U(x)}{2Q}\right) \psi(x,t), \tag{3.9}$$

obtaining

$$\frac{\partial \psi}{\partial t} = L\psi = Q\frac{\partial^2 \psi}{\partial x^2} - V(x)\psi, \tag{3.10}$$

where

$$V(x) = \frac{1}{4Q}\left(\frac{\partial U(x)}{\partial x}\right)^2 - \frac{1}{2}\frac{\partial^2 U(x)}{\partial x^2} \tag{3.11}$$

The operator L is now selfadjoint and it has the same eigenvalues as L_{FP},. Their eigenfunctions are linked so that

$$\phi_n(x) = \exp\left(-\frac{U(x)}{2Q}\right) \psi_n(x) \tag{3.12}$$

and they form an orthonormal system such that

$$\int \psi_n \psi_m dx = \int \exp\left(\frac{U(x)}{Q}\right) \phi_n \phi_m = \delta_{mn} \tag{3.13}$$

The operator L can be expressed in a compact way as

$$L = -\hat{a}a \tag{3.14}$$

where

$$a = \sqrt{Q} \exp\left(-\frac{U}{2Q}\right) \frac{\partial}{\partial x} \exp\left(\frac{U}{2Q}\right) \tag{3.15}$$

$$\hat{a} = -\sqrt{Q} \exp\left(\frac{U}{2Q}\right) \frac{\partial}{\partial x} \exp\left(-\frac{U}{2Q}\right) \tag{3.16}$$

The existence of stationary solutions depends on the asymptotic behavior of the potential $V(x)$. For natural boundary conditions where the potential goes to very large values for $x \to \infty$ the operator $\hat{a}$ becomes the adjoint of a and stationary states exist. However, also in the opposite case when the potential becomes very negative it is possible to find eigenfunction and eigenvalues.

Defining the eigenfunction and eigenvalues of L as

$$L\psi_n = -\lambda \psi_n \tag{3.17}$$

we can write the transition probability as

$$P(x, t|x't') = e^{(U(x)-U(x'))/2Q} \sum_n \psi_n(x)\psi_n(x')e^{-\lambda_n(t-t')}. \tag{3.18}$$

The transition probability allows us to compute all the joint probability distributions that express the probability W_n of the system assuming the values (x_1, t_1), (x_2, t_2), ..., (x_n, t_n). There is an infinite hierarchy of joint distribution factors that collectively defines the property of the stochastic system, however for a Markov system all the higher order W's can be obtained from the 2-point distribution W_2 that describes completely

the system at equilibrium according to

$$W_2(x,t|x',t') = P(x,t|x',t')W_{st}(x') \qquad t \geq t' \tag{3.19}$$

where W_{st} is the stationary distribution, corresponding to the eigenvalue zero. It is easy to show that a solution of the eq. 3.8 for the eigenvalue zero is:

$$W_{st}(x) = exp\left(-\frac{U(x)}{2Q}\right). \tag{3.20}$$

However, such a solution exists only for suitable boundary conditions. The so called natural boundary conditions correspond to the potential going to very large values as $|x| \to \infty$, reflecting boundary conditions requiring $\psi \to 0$ can then guarantee the existence of a stationary solution.

In terms of eigenfunctions and using the explicit form of the stationary solution we get

$$W_2(x,t|x't') = e^{(U(x)+U(x'))/2Q} \sum_n \psi_n(x)\psi_n(x')e^{-\lambda_n(t-t')} \tag{3.21}$$

and the correlation function is therefore given by the expectation value

$$< x(t+\tau)x(t) >= \int\int xx'W_2(x,t+\tau|x',t)dxdx' \tag{3.22}$$

The expectation value of any function $g(x,t)$ can be readily calculated as follows

$$\langle g(x,t)\rangle = \int_{-\infty}^{\infty} g(x,t)P(x,t)dx \tag{3.23}$$

in a similar way one can obtain $\langle f(x)\rangle$, simply integrating over time.

3.3.2 The relation with the Schrödinger equation

The modified form of the FP (3.10) is suggestive of a possible link to other applications in physics. It closely resembles the Schrödinger equation used in quantum mechanics and this observation is maybe worth investigating a little bit more since both equations describe the evolution of probability or of quantities closely related to it. There is also another reason to look further in this relation. There are an enormous amount of methods developed to deal with problems involving the Schrödinger

equation and a multidecadal expertise in discussing the concepts and interpretations required. The potential of trying to use some of this wealth for application in our field is simply too large to ignore.

The detail of the relation linking the two equations can be made explicit. The Schrödinger equation for a point particle of mass m can be written as

$$i\hbar\frac{\partial\psi_S}{\partial t} = \frac{-\hbar^2}{2m}\frac{\partial^2\psi_S}{\partial x^2} + V(x,t)\psi_S, \tag{3.24}$$

where m is the mass of the particle, $\hbar$ is the Planck constant divided by 2π and ψ_S is the quantum wave function.

An analytical continuation of the time $t = -i\tau$ (sometimes known as *Wick's rotation* in the physics literature) will transform this form of the Schrödinger equation into

$$\frac{\partial\psi_S(x,\tau)}{\partial\tau} = \frac{\hbar}{2m}\frac{\partial^2\psi_S(x,\tau)}{\partial x^2} - \frac{1}{\hbar}V(x,\tau)\psi_S(x,\tau), \tag{3.25}$$

We can recover (3.10) in form by substituting $\frac{\hbar}{2m} \rightarrow Q$ and rescaling the potential V by $\hbar$. It is interesting to note that the stochastic parameter Q plays the same role than Planck's constant $\hbar$. They are the controlling parameters of the uncertainty of the system. The limit $Q \rightarrow 0$ will yield the deterministic solution of the evolution equations in a similar sense that the limit $\hbar \rightarrow 0$ yields the classical (deterministic) solutions in the case of Schrödinger equation.

The remaining difference is the interpretation of the wave function ψ_S. The probability distribution can be obtained from to the solution of (3.24) by $P_S = |\psi_S|^2$ whereas the solution of the Fokker-Planck equation (3.10) is directly the probability distribution itself. Therefore the evolution of the probability for a stochastic system is given by a Schrödinger -like equation, but whose solution ψ represents the probability distribution itself (scaled by an exponential factor), rather than its density.

3.4 A self-excitation ENSO model with a cubic nonlinear term

A simple model of the ENSO system based on the recharge theory was proposed by Jin (1997a). The model is a nonlinear system in terms of nondimensional variables T, h. T is representing the anomaly SST in the Eastern Pacific, whereas h is the anomaly of

the depth of thermocline in the Western Pacific.

$$\begin{aligned} \frac{dh}{dt} &= -rh - \alpha\mu b_0 T \\ \frac{dT}{dt} &= (\gamma\mu b_0 - c)T + \gamma h - (bT + h)^3 \end{aligned} \tag{3.26}$$

The coupling strength will be measured by a parameter μ according to $\tau = b_0\mu T$. μ measures the strength of the interaction between the SST and the wind stress relative to a scale b_0. The parameters can then be expressed as non-dimensional values $c = 1, \gamma = 0.75, r = 0.25, \alpha = 0.125, b_0 = 2.5$ using the same choices of scales made by Jin (1997a).

Jin (1997a) studied the bifurcation diagram of the stationary solution of this system as a function of the interaction parameter μ and he found that the system has a single oscillatory solution for values of $\mu < 16/15$ and then two exponential solutions that are stable for large values of $\mu > 19/15$. The delayed oscillator theory focus on the parameter space below this threshold that allows oscillations and therefore the appearance of something like an ENSO cycle, but the introduction of stochastic noise also makes the regime with stable stationary states capable producing ENSO variability. They also investigated the behavior of the system under a stochastic forcing of strength Q, but still with a linear system to describe ENSO.

The addition of gaussian white noise to the two equations in (3.39) will allow the system to vacillate between one stable point and the other. Fig.3.7 and Fig.3.8 show the trajectory for increasing values of the noise strength Q. The corresponding probability distributions are peaked in correspondence of the stationary points (not shown). The fluctuation between the two stable states can be clearly seen and also the degradation of the bimodal nature of the distribution as the noise gets large, making the transition from one stable point to the other much easier. For larger values of the noise a completely normal distribution can be reached.

The variations of the trajectory are however confined and the path taken by the variables from one point to the other seems rather limited in a direction normal to the line joining the two centers. This suggests that if we could transform variables in such

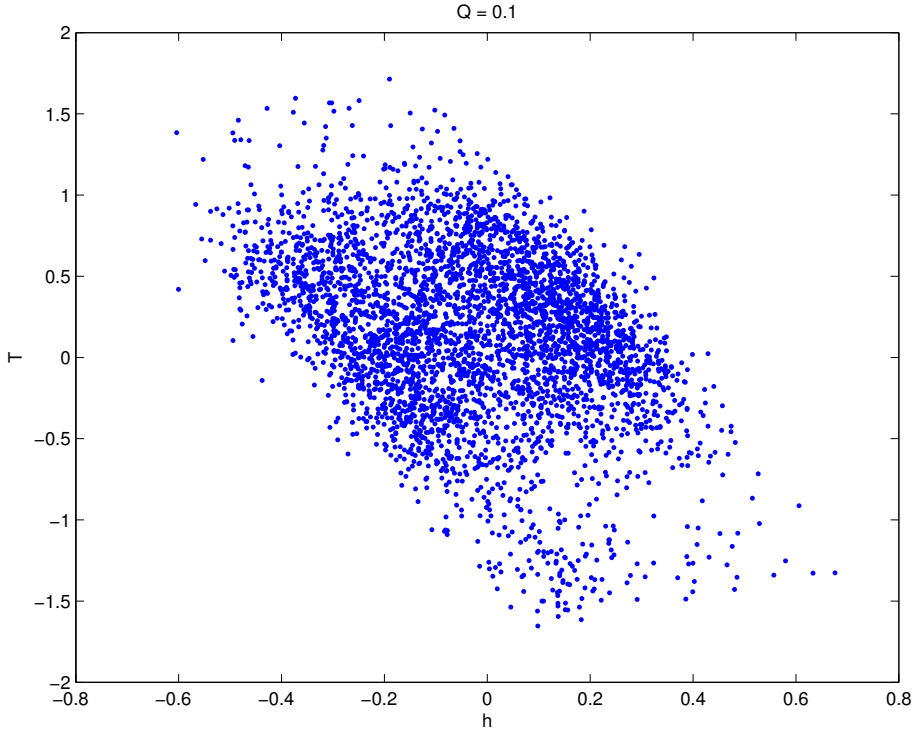

Figure 3.7: Trajectory plot of a solution from (3.39) considering noise. $Q = 0.1$, $\mu = 21/15$.

a way to introduce new variables (θ, z), obtained with a rotation

$$\begin{aligned} h &= z + \tfrac{0.8\theta}{\mu} \\ T &= \theta - \tfrac{0.8\, z}{\mu} \end{aligned} \tag{3.27}$$

we will be able transform the system in such a way that the stationary states in the (z, θ) coordinates are given by

$$(0,0) \quad (\frac{1}{2}\sqrt{\frac{15\mu - 16}{5}}, 0) \quad (-\frac{1}{2}\sqrt{\frac{15\mu - 16}{5}}, 0) \tag{3.28}$$

along the z axis. We can then transform the system to a single equation for z by assuming that $\theta \approx 0$. This approximation implies that $h \approx z$ and $T \approx -\frac{\mu}{0.8} z$ that is consistent with the solution of the original system (3.39) as described in (Jin, 1997a).

We can now apply the arguments developed in Section 3.3. Using the approximations just described we can get a one-variable stochastic equation:

$$\dot{z} = f(z) + \sqrt{Q}\epsilon(t), \tag{3.29}$$

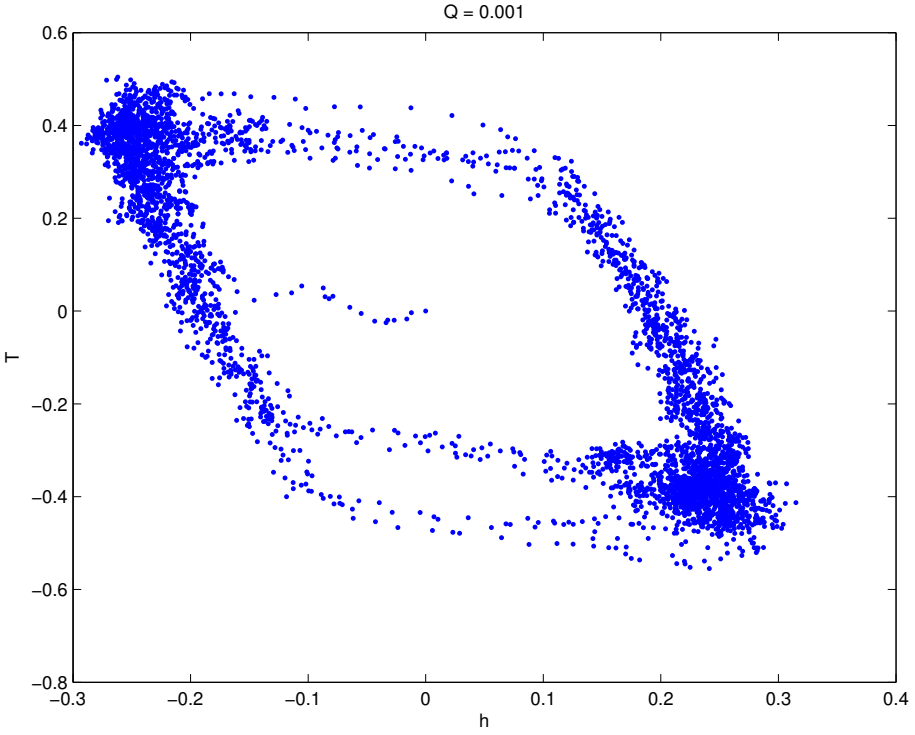

Figure 3.8: Trajectory plot of a solution from (3.39) considering noise. $Q = 0.001$, $\mu = 21/15$.

with

$$f(z) = \frac{z(-80\mu z^2 + 60\mu - 64)}{100\mu^2 + 64} \tag{3.30}$$

defining the parameters,

$$\beta^2 = \frac{60\mu - 64}{200\mu^2 + 128} \qquad \delta^2 = \frac{40\mu}{60\mu - 64}. \tag{3.31}$$

we can get a compact form

$$f(z) = -4\beta^2\delta^2 z^3 + 2\beta^2 z \tag{3.32}$$

This forcing function $f(z)$ admit a potential $U(z)$ that can be obtained from $f(z)$ by integration

$$U(z) = -\int f(z)dz = \beta^2 z^2(\delta^2 z^2 - 1), \tag{3.33}$$

and therefore we can use the self-adjoint form of the Fokker-Planck equation (3.10)

$$V(x) = \frac{1}{4Q}\left(\frac{\partial U(x)}{\partial x}\right)^2 - \frac{1}{2}\frac{\partial^2 U(x)}{\partial x^2} \tag{3.34}$$

that in our case becomes

$$V(z) = 250\big(2\,\beta^2\delta^2 z^3 + 2\beta^2 z\left(\delta^2 z^2 - 1\right)\big)^2 + \beta^2 - 6\beta^2\delta^2 z^2 \tag{3.35}$$

The complete Fokker Planck equation for our simple model can then be written as

$$\frac{\partial\psi}{\partial t} = Q\frac{\partial^2\psi}{\partial z^2} - \Big[250\big(2\,\beta^2\delta^2 z^3 + 2\beta^2 z\left(\delta^2 z^2 - 1\right)\big)^2 + \beta^2 - 6\beta^2\delta^2 z^2\Big]\,\psi. \tag{3.36}$$

The probability distribution can be obtained from the solutions of (3.36) via

$$P(x,t) = \exp\left(-\frac{U(z)}{2Q}\right)\psi(z,t). \tag{3.37}$$

The one dimensional system has an oscillatory solution for $\mu < 16/15$ and two stable solutions for $\mu > 16/15$. There is also a critical point at $z = 0$ that is stable for $\mu < 16/15$ that becomes unstable for $\mu > 16/15$. The dependence of the potential on the coupling parameter is shown in Fig.3.9. Crossing the threshold at $16/15$ reveals a couple of symmetric stable points whose separation increases with μ. The depth of the two potential wells is identical and the height of the central barrier also increases with increasing values of the coupling.

The solution for the Fokker Planck equation is a transition probability density distribution that can be expressed in terms of eigenfunctions. The eigenfunctions of the transformed operator L are a complete set and they allow the representation of any initial probability but because of the positive definite nature of the probability every initial condition will always be a mixture of different eigenfunctions. The first five eigenfunctions transformed back using (3.12) to the eigenfunction of L_{FP} are shown in Fig.3.10. They basically represent an ascending order of orthogonal functions sampling the region around the potential. Except for the mode corresponding to the eigenvalue zero, i.e. the stationary solution, they all have oscillatory character.

It is important to note here that the solution cannot collapse to a single oscillatory eigenvector because only combinations of eigenvectors that preserve the positive definiteness of the probability distribution will be described by the equation.

The different stationary solution obtained for various values of μ are shown in Fig.3.12. The probability has a single maximum for values below the threshold where

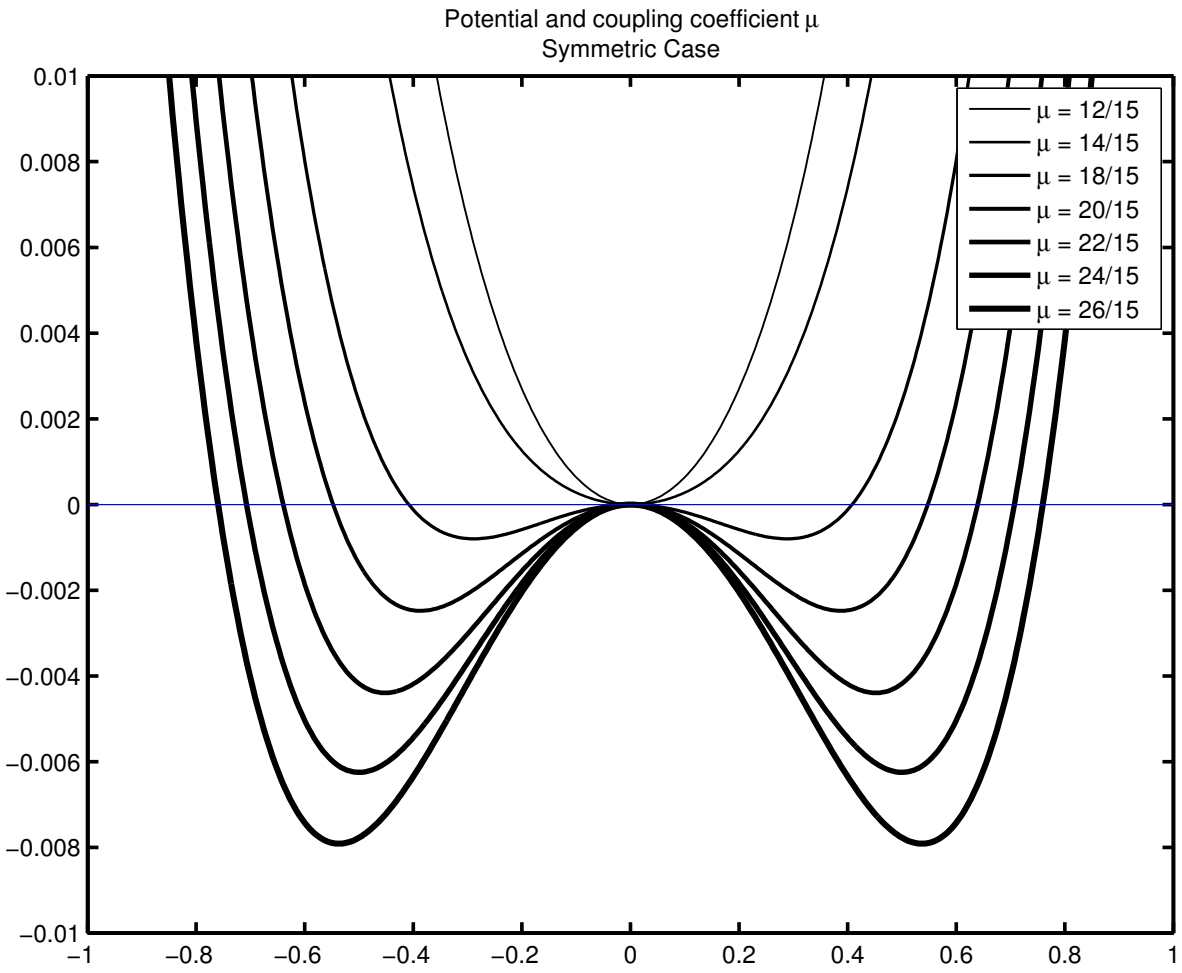

Figure 3.9: The dependence of the potential of the one-dimensional model from the coupling parameter μ. The symmetry is broken for $\mu = 16/15$, for values larger the potential has two stable points in symmetric positions with respect to the ordinate axis. The separation increases with increasing values of the coupling.

there is only one critical point and an oscillation, but they become a doublet when μ is large. The dependence from the value of the noise, Q, can be easily guessed from (3.20): large values of the noise will tend to flatten and eliminate the double peaks, resulting in a single normal distribution centered at the origin. The stationary density probability distribution from the one-dimensional model is therefore very consistent with the probability distribution obtained from the numerical experiments.

The evolution of the probability density distribution can be obtained from the tran-

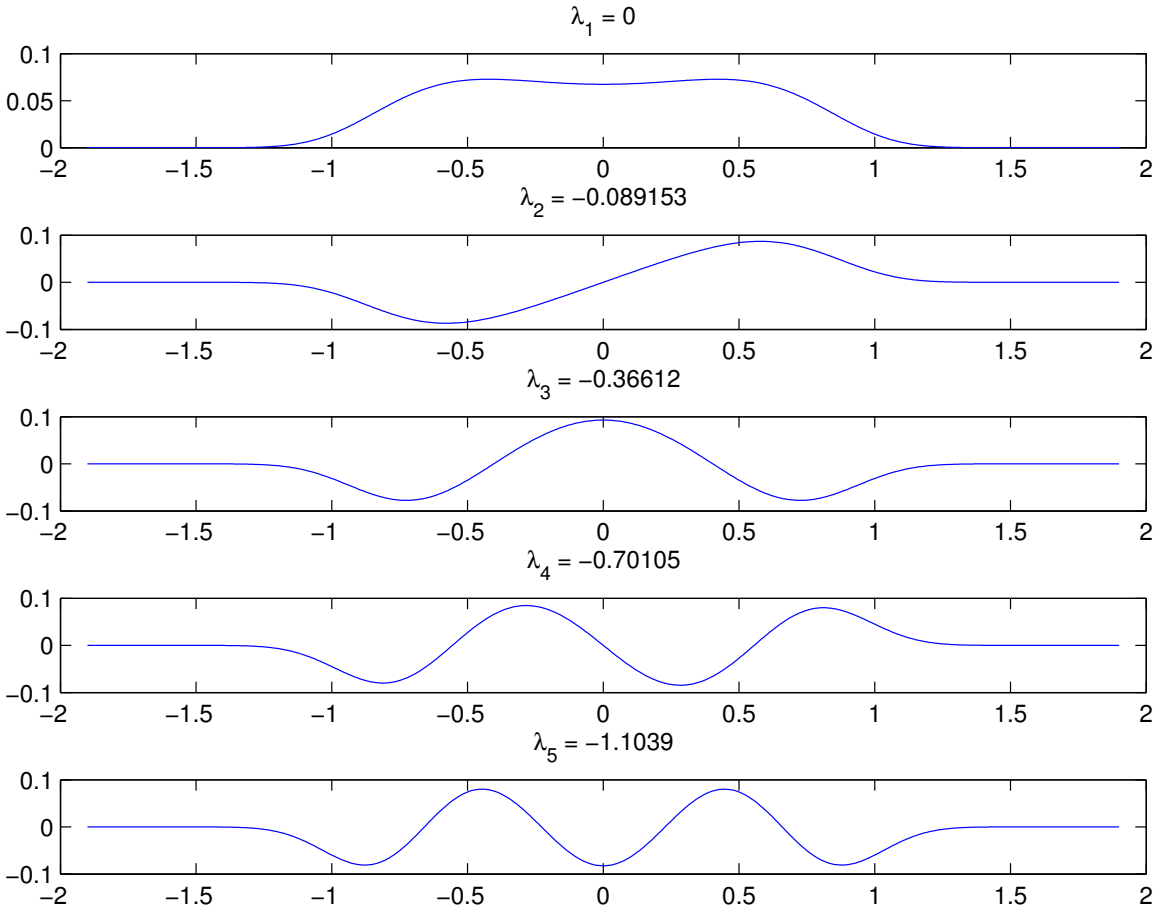

Figure 3.10: The first five eigenfunction for the symmetric case. The first eigenfunction corresponds to the eigenvalue zero and therefore is the stationary distribution.

sition probability (3.18) as

$$W(x,t) = \int P(x,t|x',0)W_{IC}(x',0)dx' \tag{3.38}$$

Fig.3.13 shows the evolution of the probability for an initial distribution centered at $x = -0.7$. The coupling is set at $\mu = 21/15$ and it generates a rather well defined potential with a high barrier. For this value of the noise ($Q = 0.15$) the stationary solution is still not fully achieved at a final time of 60 months.

Several factors can influence the evolution for a given value of the coupling coefficient. Increasing the strength of the forcing will make easier the transition to the

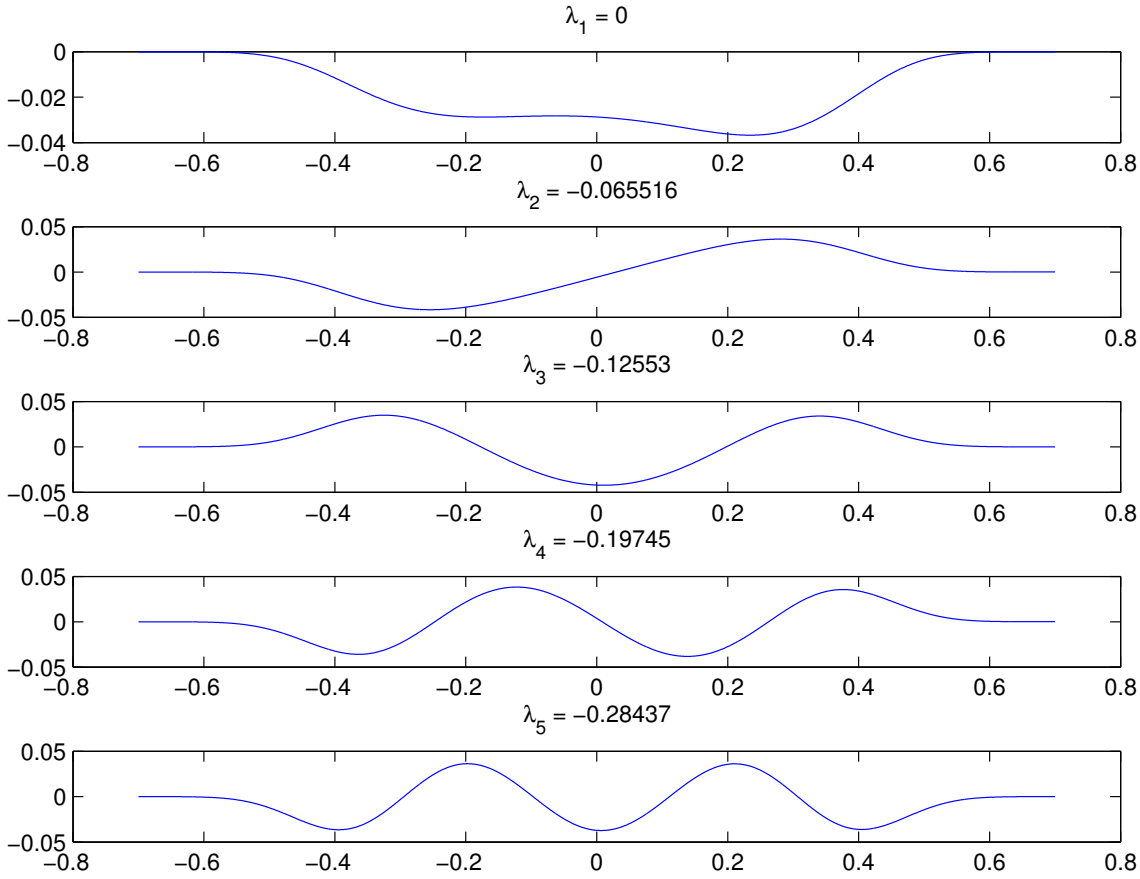

Figure 3.11: As in Fig.3.10 but for the asymmetric case

neighboring potential well, resulting in a faster convergence to the stationary state. Localization of the initial condition also affects the following evolution. In general, a well localized distribution will have a slower transition outside of the region where the stationary solution exist, like those in Fig.3.13 will have a slower evolution. An extremely localized distribution,$\delta(x)$ will project equally on all eigenfunctions and the convergence to the zero eigenvalue will be influenced by higher eigenvalues with long decay scales. On the other hand, an initial condition that projects better on the slower mode will have a faster evolution (Fig.3.14) showing a rapid convergence to the equilibrium distribution.

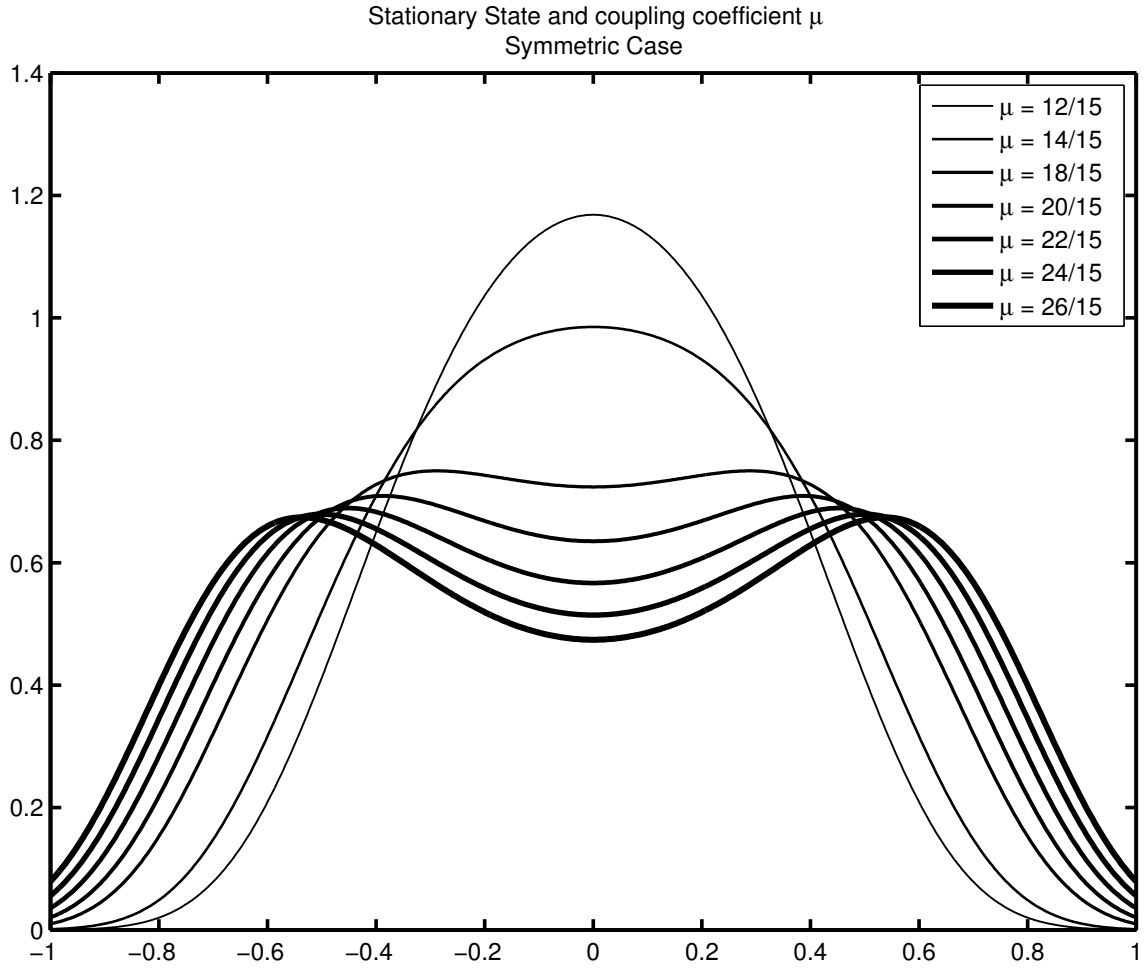

Figure 3.12: The stationary solution for the probability distribution for various values of the coupling parameter μ. The solution is unimodal for values below the threshold and becomes bimodal for stronger coupling. It follows of course closely the potential distribution in Fig.3.9 according to Eq. 3.20.

3.5 The origin of the asymmetry

The model shown in the previous section shows some of the aspects of the El Niño variability, but it lacks the difference between cold and warm states that the observations have (Fig.3.1). An et al. (2005); An and Jin (2004) have proposed that the effects of the neglected nonlinear terms in the advection can explain some of the amplified magnitude that warm events show. Intraseasonal variations in convection has also received considerable attention for the forcing that they can exert, once their effects is rectified in the seasonal mean, to the inter annual variability.

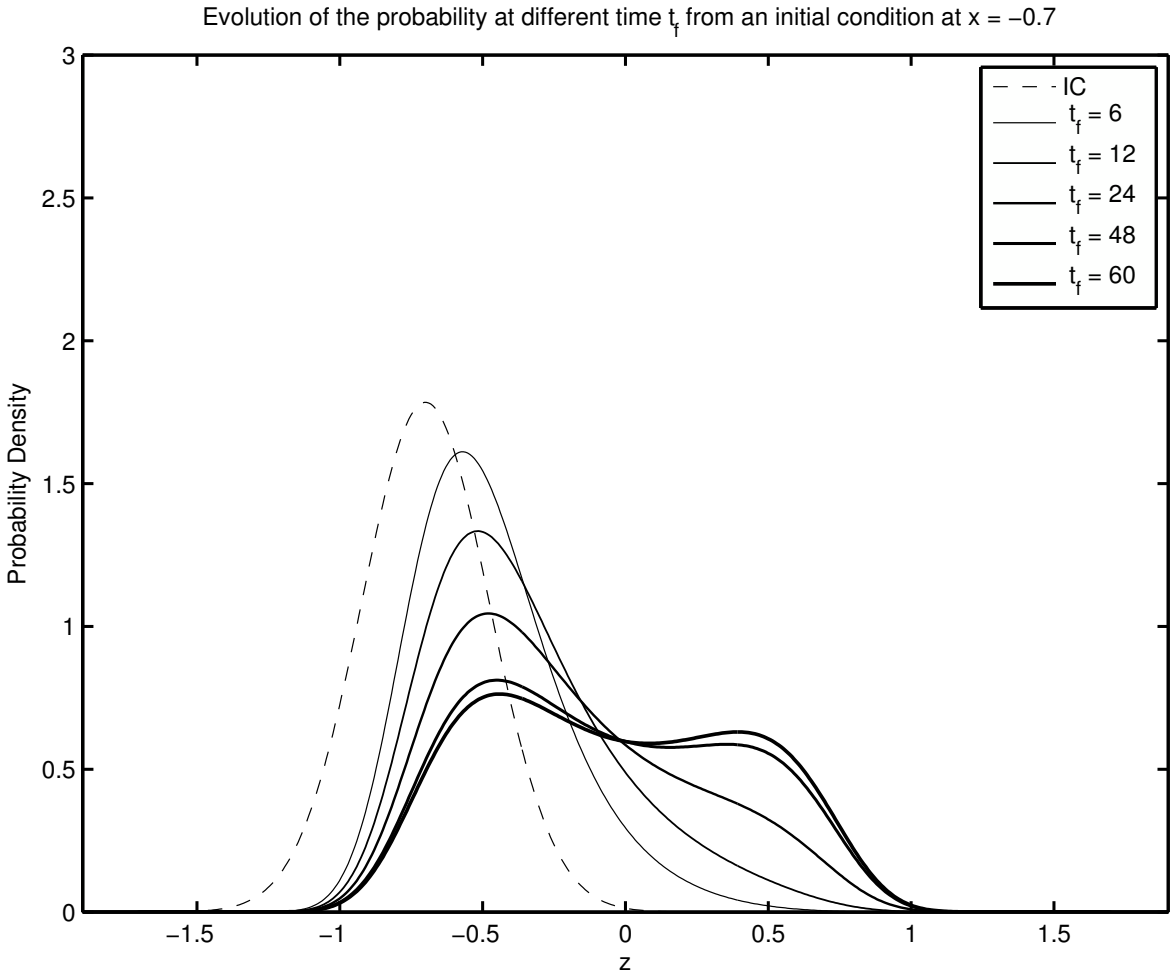

Figure 3.13: The evolution of the probability distribution for an initial distribution centered at $x = -0.7$ and for different times in months. The value of the coupling constant used here ($\mu = 21/15$) and the level of the stochastic forcing ($Q = 0.15$) result in a time to achieve the stationary distribution of about 60 months.

The Madden-Julian Oscillation, in particular has been the subject of observational and modeling studies. In general, it has been considered to be a component of the stochastic forcing, however, it does seem to have a systematic, rather than stochastic effects on the anomaly SST in the Eastern Pacific. Zhang and Gottschalck (2002) and Zhang (2001) have shown that it is the seasonal activity of the MJO that is correlated with positive SST anomalies in the East Pacific. These results implies that the rectified effect of the MJO is rather of one sign, tending to push the system towards warmer states. This systematic effect seems to indicate that it is more reasonable to extract the

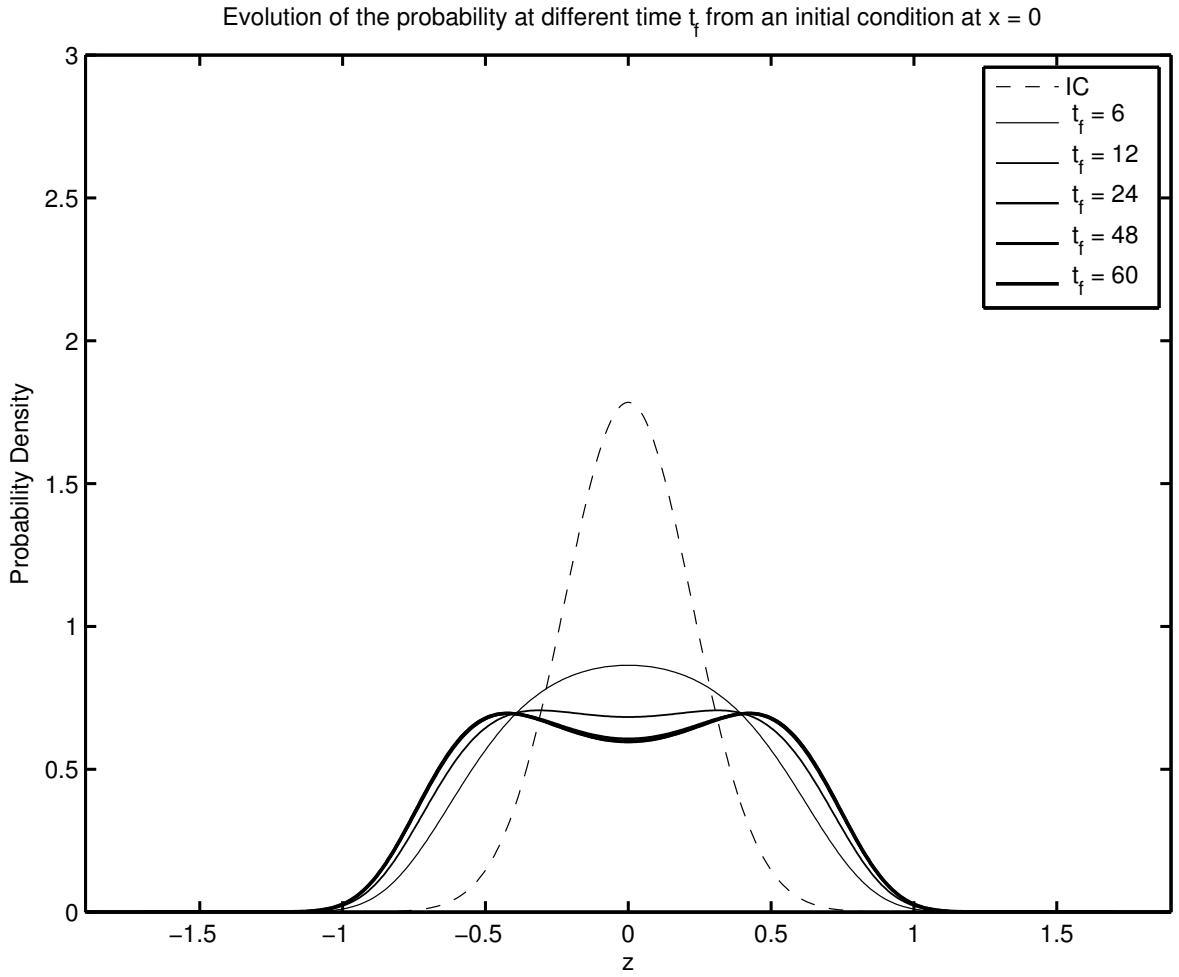

Figure 3.14: As in Fig.3.13, but for an initial distribution centered at $x = 0$.

MJO from the stochastic forcing and try to reproduce its effect more directly.

The nonlinear system (3.39) can then be easily modified to take into account the effect of the MJO by adding a constant term in the temperature equation. However, this would not be consistent with the dynamics of the MJO perturbation on the equatorial pacific ocean. A simple constant in the temperature equation will force a change in the thermocline depth of opposite sign, as it is required by the inter-annual dynamics. In order to get a constant response it is necessary to add a term also in the thermocline equation in order to represent the change in depth produced at seasonal scales by the MJO forcing. The model equations (3.39) can therefore be modified adding a constant term γ_T in the temperature equation and another constant term γ_h in the thermocline

equation such as

$$\begin{aligned} \frac{dh}{dt} &= -rh - \alpha\mu b_0 T + \gamma_h \\ \frac{dT}{dt} &= (\gamma\mu b_0 - c)T + \gamma h - (bT + h)^3 + \gamma_T. \end{aligned} \tag{3.39}$$

It is still possible to obtain a one-dimensional model such that:

$$\dot{z} = \frac{\left(25\mu^2\gamma_h - 20\mu\gamma_T\right)}{25\mu^2 + 16} + z\frac{(15\mu - 16)}{25\mu^2 + 16} - z^3\frac{20\mu}{25\mu^2 + 16} \tag{3.40}$$

The scale of the constants can be derived from the observations (Zhang, 2001) and it is estimated to be of the order of $0.1C$ at seasonal scale for the SST and of the order of $2m$ for the average effect on the thermocline.

The potential that can be obtained using the above constant is shown in Fig.3.15. The presence of the MJO breaks the symmetry and makes the potential well for the warm stable case deeper. (The variable z is proportional to the negative of the temperature anomalies). Increasing the coupling intensifies the asymmetry and the separation between the states, making it more difficult to overcome the central barrier.

Breaking the asymmetry creates a different situation, The initial condition at neutral conditions ($x = 0$) in Fig.3.16 is showing a faster adjustment to the the equilibrium than the previous case. This is more evident in the initial condition centered at $x = -0.7$ (Fig. 3.17) that is showing clear signs of a faster transition, even if it is yet not completely finished at 48 months. The inspection of these solutions seems to indicate that breaking the symmetry has changed the structure of the eigenvalues that represent the inverse time scales of the evolution of each eigenfunction.

It is possible to analyse the dependence of the skewness of the theoretical distribution as a function of the coupling parameter μ. Table 3.1 shows the skewness, computed as the normalised third moment of the distribution, for increasing coupling strength. The value for the observations based on the NINO3.4 set already used in the paper is also shown at the bottom. The skewness is largely a function of the coupling parameter and of the symmetry parameter γ, whereas for larger values of the noise it tends to become smaller. Realistic values of skewness can be obtained within the parameter range of the coupling.

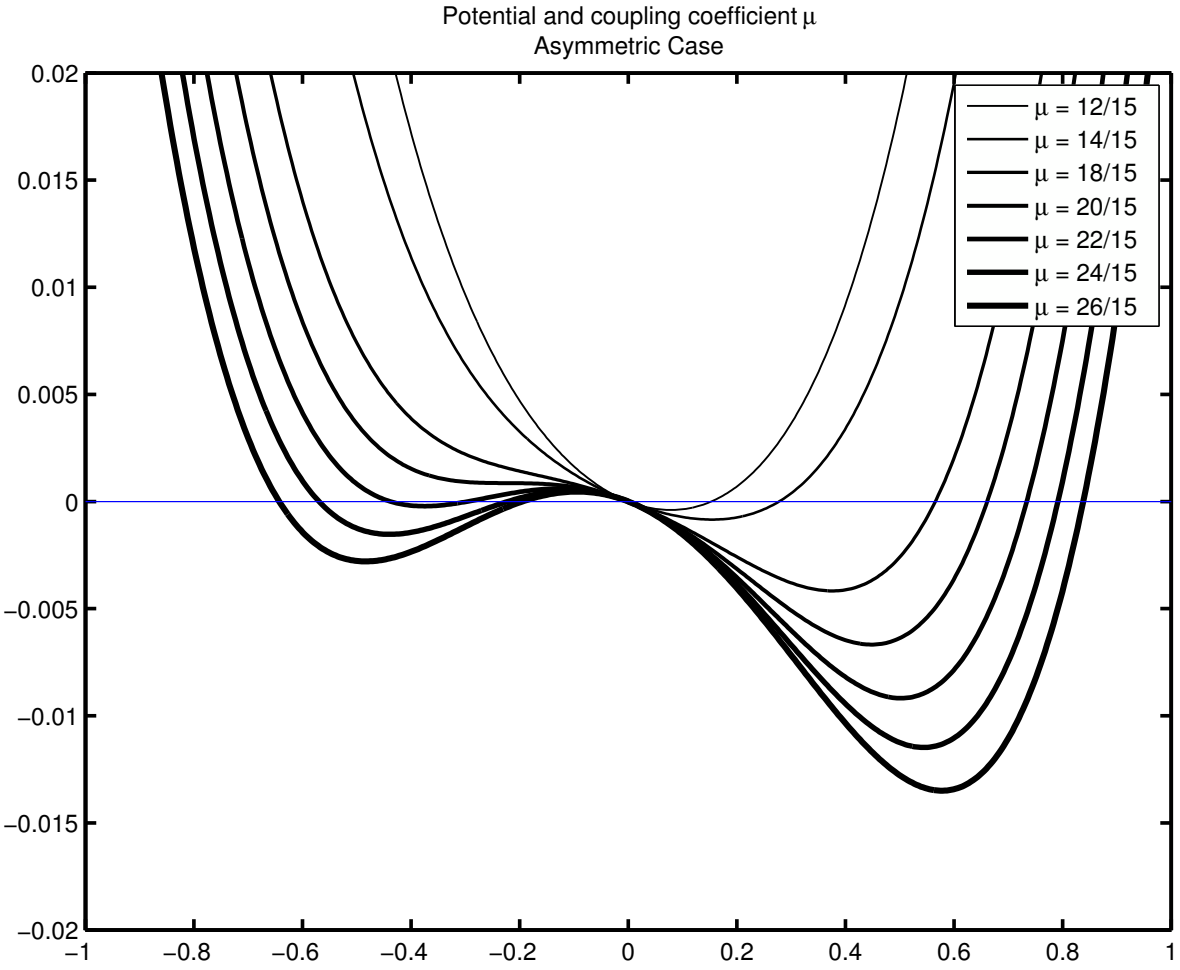

Figure 3.15: The potential for the one-dimensional model including the effect of the MJO. The presence of the MJO breaks the symmetry and makes the potential well for the warm stable case deeper. (The variable z is proportional to the negative of the temperature anomalies).Increasing the coupling intensifies the asymmetry and the separation between the states, making more difficult to overcome the central barrier.

3.5.1 Time correlations

Correlations can be easily obtained from the joint probability in the stationary state. The autocorrelation length, for instance, can be written as:

$$\langle x(\tau)x(0)\rangle = \int\int xx' e^{(U(x)+U(x'))/2Q} \sum_n \psi_n(x)\psi_n(x') e^{-\lambda_n \tau} dx dx' \int\int xx' \psi_0\psi_0 \sum_n \psi_n(x)\psi_n(x') e^{-\lambda_n \tau} dx dx' \tag{3.41}$$

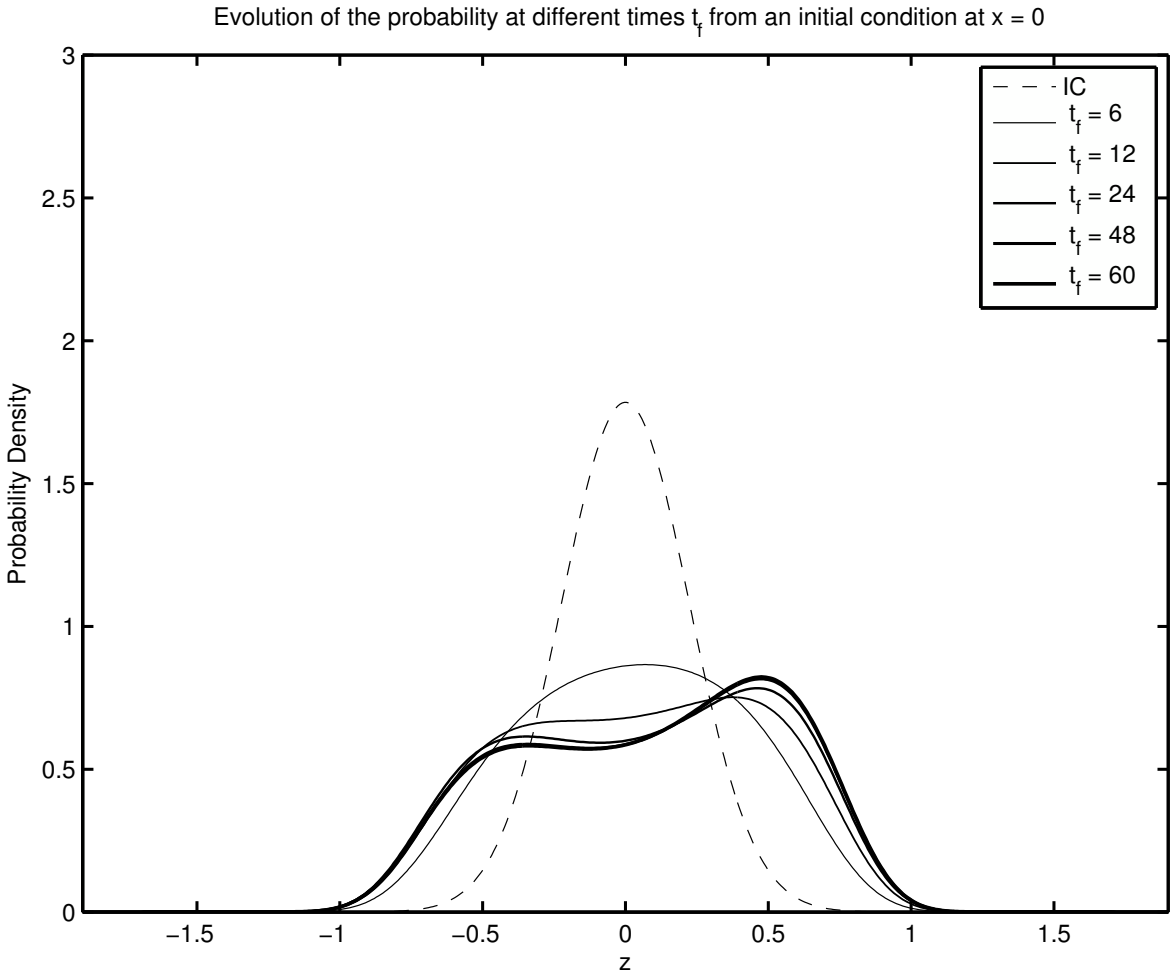

Figure 3.16: As in Fig.3.14, for the asymmetric potential.

This relation reduces to the covariance for $\tau = 0$, whereas the value at different τ's depend on the contribution of each eigenfunction. For very large lags $\tau \to \infty$ it is interesting to see that we can recover easily the Onsager regression hypothesis so that

$$\lim_{\tau\to\infty} \langle x(\tau)x(0)\rangle = \int\int xx'\psi_0(x)\psi_0(x')\psi_0(x)\psi_0(x')dxdx' = \langle x\rangle^2 \tag{3.42}$$

The autocorrelation in general tends to be shorter for increasing noise and increasing asymmetry. The asymmetric potential yield shorter autocorrelations than the symmetric potential for the same value of the coupling and asymmetry parameter γ. The best results are obtained for relatively large values of gamma, in this case 0.06 was used.

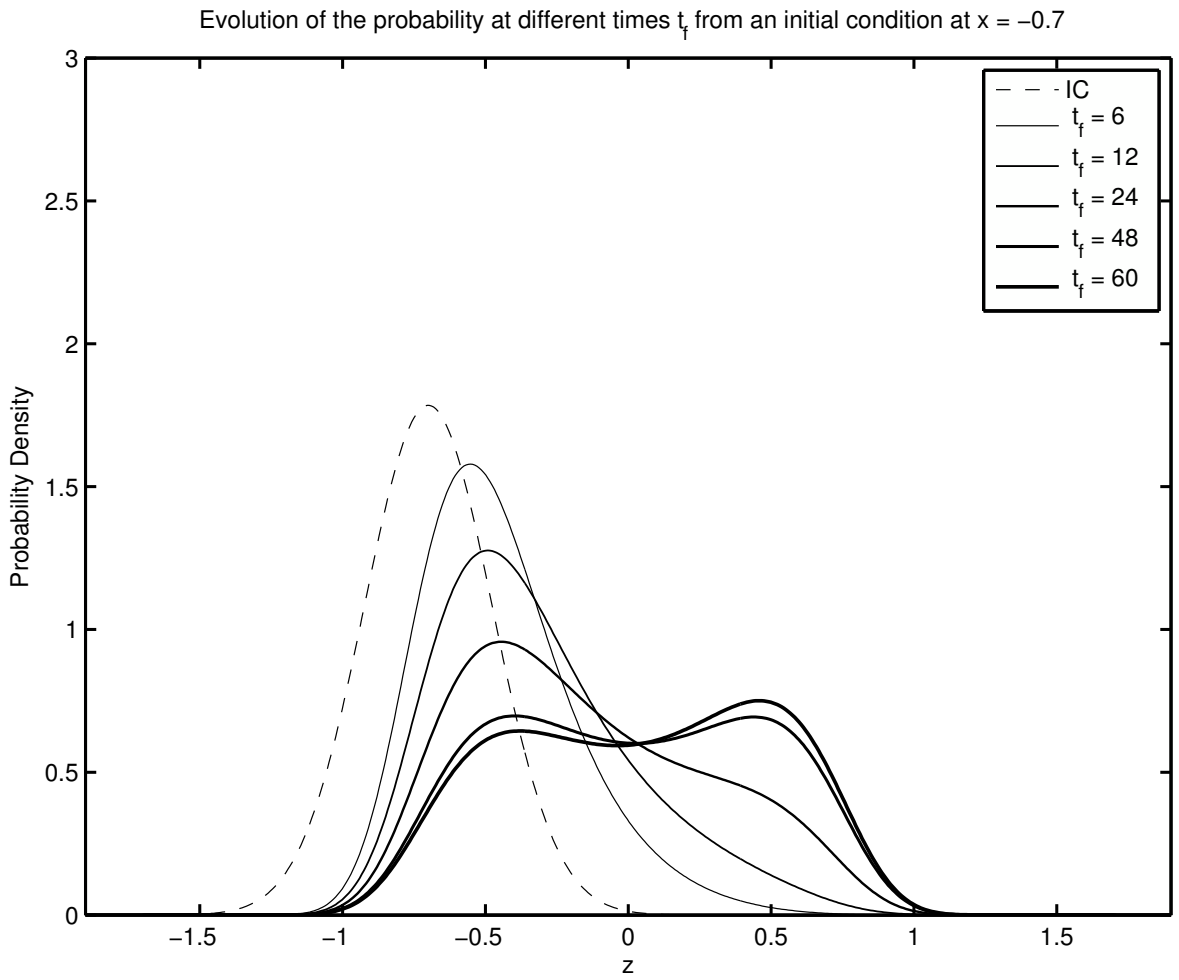

Figure 3.17: As in Fig.3.13, but for the asymmetric potential.

Fig.3.18 shows the autocorrelation for the symmetric and asymmetric potential with $Q = 0.1$ and $\mu = 27/15$. The asymmetric model has some correspondence with the observations for lags up to 10 months, but the symmetric model decays too slowly. The simple asymmetric model captures the main behaviour, but it does not fall quickly enough and it does not cross the zero line.

The behaviour of the autocorrelation is determined by the eigenvalue structure. Fig.3.19 shows the structure of the first eigenvalue in the symmetric and in the asymmetric case corresponding to the autocorrelation in Fig.3.18. The physical interpretation of these eigenvalues in the quantum mechanic case is that they represent the energy levels of the states, in this case they can be interpreted as the decay time scale

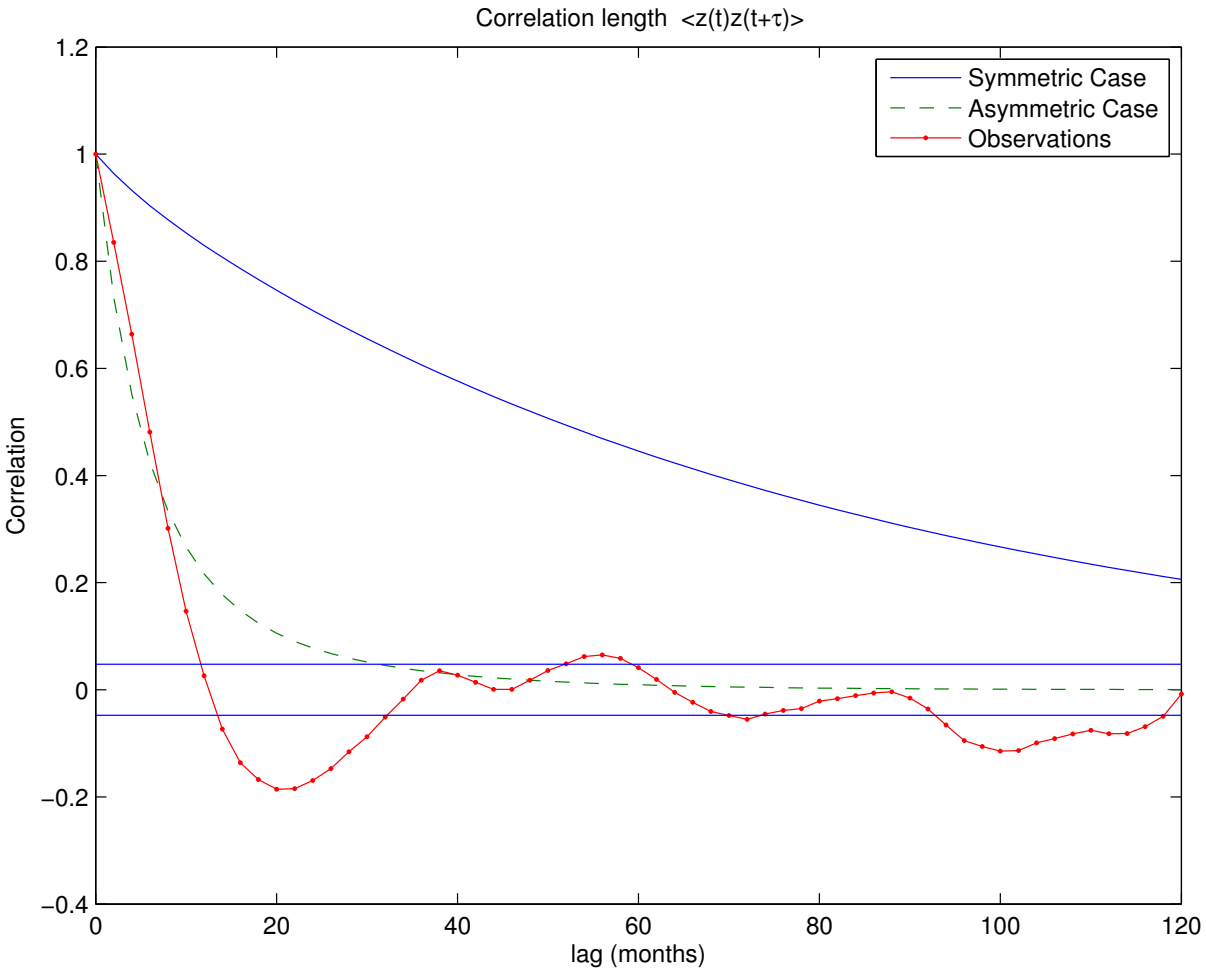

Figure 3.18: Autocorrelation function for the two models. The asymmetric model has shorter correlation length for the same value of the coupling constant μ indicating that the asymmetry is also introducing a faster decorrelation that brings the system to a realistic value of 10-12 months. Horizontal lines indicates the 95% confidence level for the observed autocorrelations.

for each eigenfunction that contributes to the probability distribution. The symmetric case on the left in Fig.3.19, tends to have larger eigenvalues and so the second one has also a very long decay scale of about 38 months inverse. In general the decay scales in the asymmetric case are shorter and so the result is that the autocorrelation as a function of the lag (Fig.3.18) is showing a faster drop, of the order of 10 months for the asymmetric case.

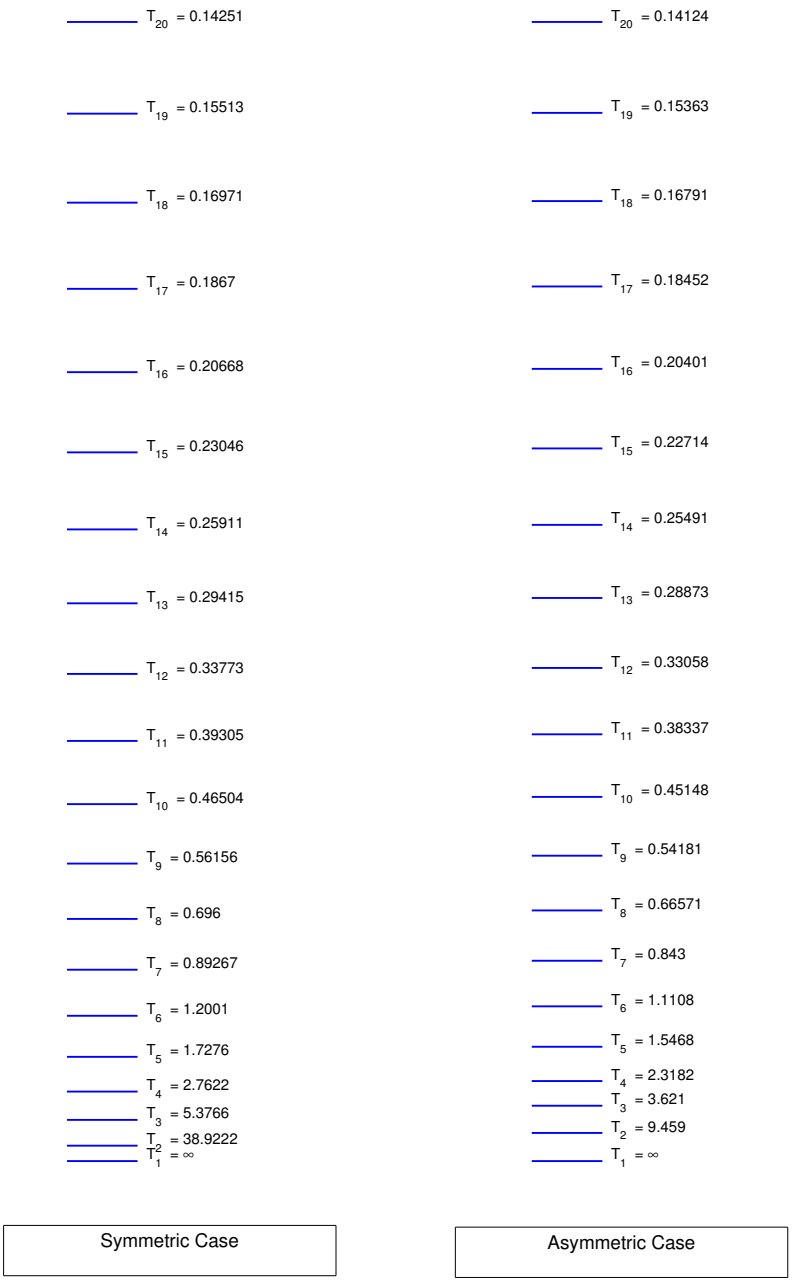

Figure 3.19: The eigenvalues structure for the symmetric model (left) and the asymmetric model (right). It is possible to see how breaking the symmetry has increased the separation between the eigenvalues.

3.5.2 Transition from warm and cold cases

The probability of transition from one probability distribution to another can be obtained from the density probability distribution (Eq.3.18 or 3.38) inserting an initial distribution. In the simplest case we can assume for the initial distribution a delta function in a particular value $W_{IC} = \delta(x' - x_0)$, so that the distribution at time t is

given by

$$W(x,t) = \int P(x,t|x',0)\delta(x'-x_0)dx' = P(x,t|x_0,0) \tag{3.43}$$

It is of particular interest to evaluate the probability to evolve starting from one potential well (a warm El Niño state) to the other well (a cold La Niña state).

In the symmetric case we expect that these two probabilities be the same because of the symmetry, but the asymmetric case is more interesting. The probability distribu-

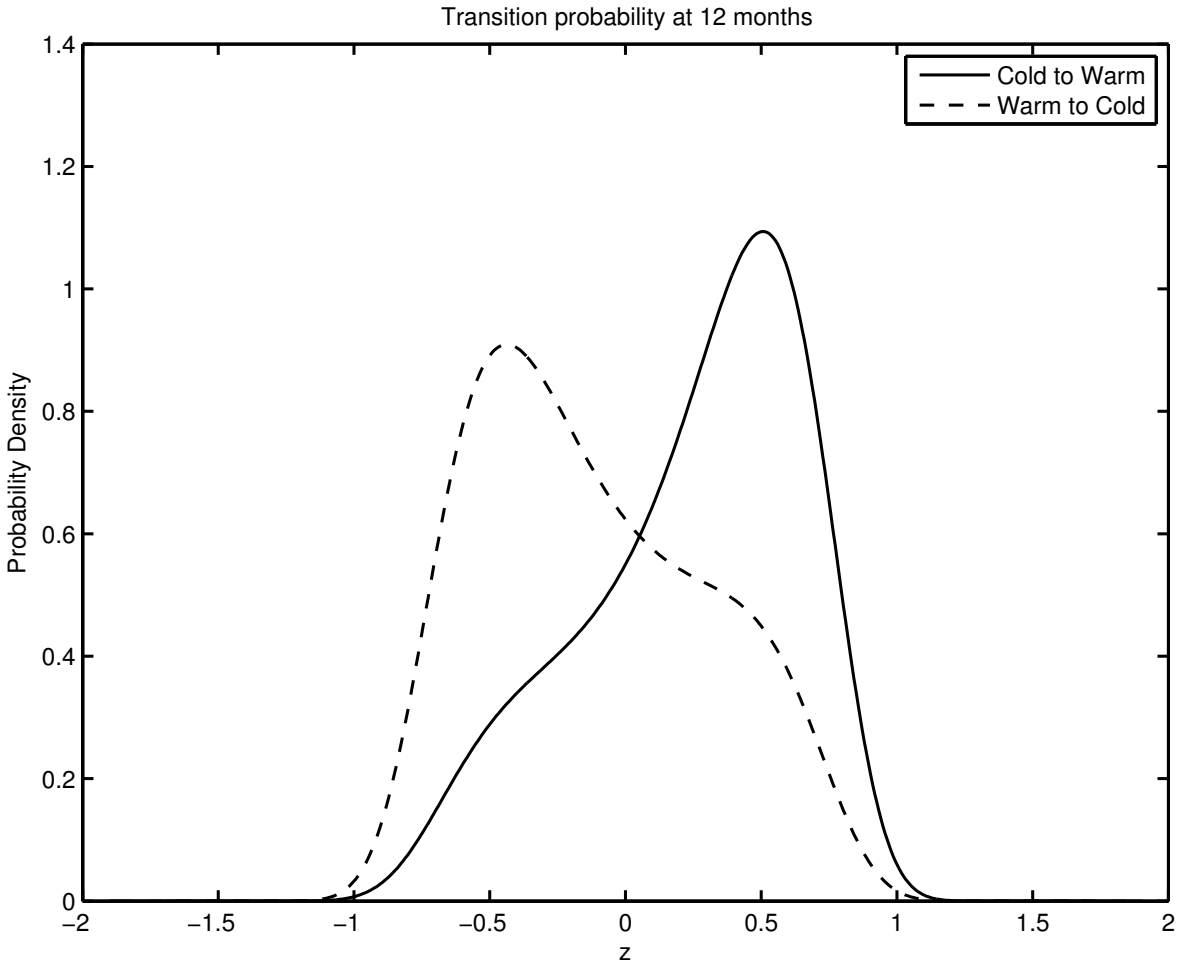

Figure 3.20: The probability distribution for a transition from a sharp, δ-like distribution at $t = 0$ in the cold well (solid) to $t = 12$ months, compared with the same transition from the warm well to the cold well (dashed). The final probability density of the cold to warm transition is smaller than the probability of a warm to cold transition, indicating that El Niño is more probable to be followed by a La Niña than the other way around. The peaks indicate the position of the cold and warm well respectively.

tion for a transition from a sharp, δ-like distribution at $t = 0$ in the cold well located around $z = 0.5$ (solid line in Fig.3.20) to a later time (in this case 12 months later), is showing a secondary peak in the warm well (located around $z = -0.5$), indicating tunneling across the potential barrier induced by the stochastic noise. This is to be expected as we have seen in the previous sections, however the opposite transition, from the warm well to the cold well (dashed line) is also showing a secondary peak, but the probability density is smaller, indicating that warm states are more probable to be followed by cold states than the opposite. This feature tend to be stronger as the asymmetry increases (growing values of μ) or the noise becomes larger. Observations show a similar feature if the probability of the two transitions is estimated from the data (Choi and Vecchi, 2012).

3.6 Conclusions

The probability distribution of the NINO3.4 index, considered as an indicator of ENSO dynamics, can be reproduced by a simple nonlinear system stochastically forced by gaussian noise. A probability distribution with many properties similar to the observed NINO3.4 can be obtained also in a regime that does not support self-sustained oscillations, characterized by large values of the coupling constant between stress and surface temperature. This regime has usually been neglected in the past as a regime where ENSO dynamics could not be deployed because of the absence of oscillations, but we show that indeed this maybe the case if stochastic forcing is included. The theoretical probability distribution allows the calculation of time correlation and other quantities, showing that the asymmetry is necessary to achieve the time scales that are typical of ENSO. The skewness of the distribution is increasing with the coupling parameter and realistic values can be obtained.

It was not the intention of this paper to advocate a bimodal probability distribution for ENSO, in fact the distribution is probably unimodal. We propose instead here a representation of ENSO as transitions between states, even as low as only two, that can be a viable framework to study it. Further work is required to clarify what will be the total number of states that will be needed for the final theory.

The Madden-Julian oscillation has a systematic effect on the eastern Pacific SST and

Table 3.1: Skewness parameter for the asymmetric distribution and various values of the coupling parameter and for $Q = 0.15$ and $\gamma = 0.01$. The skewness increases for larger couplings and it becomes smaller for increasing noise. The skewness for the estimated probability distribution for the observation shown in Fig.3.1 is included at the bottom.

μ	$Skewness$
17/15	0.3692
19/15	0.3803
21/15	0.3898
23/15	0.3981
25/15	0.4055
27/15	0.4122
29/15	0.4185
Obs	0.3633

on the depth of the thermocline in the Western pacific that can be represented in this model in the simplest way with a constant forcing. The presence of the forcing breaks the symmetry, producing a more realistic asymmetric probability distribution between cold and warm states that also explains the gap in the probability of the warm to cold and cold to warm transition. The theoretical autocorrelation is also impacted by the asymmetries and it tends to be closer to the observations. In this hypothesis, the rectified seasonal effect of the MJO activity has a systematic impact on the ENSO dynamics producing the asymmetries observed in the probability distribution.

The theory proposed here unifies in a simple logical framework the hypothesis that ENSO is a chaotic nonlinear system or a linear, but stochastically forced case, in fact both these cases can be obtained as limiting cases of the system proposed here. Weak noise, and/or weak coupling will result in a self-sustained oscillation, whereas weak nonlinearities (though we did not discuss this case here) will recover the linear stochastic system. This study shows that the dynamics of ENSO is possibly far richer than previously thought and different regimes can be active at different times as the coupling constant and the magnitude of the noise varies. We also think that this approach can be extended in a number of ways, considering higher dimensional system, multiplicative or coloured noise and more realistic approaches, but this will be the subject of our next papers.

CHAPTER 4

EFFECTS OF PERIODIC GROWTH RATE IN THE SIMPLE ENSO MODEL AT STRONG COUPLING

4.1 Introduction

In the previous chapter a simple system is proposed that retains the main characteristics of El Niño-La Niña variations, such as the skewness and the autocorrelation, and it is shown how solutions for the probability distribution can be obtained using a Fokker-Planck equation.

Several ENSO's studies consider the seasonal cycle into their deterministic models. Munich (Munnich et al., 1990) studied ENSO as it was described by an iterative map, derived from a more complex model, which combines the linear ocean dynamic in the β-plane approximation with the Bjerknes hypothesis. In this model they also considered the case of a periodic correction into the coupling factor, to take crude account of the mean annual cycle in the SST and of the wind speed. Another interesting explanation of the importance of adding a seasonal cycle in the model, was given Tziperman et al. (1994a). They used a model with delayed equation including an idealized seasonal forcing to evaluate whether ENSO might be a low-order chaotic process driven by the seasonal cycle. The added phenomenological cycle was able to introduce inter-

esting features at strong coupling, that means strong interaction between ocean and atmosphere with consequent strong non-linearity. In fact, in this case the system became mode-locked. The frequency of the non-linear oscillator changes slightly to a simple rational multiple of the driven annual forcing. However such a model with time delay and seasonal cycle could not reproduce the changes in regimes typical of ENSO events. Another forcing, a stochastic one, must be taken into account together with the seasonal cycle, (Stone et al., 1998). Galanti and Tziperman (2000) investigated the phase locking of ENSO to the seasonal cycle in three different dynamical regimes.

The Delayed Action Oscillator (DAO) was modified to include the annual cycle and stochastic forcing, as external influences which allowed to better model ENSO dynamics. Since El Niño events typically appear in late December - early January, the annual cycle plays an important role in the onset of El Niño (Boutle et al., 2007). Recently a stochastic Recharge Oscillator (RO) has been used to explain the role of the annual cycle in ENSO growth rate in the formation of the spring predictability barrier. The RO used is linear and the growth rate considered is almost always negative (Levine and McPhaden, 2015).

I have completed the study started in the previous section making some considerations about the effect of the annual cycle on our simple model. The periodic growth rate used is always positive, in order to implement the Bjerknes positive feedback hypothesis described in chapter 1, but now is modified to be be periodic. If non-linearity and strong coupling are used, this hypothesis can be conserved because the system is damped also without considering a negative growth rate. I have shown that a periodic growth rate produces a periodic, and not static, PDF for the ENSO system, and also in this case with the positive feedback, it is able to explain the Spring Predictability Barrier (SPB) and the spread of the PDF in a particular month of the year.

4.2 Effects of periodic Growth Rate on the Potential

I have considered as starting point the RO with the parameter estimation used in the previous chapter (in A.2 you can find a more detailed explanation of the parameters appearing in the RO), using the cubic non-linear term that for strong coupling is able to damp the system, but I have added a periodic term to the growth rate $R = (\gamma\mu b_0 - c)$ to

take into account the annual cycle. The new periodic term, called $\lambda(t)$, is the combined effect of the periodic coupling and the collective damping term c. The total growth rate can be written as

$$R \to (\gamma \mu b_0 - c) + \lambda(t), \tag{4.1}$$

where

$$\lambda(t) = \lambda_0 + \lambda_1 \cos(\omega t + \omega), \tag{4.2}$$

with $\omega = \frac{2\pi}{6}$, since I have used the scaling of Jin (Jin, 1997a). The shape of $\lambda(t)$ has chosen following the suggestion of Stein, (Stein et al., 2010). They estimated that the growth rate should decrease in the first part of the year and then becomes bigger during autumn. They used a linear stochastic model and the growth rate is almost always negative, while I have wanted to conserve the positive Bjerknes feedback in the model, so $\lambda(t)$ acts to decrease the estimation of the growth rate in the first part of the year but is always positive the total growth rate. The initial decreasing could be justified thinking to the impairment of the wind stress, that should decrease in that period. This could be seen as an impairment of the coupling between ocean and atmosphere and then the growth rate should be smaller. In Fig. 4.1, it is shown the total and the mean behavior of the growth rate. From here the parameter used are $\lambda_0 = -0.5$ and $\lambda_1 = 1.4$, $\mu = \frac{24}{15}$, $\gamma_h = \gamma_T = 0.02$ and $Q = 0.015$.

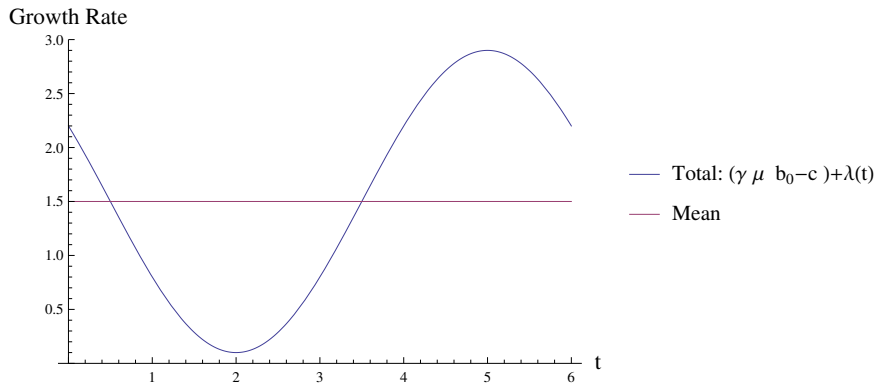

Figure 4.1: Growth Rate periodic variations and mean. With this parameter the growth rate is small during the first part of the year and becomes bigger during autumn.

If now the transformation performed in the previous section is used, a simple model described by a unique equation is found

$$\dot{z} = -z^3 \frac{20\mu}{16 + 25\mu^2} + z\frac{(16\lambda_1 \cos(t\omega) + 16\lambda_0 + 15\mu - 16)}{25\mu^2 + 16} + \frac{25\mu^2\gamma_h - 20\mu\gamma_T}{25\mu^2 + 16}. \tag{4.3}$$

Now in the growth rate appears the periodic annual cycle. The effect of this periodic term is that of modifing the potential previously found, making it time dependent, Eq. (4.4)

$$U(z,t) = \frac{5\mu z^4}{25\mu^2+16} - \frac{z^2\left(8\lambda_1\cos(t\omega) + 8\lambda_0 + \frac{15\mu}{2} - 8\right)}{25\mu^2+16} - \frac{z\left(25\gamma_h\mu^2 - 20\gamma_T\mu\right)}{25\mu^2+16}. \quad (4.4)$$

In Fig. 4.2, it is shown the behavior of the periodic potential, derived from the periodic drift of Eq. (4.3). Remember that the time scale used here is $[t] = 2$ months. Now

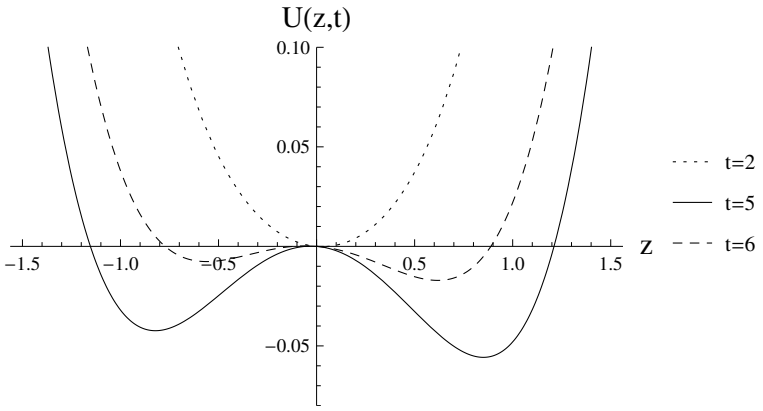

Figure 4.2: Periodic drift potential Eq. (4.4).

the potential modifies its shape during the year. During autumn it becomes more and more asymmetric and gradually becomes parabolic in spring. This behavior influences the PDF periodically and it is able to modify the persistence of the initial condition. The systematic MJO effect, taken into account with the two constants γ_h andγ_T, modifies the symmetry of the potential.

Numerically solving the FP equation associated to the stochastic Eq. (4.3), the periodic PDF can be found. In Fig. 4.3, it is shown a contour of the evolution of the PDF using as initial condition a Gaussian distribution centered in $z = 0$. When $z \approx \pm 1.5$ the potential act as a wall for the system and then we set as boundaries for the FP equation that the PDF must go continuously to zero in those points. After approximately one year the system loses information about the initial PDF distribution, and the long-term periodic behavior of the PDF is reached. In Fig. 4.4, temporal slices of the PDF evolution are shown. During December periods, time slices $t = 24$ and $t = 30$, the system has more chances to make rise strong events than in August periods $t = 28$ and $t = 34$. This respects the observed behavior, Fig. 5.1a of the next chapter.

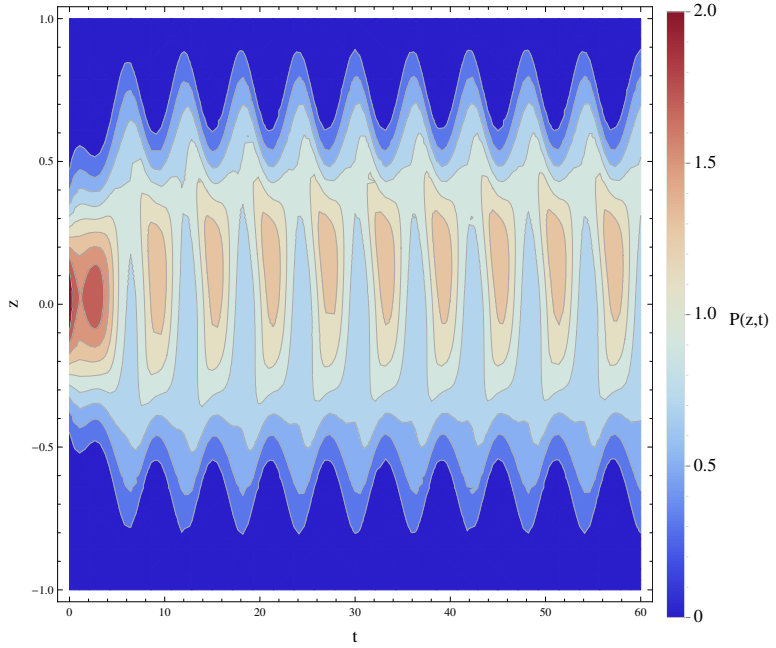

Figure 4.3: Contour of the evolution of the PDF associated to Eq. (4.3).

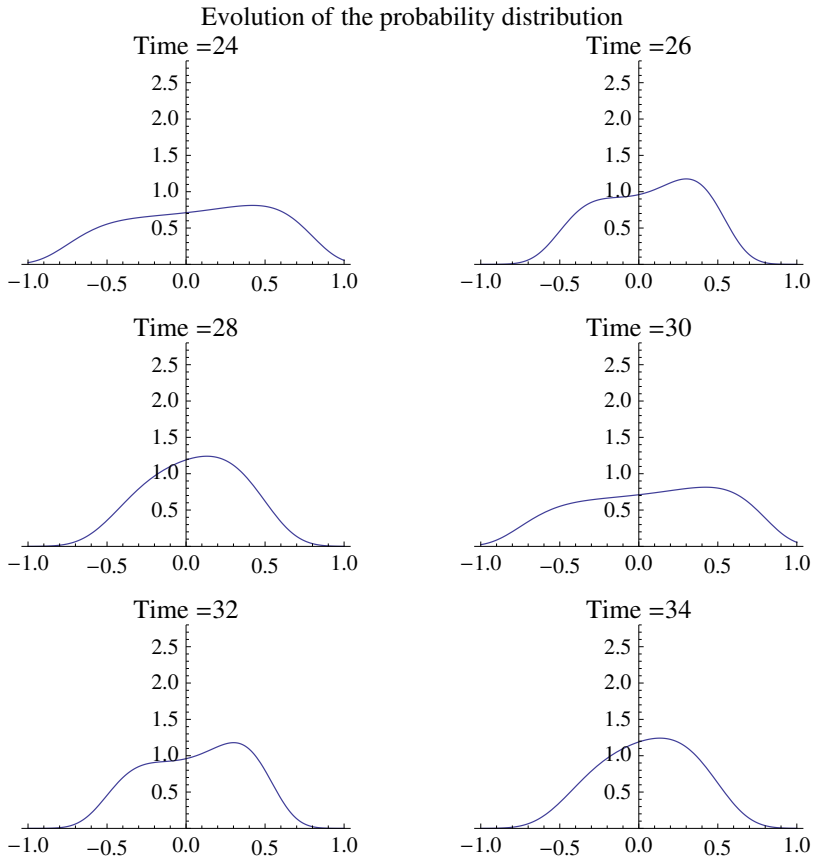

Figure 4.4: Temporal slices of the PDF evolution.

As mentioned above, and suggested by Levine and McPhaden (Levine and McPhaden,

2015), the effect of the periodic growth rate is reflected in a difference persistence in the initial condition during the year. This means that the periodic growth rate produces a predictability barrier. A straightforward explanation of this effect can be done looking at the potential. When the growth rate decreases, the drift potential becomes parabolic and the system is more locked, it can not easily jump in different configurations, and the system is more persistent. On the contrary, when the potential is asymmetric and away from the parabolic configuration, the system, with the aid of noise, can jump between two potential wells that correspond to events of strong anomalies. To examine this effect, the ensemble Normalized Temperature Persistence (NTP) has been used for every month m, defined here by the following quantity

$$NTP_m(\tau) = \frac{1}{Ny-1} \sum_{i=1}^{Ny-1} \frac{T^i(m+\tau) - T^i(m)}{T^i(m)}, \tag{4.5}$$

where Ny is the total number of years of the series, and $T^i(m)$ ($z^i(m)$ if the model is considered) is the temperature during the year i at month m. In Fig. 4.5, it is shown the behavior of the quantity defined above, computed both for the NINO3.4 time series and for a 4000 years time series generated with the model. Both the pictures show evidence of the so called Spring Predictability Barrier. A periodic growth rate can generate the predictability barrier.

For completeness I have to remark a few problems related with this simple model. With the value of the parameter used here, the standard deviation of the time series generated with the simple model is $\sigma_M \approx 1.4\,^\circ$C (once z is converted in dimensional temperature), while the one computed from the observations is $\sigma_O \approx 0.8\,^\circ$C. Looking at Fig. 4.5, it can also be noted that the autocorrelation of the observations must decrease faster than the one of the model. Increasing the value of Q, the parameter more difficult to estimate, the right value of the correlation can recovered but σ_M is amplified and the PDF results to be less asymmetric (not shown here). Decreasing the Q value, the asymmetry increases and decreases σ_M, but the model is strongly autocorrelated.

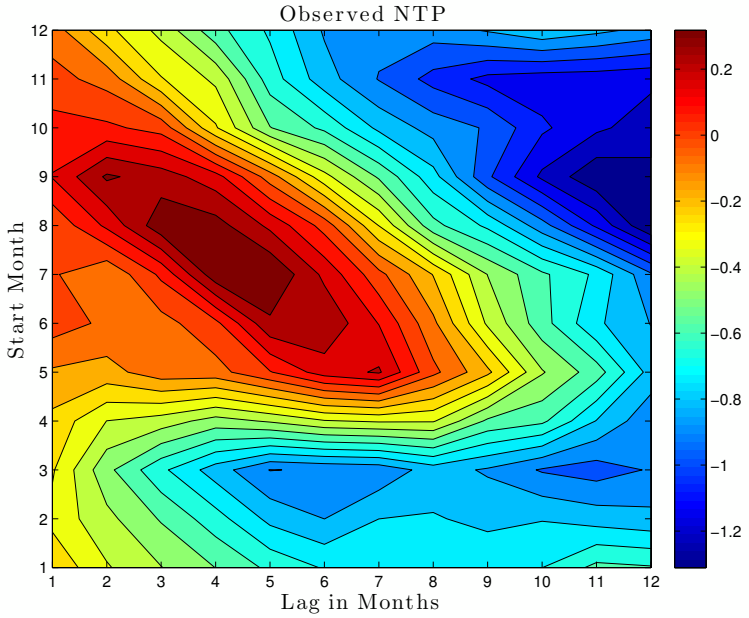

(a) *Ensemble NTP computed using the NINO3.4 time series.*

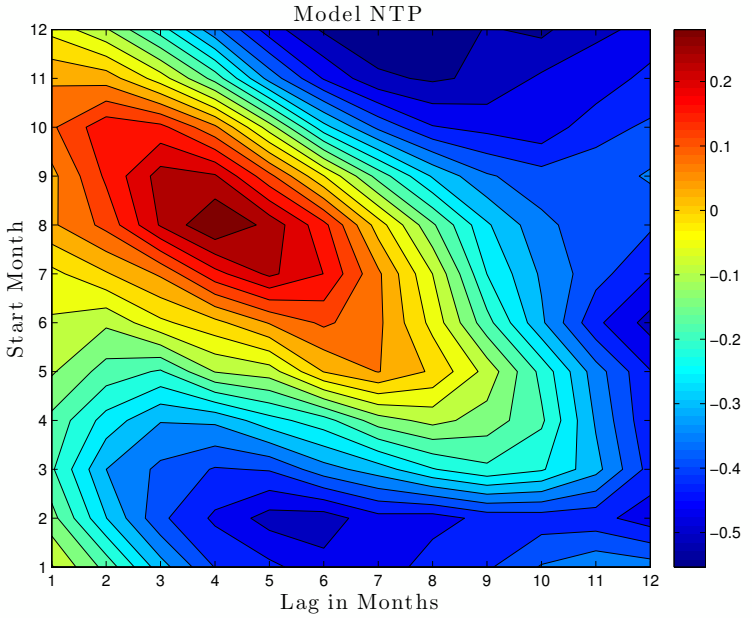

(b) *Ensemble NTP computed using the a* 4000 *years time series generated with the simple model.*

Figure 4.5: Comparison of the Ensemble NTP computed both for the observations and for the model. Both the pictures show the so called Spring Predictability Barrier.

4.3 Summary

In the last two chapter a new way to consider ENSO is suggested; it can be seen as a system that can jump between two states, one positive and one negative, thanks

to the stochastic forcing. These two states are represented by a potential generated by the non-linearity that damps the system. Since the noise is an important ingredient in studying ENSO, we have studied the system by means the FP equation associated with it. In this framework the natural way of thinking is the one that refers to the potential that arises from the drift term of this FP equation.

The model studied has been derived using a rotation in the space of variables of the Recharge Oscillator. This starting model is based on the positive Bjerknes feedback and does not consider explicitly retarded waves, but their cumulative effect into the parameters definitions. To the rotated model the stochastic forcing has been added to sustain the oscillation otherwise damped. This damping is granted thanks to the strong coupling between atmosphere and ocean used and the non-linear term. into the equation.

We have tried, using this rotated model described by just one equation, to suggest a possible mechanism that could explain the asymmetry in the PDF typical of ENSO. In particular, taking into account the MJO effect into the equations we have been able to set the different depth of the double well potential that describes the system, generating in this way a PDF that is asymmetric.

Using this model, I have also tried to exploit a periodic growth rate as cause of the predictability barrier, another important feature of ENSO. It is important to remark that before the rotation in the variable space, I have modified the growth rate maintaining it positive to respect the positive Bjerknes hypothesis. The predictability barrier could be explained by means the potential well. During autumn it becomes more and more asymmetric and gradually becomes parabolic in spring. This behavior influences the PDF periodically and it is able to modify the persistence of the initial condition.

It is impossible to obtain the exactly values of all the observables that characterize ENSO using more sophisticated Coupled General Circulation Model (CGCM), so we have no hope to explain exactly ENSO using such a simple model. A perfect reproduction of ENSO is not the aim of this work but rather trying to highlight all the mechanisms that together with the Bjerknes positive feedback are able to characterize ENSO, in particular the asymmetry of the PDF and the SPB.

CHAPTER 5

ENSO'S TRANSITION PROBABILITY MATRICES

5.1 Introduction

The long-term predictability and the study of the variability generated by the interaction between atmosphere and ocean, are one of the big challenges of our time. Being able to deeply understand and to provide predictions of phenomena such as El-Niño Southern Oscillation (ENSO), which is able to change the normal weather variability on global scales causing damage to agriculture and therefore to the socio-economic system of entire countries, could mean limiting the damages generated by these phenomena.

Lorenz started to show the difficulty in making weather forecast, explaining the chaotic nature of the dynamic that governs the atmosphere and the ocean (Lorenz, 1963, 1984, 1987). Because of small, but inevitable, errors committed in defining the initial state, the solution of the simulation quickly moves away from the real solution. He also estimated that the small errors generally tend to amplify as time goes by: he estimated that they tend to double in 2.5 days (Lorenz, 1969).

Despite these problems, Shukla (1981), extended the classical concept of predictability to the predictability of time averages. He showed that the predictability limit for

the synoptic-scale wave is only about two weeks, while the predictability limit of the low-frequency planetary waves could be longer than one month; these observations lay the physical foundations to make dynamical prediction of monthly means.

Two years later, Miyakoda et al. (1983) highlighted that some large-scale quasi-stationary anomalous circulation features could have been successfully predicted using initial conditions, without considering any boundary conditions; but, later than one month, the focus of the problem should be more on boundary conditions than the atmospheric initial conditions (Shukla, 1985).

Assuming that the Sea Surface Temperature (SST), provides the major lower boundary for the atmosphere Stern and Miyakoda (1995) showed the feasibility of seasonal forecast using multiple General Circulation Model (GCM) simulations.

Now a new field called “Decadal Prediction” is using initialize climate model to produce future climate projections (Meehl et al., 2009).

Even tough there have been lots of advances in the predictability, there are still matters that are not completely understood, in particular about the seasonal predictability affected by the Spring Predictability Barrier (SPB). This phenomenon is one of the most important causes of prediction uncertainties in ENSO forecasting. It often experienced by most ENSO-forecasting models, and it is characterized by an apparent drop in prediction accuracy during April and May (Webster and Yang, 1992; Webster, 1995). After the spring (or the autumn in the Southern Hemisphere), the ability of the models to predict becomes increasingly better. SPB , “shakes" the system that looses part of the information about its state.

It must also be considered that all the models inherit uncertainty associated with a finite resolution and with the approximation in the physical equations used. These elements could introduce some fictitious effects that distort the results obtained with the simulations.

I have wanted to present how to use the probability transition matrices associated with a particular climatic phenomenon for an its description and characterization. In particular I have focused on ENSO, since the investigation of the previous chapter prompted the idea that ENSO could be a system described by a sequence of states, rather than a simple oscillation (even if this framework can be extendable to all the

other climate phenomena). The transition considered between different seasons are one year long or less. From these matrices the SPB effect can be recognized and a sort of index of predictability using the entropy associated to these matrices can be written.

Nicolis (1990) developed a systematic method for mapping deterministic chaos in general, and atmospheric and climate dynamics in particular, into a Markovian process. He casted a multivariate system continuously evolving in time in a discrete iterative form, monitoring successive extrema of some of the variables, as done also by Fraedrich (1988), or reducing the dimensionality of the system using Poincaré map. From the map obtained, using appropriate partition of the possible state he mapped the deterministic chaotic system into a stochastic one, described as a Markov process.

However, some interesting systems, such as ENSO, seem to be described by damped oscillations sustained by noise. The stochastic forcing in this phenomenon is really important. Instead of describing it considering an iterative map derived by monitoring its extrema, I have divided Sea Surface Temperature Anomaly (SSTA), in four states; then, I have computed the transition probability matrices for these states for different transitions periods. These matrices not necessarily describe a Markovian process, but if this is the case, more information, as the mean sojourn time and variance, can be easily extracted. As it will be explained in the next section, using only two states, the extreme events could bring an over-estimation of this mean sojourn time.

This statistical approach is applied both to the NINO3.4 index (the mean SST in the region $5°\text{N} - 5°\text{S}$ and $170°\text{W} - 120°\text{W}$ with the seasonal cycle removed) computed from the observations, and to the same index computed from a long run simulation of a General Circulation Model (GCM). These matrices can be used to compare models and observations. From the comparison, it is possible to see in detail the statistic related to the dynamic of ENSO, the persistence of a state or its capabilities to transit in another one. The stationary distribution for every season can also be extracted, but here there is more information. Comparing the matrices obtained from the model and observations, it is possible to have a more detailed picture of the wrong kind of transition that could happen in the model for a particular transition time.

These matrices are also computed for a time series obtained disturbing a simple oscillation with noise. This is done to highlight the signature which could be left by that kind of signal in these matrices.

A statistic for small population is applied to the entries of the observation and model matrices to compute the confidential interval of each transition probabilities.

5.2 Methods

One of the possible ways of studying the ENSO phenomenon, by means NINO3.4 index, passes through the use of the transition probabilities matrices. I have assumed that the SSTA can fall just in four states defined in Tab. 5.1b. The A^- state represents a strong negative anomaly that could be considered as a La Niña event, accordingly to the definition of `http://www.cpc.ncep.noaa.gov`, while A^+ is a strong warm event that could be considered as an occurrence of El Niño. The intermediate states N^- and N^+ , respectively negative and positive, are the so called neutral states, characterised by too small anomalies to consider the Pacific Ocean in a state of La Niña or El Niño. The SSTA jumps in each of these states with the seasons changing Tab. 5.1a. From NINO3.4 index, it can be found a new series in which the time unit leads in the next season and where the SSTA can assume four values. I have started with a monthly data time series of 159 years, from January 1856 to December 2014. The period 1856-1949 is a reconstruction (Kaplan et al., 1998) while the period 1950-up to now is taken by the Climate Prediction Center of the NOAA, `http://www.cpc.noaa.gov/data/indices/`.

Convention	Months
s_1	DJF
s_2	MAM
s_3	JJA
s_4	SON

(a) .

States $\mathbb{T}$	Range $SSTA$ $[C]$
A^-	$(\infty \quad -0.5)$
N^-	$[-0.5 \quad 0]$
N^+	$[0 \quad 0.5]$
A^+	$(0.5 \quad +\infty]$

(b) .

Table 5.1: Conventions for the name used to indicate different seasons and division of the continuos interval of SSTA variation in four different discrete states.

I have denoted with $\mathbb{W}^{nk}$ the matrix that contains the transition probabilities between states considering the starting season s_n and the ending season s_k. If $n < k$,

both seasons belong to the same year, if $n \geq k$ the convention used here is that s_k belongs to the next year. The elements of this matrix are

$$(\mathbb{W}^{nk})_{ij} = \mathbb{P}(i, s_n | j, s_k), \quad i, j \in \mathbb{T}, \text{ and, } \; n, k \in \{1, 2, 3, 4\}, \tag{5.1}$$

where $\mathbb{T}$ is the space of the possible states, and $\mathbb{P}(i, s_n|j, s_k)$ is the conditional probability to reach the state j during the season s_k starting from the state i in the season s_n, with the convenience that the time of the transition must not be longer than one year.

The transition probability matrix is unknown, and the matrix elements have to be empirically found. Since there is a 159 years time series of monthly data, it is possible to assist to 12x159-1 monthly transitions. The best estimate for these transition probabilities is found considering the number of transitions m_{ij}^{nk} made from the state i, during one of the months belonging to the season s_n, to the state j in one of the three months of the season s_k, and the total number of transitions made out of state i during this period $m_i^{nk} = \sum_{j \in \mathbb{T}} m_{ij}^{nk}$. The empirical transition matrix can be used to construct an estimate of the transition probability matrix:

$$(\hat{\mathbb{W}}^{nk})_{ij} = \frac{m_{ij}^{nk}}{m_i^{nk}}, \quad i, j \in \mathbb{T}, \text{ and, } \; n, k \in \{1, 2, 3, 4\} \tag{5.2}$$

this is just estimating a binomial proportion. Finding an error for these matrices is more complicated, since the conditions for a Bernoullian sampling like this

$$m_i^{nk} \, (\hat{\mathbb{W}}^{nk})_{ij} > 10 \; \wedge \; m_i^{nk} \, (1 - (\hat{\mathbb{W}}^{nk})_{ij}) > 10 \tag{5.3}$$

are not satisfied for all the elements of the matrix. The violations of these conditions tell that the low of 3σ, where σ is the estimate of the standard deviation, can not be used. An estimation of the probability from a small population is done, but the universal confidence levels are not well defined. This is because of the strong dependence of the binomial distribution for small population on the number of sampling m_i^{nk} and on the probability $(\hat{\mathbb{W}}^{nk})_{ij}$. This problem can be solved finding directly the solution of the confidence level problem transcribed for a discrete variable (Rotondi et al., 2001). If CL is the confidence level required, the extreme values $(\hat{\mathbb{W}}_1^{nk})_{ij}$, $(\hat{\mathbb{W}}_2^{nk})_{ij}$ of the cor-

respondent confidence interval are determined by:

$$\sum_{m=m_{ij}^{nk}}^{m_i^{nk}} \binom{m_i^{nk}}{m} (\hat{\mathbb{W}}_1^{nk})_{ij}^m \, (1 - (\hat{\mathbb{W}}_1^{nk})_{ij})^{m_i^{nk}-m} = c_1 \tag{5.4}$$

$$\sum_{m=0}^{m_{ij}^{nk}} \binom{m_i^{nk}}{m} (\hat{\mathbb{W}}_2^{nk})_{ij}^m \, (1 - (\hat{\mathbb{W}}_2^{nk})_{ij})^{m_i^{nk}-m} = c_1 \,, \tag{5.5}$$

with $c_1 = c_2 = \frac{1-CL}{2}$. This system can be solved with a simple recursive algorithm of dichotomous search. Fixing the starting values for the extremes of the confidence level $(\hat{\mathbb{W}}_1^{nk})_{ij} = (\hat{\mathbb{W}}_2^{nk})_{ij} = 0.5$, and a step size $s = 0.5$, after each iteration it is added or subtracted half step to the probability values until Eqs. (5.5) are satisfied less than a certain small amount $\epsilon = 10^{-6}$. If the problem for each value of the transitions matrices is solved, it is possible to say that

$$(\hat{\mathbb{W}}^{nk})_{ij} \in \left[(\hat{\mathbb{W}}_1^{nk})_{ij} \quad (\hat{\mathbb{W}}_2^{nk})_{ij} \right] , \tag{5.6}$$

with the required confidence level.

These transition matrices may show some important features about ENSO; for example, using just four states, the spring barrier could be highlighted by the values of the probabilities and how they move through the matrix considering different seasons transitions.

One way to quantify this loss of information is considering the distance between the different transitions matrix and the one that represents the complete lack of information, that it can be seen as the matrix that has the maximum entropy, that is the uniform distribution matrix

$$\mathbb{M}_E = \begin{bmatrix} 0.25 & 0.25 & 0.25 & 0.25 \\ 0.25 & 0.25 & 0.25 & 0.25 \\ 0.25 & 0.25 & 0.25 & 0.25 \\ 0.25 & 0.25 & 0.25 & 0.25 \end{bmatrix} . \tag{5.7}$$

The distance considered here between the two matrices $\mathbb{A}$, $\mathbb{B}$ is the ordinary d_2 distance

$$d_2(\mathbb{A}, \mathbb{B}) = \sqrt{\sum_{i=1}^{4} \sum_{j=1}^{4} (a_{ij} - b_{ij})^2} \, . \tag{5.8}$$

The seasonal transition that suffers more from the SPB effect should have the smallest distance. To estimate the true distance and the error for each matrix, it is necessary to consider an ensemble obtained varying the probabilities contained in the matrix under study according to their confidence interval, in such a way that the sum of each row is equal to one. For all the ensembles, the distance is computed so that one can consider the distance average and standard deviation.

Another more useful way to compute the loss of information for the different transition matrices is using the entropy of the matrices computed as

$$S(\hat{\mathbb{W}}^{nk}) = -\sum_{i,j}(\hat{\mathbb{W}}^{nk})_{i,j}\log_e[(\hat{\mathbb{W}}^{nk})_{i,j}], \quad i,j \in \mathbb{T}\,. \tag{5.9}$$

From these quantities it is easy to build a clear index for the predictability of ENSO as follow:

$$ENSO_{idx} = 1 - \frac{S(\hat{\mathbb{W}}^{nk})}{S(\mathbb{M}_E)}. \tag{5.10}$$

When this index is equal to one, the maximum information is obtained and you are sure about the possible transition that occurs.

A simple test to verify the goodness of these matrices is to recover the long-time Probability Density Function (PDF) for the states in $\mathbb{T}$, computed from the time series of the NINO3.4 index for different seasons. Fig. 5.1a shows the behavior of the PDF of the SSTA for the four seasons of Tab. 5.1a, while Fig. 5.1b shows the PDF computed for the four states considered. One of the most important facts is that the ENSO PDF is more asymmetric during autumn and winter than in spring and summer. This is a consequence of the occurrence in phase of the strong anomaly. If $\mathbf{P}(s_k)$ is the row vector that represents the long-time PDF for the four states in the season s_k,

$$\mathbf{P}(s_k) = E[\mathbf{P}_0(s_n)\mathbb{W}^{nk}]_0\,, \tag{5.11}$$

where $E[\,]_0$ is the mean obtained considering all the possible initial distributions $\mathbf{P}_0(s_n)$ in the season s_n. If the matrices $\hat{\mathbb{W}}$ are a good estimation of the real matrices $\mathbb{W}$, Eq. (5.11) must hold also for these matrices.

Fig. 5.2 is the same as Fig. 5.1b but for the NINO1+2 and NINO4 indices. These data series are also used to describe ENSO. The domains of definition are $10°\mathrm{N}-$

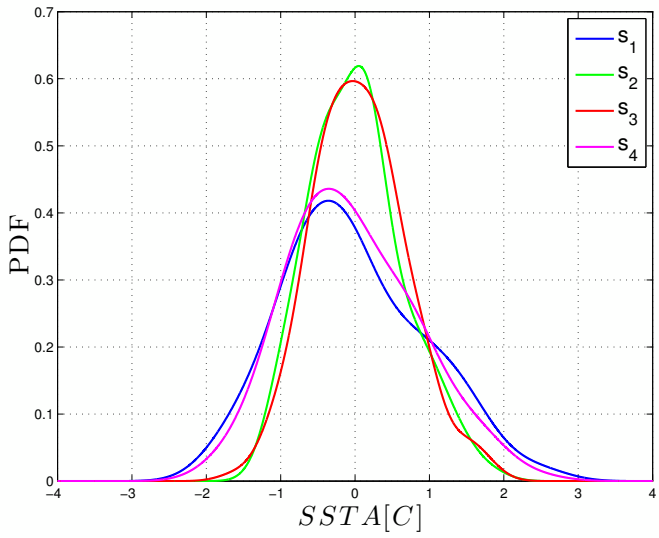

(a) *Long-time seasonal PDF computed from the NINO3.4 index.*

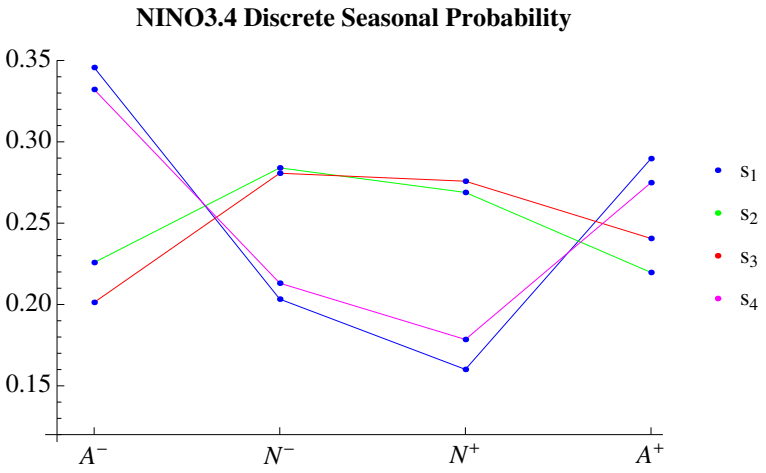

(b) *Long-time seasonal discrete probability for the state $\mathbb{T}$ computed from the NINO3.4 index.*

Figure 5.1: Long-time PDF and discrete PDF (for the state $\mathbb{T}$) computed from the NINO3.4 index.

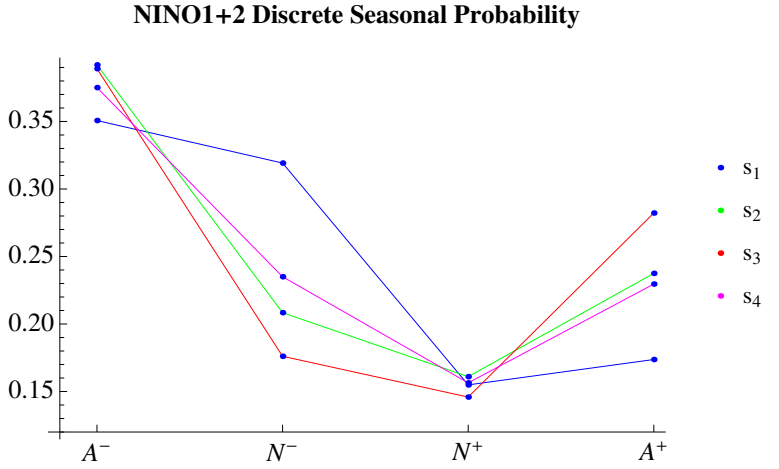

(a) *Long-time seasonal discrete probability for the state* $\mathbb{T}$ *computed from the NINO1+2 index.*

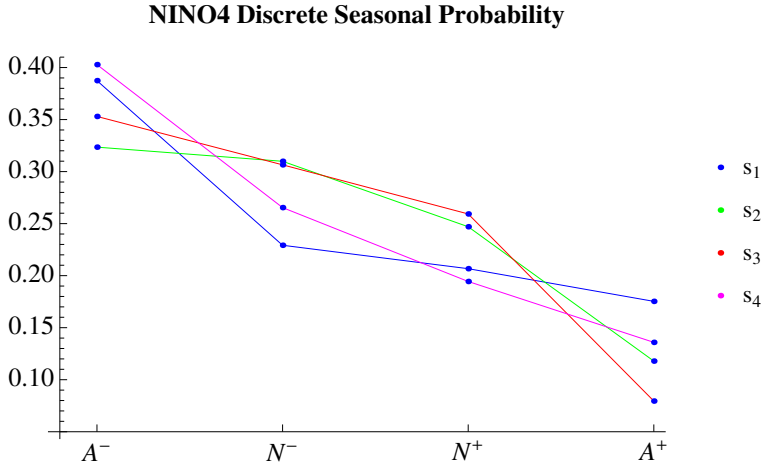

(b) *Long-time seasonal discrete probability for the state* $\mathbb{T}$ *computed from the NINO4 index.*

Figure 5.2: Long-time discrete PDF (for the state $\mathbb{T}$) computed from the NINO1+2 and NINO4 indices. For these ones the changes in the seasonal discrete probability density are not highlighted as in Fig. 5.1b, they seem to be more stationary.

$10°$S, $80°$W $-$ $90°$W and $5°$N $-$ $5°$S, $160°$E $-$ $150°$W respectively. With these domains of definition NINO3.4 results to be more sensitive during time, because is computed in a more central region than the other two indices. In fact, the change in concavity for the discrete PDF in Figs. 5.2a and 5.2b is really reduced, and this pushed me to analyze further, via the transition probability matrices, the NINO3.4 data series. The other two regions (NINO1+2 and NINO4 indices) are too much locked to appreciate jumps between the four states described above.

A particular group of transition matrices is the one for which $n = k$; these are the one-year transitions. Since the ENSO autocorrelation decays exponentially fast,

these kind of matrices could be considered associated to homogeneous discrete-time Markov chains with time step of one year. Homogeneous in the sense that $\hat{\mathbb{W}}$ do not change in time, and they are the same for every step. This consideration allows us to study some temporal characteristics of ENSO without using the spectrum. In particular, it can be computed the mean sojourn time of this discrete-time chain, that is the mean total number of steps that one chain at state i stays there at each visit. If the diagonal elements of these matrices are different from zero, at any time step the system may remain in its current state. At each time step, the probability of leaving any state i is independent from what occurred at previous time step, and is equal to

$$\sum_{i \neq j} (\hat{\mathbb{W}}^{nn})_{ij} = 1 - (\hat{\mathbb{W}}^{nn})_{ii} \,. \tag{5.12}$$

The evolution of the system may be identified with a sequence of Bernoulli trials (Stewart, 2009), with probability to exit from the state i equal to $1 - (\hat{\mathbb{W}^{nn}})_{ii}$. The probability that the sojourn time is equal to l steps is that of having $l-1$ consecutive Bernoulli failures, followed by a single success. This means that the sojourn time at state i for the chain associated with the transition between the seasons n, that I have denoted with T_i^{nn}, is geometrically distributed with parameter $1 - (\hat{\mathbb{W}^{nn}})_{ii}$. From this distribution, the mean and the variance of the sojourn time can be easily computed:

$$E[T_i^{nn}] = \frac{1}{1 - (\hat{\mathbb{W}}^{nn})_{ii}} \,, \tag{5.13}$$

$$Var[T_i^{nn}] = \frac{(\hat{\mathbb{W}}^{nn})_{ii}}{(1 - (\hat{\mathbb{W}}^{nn})_{ii})^2} \,. \tag{5.14}$$

It is also interesting to recall that the geometric distribution has the memoryless property, that means that a sequence of $l-1$ unsuccessful trials does not affect the success of the l^{th} jump. This sojourn time can give indications about the mean time that one state of ENSO can stay there when occurs in a given season. The analysis of the mean sojourn time for ENSO requires just a little attention about the fact that four chains referred to the transitions in different seasons are considered. Since strong events occur more frequently during winter and autumn, the correspondent chains will tend to give a longer sojourn time; this happens because the original series can give successive strong events, if examined in the subspace of the winter and autumn seasons that correspond to different events and not necessarily to the same event that persists in

time. This means that one strong event can be suppressed during spring and summer and it can arise again in the next autumn-winter period, so the sojourn time referred to the chain of autumn-winter will be overestimated. However, this overestimation can give information about the time in whom you can find extreme events consecutively. Since the transition matrices are affected by error, to compute the mean sojourn time and its variance and keep into account this intrinsic uncertainty, the method of the ensemble is used again. For each of the four matrices, it is built an ensemble varying the probability in the range of the confidence level, considered with the constraint that the sum of each row must be equal to one. Then, for each member of the ensemble, the mean sojourn time and variance are computed, and an average of these two sets is done.

Another interesting property that must be considered, is that a transition matrix, defined on a finite number of states, always possess at least one invariant density probability. A discrete density probability $\pi^{nn} = (\pi^{nn}_{A^-}, \pi^{nn}_{N^-}, \pi^{nn}_{N^+}, \pi^{nn}_{A^+})$ is said to be invariant for the transition matrix $\hat{\mathbb{W}^{nn}}$ when

$$\pi^{nn} = \pi^{nn}\hat{\mathbb{W}}^{nn} \tag{5.15}$$

that implies

$$\pi^{nn} = \pi^{nn}(\hat{\mathbb{W}}^{nn})^l, \quad \forall l\,. \tag{5.16}$$

If the transition matrix is regular, this invariant probability is the only one. Looking for these invariant probability means, again, to find the long-time PDF for the different seasons. This can be seen as an another check, a test to verify that these matrices are able to reproduce the asymmetry of the probability distributions along the time.

In the following, some important elements that contribute to characterize a Markov chain are recalled. I have defined with $f_i^{n,(s)}$ the probability that the chain associated to the transition matrix $(\hat{\mathbb{W}}^{nn})$, with initial state $i \in \mathbb{T}$, returns to the state i after s-step for the first time. This probability is different from $\hat{\mathbb{W}}^{nn}_{ii}$, which can contain any returns

in the state i also before the step s. In general, $f_i^{n,(s)}$ can be found iteratively:

$$f_i^{n,(1)} = (\hat{\mathbb{W}}^{nn})_{ii} \tag{5.17}$$

$$f_i^{n,(s)} = [(\hat{\mathbb{W}}^{nn})^s]_{ii} - \sum_{r=1}^{s-1} f_i^{n,(r)} [(\hat{\mathbb{W}}^{nn})^{(s-r)}]_{ii}, \quad s \geq 2. \tag{5.18}$$

With this definition, the probability that the chain returns back at the state i at any time is

$$f_i^n = \sum_{r=1}^{+\infty} f_i^{n,(r)}. \tag{5.19}$$

If $f_i^n = 1$,the return is ensured and the state i is defined as recurrent or persistent, while if $f_i^n < 1$, the state i is defined as transient.

If all states are reachable from the other ones in a finite number of steps, and the system can not be trapped in a particular ensemble of states, the chain is said to be irreducible.

The states can also be classified as periodic or a-periodic; this is an important feature in the studying of ENSO. A state i has a period of d, with $d > 0$, if, starting from the state i, the chain can only revisit it sd-steps later for some positive integer s: d is the greatest common divisor of s for which $[(\hat{\mathbb{W}}^{nn})^s]_{ii} > 0$. A state i is said to be periodic if its period $d > 1$; otherwise the state is a-periodic.

After these preliminaries, these matrices are used to highlight, with a simple example, the predictability properties of the system during the 1997. In this period a strong El Niño event occurred and the model had big difficulty in its prediction. Clearly, nowadays the more and more powerful and accurate GCMs are able to do really amazing forecast, but these matrices can be used to quickly understand the difficulties in the predictability for those forecast.

Once the transition matrices for the real phenomenon are obtained, it could be interesting comparing them with the one obtained by a simple sinusoidal signal with noise and by a GCM. The first comparison helps us to understand how much ENSO can be seen as an oscillatory phenomenon while the second comparison can highlight the difference between the model and the reality.

5.3 Application

5.3.1 A simple experiment

Before starting to characterize ENSO by means the transitions probability matrices and compare them with the matrices of the GCM model, it could be interesting looking for the signature that a periodic signal modified by noise could leave in these matrices. This signature can help us in detecting trace of simple oscillatory behavior of the phenomenon under study, both in the observations and in the models. To do this, I have performed a simple experiment. I have used a monthly data time series build up with the following periodic function disturbed by strong noise:

$$SSTA(t) = \frac{1}{2}\sin(\omega t) + \eta, \tag{5.20}$$

where $\omega = \frac{2\pi}{12}$ is the pulsation corresponding to a one-year period, and η is a stochastic forcing with a Gaussian distribution centered in zero and with a standard deviation equal to 0.6. I have used a period of 10^5 years for this time series to write down the transition probability matrices. In Fig. 5.3 it is shown a little period of this evolution.

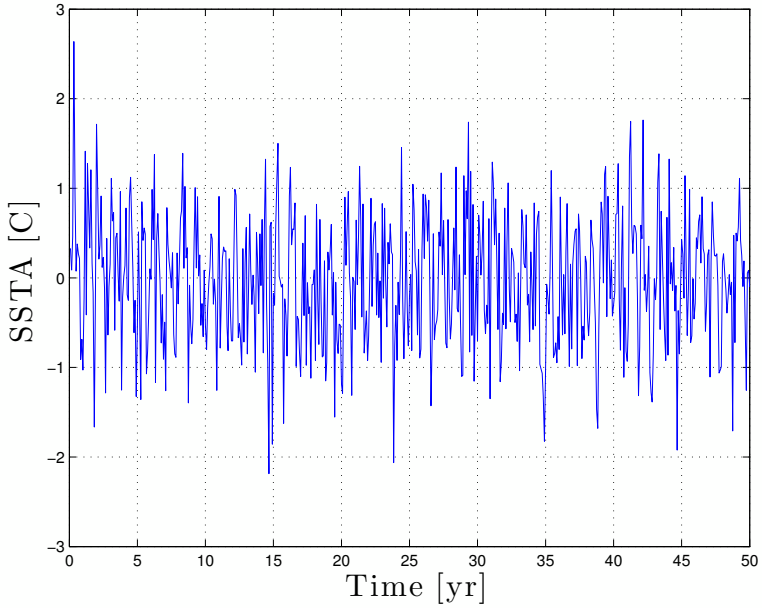

Figure 5.3: An example of the time series evolution for the sinusoidal experiment with noise, Eq. (5.20).

The values of amplitude, frequency or the value of the phase of the sinusoidal signal

in this experiment are not important . I have just wanted to see how an oscillatory noisy signal is represented in these matrices. Clearly, different phase, frequency or amplitude would shift coherently the probability into the matrices. The values for the amplitude and noise, however, are chosen to be sufficiently hight to allow the experiment time series to span the four states of the ENSO time series. If the amplitude of the signal or the one of the noise are too short only few entrances of the matrices are different from zero, and the transitions become trivial.

In Fig. 5.4, the probability transition matrices for this experiment are shown. In this case, the signature of the deterministic periodic function used in Eq. (5.20) is reflected in the fact that some matrices tend to be equal, in particular $\hat{\mathbb{W}}^{n,k}$ with k fixed and $n = 1, 2, 3, 4$.

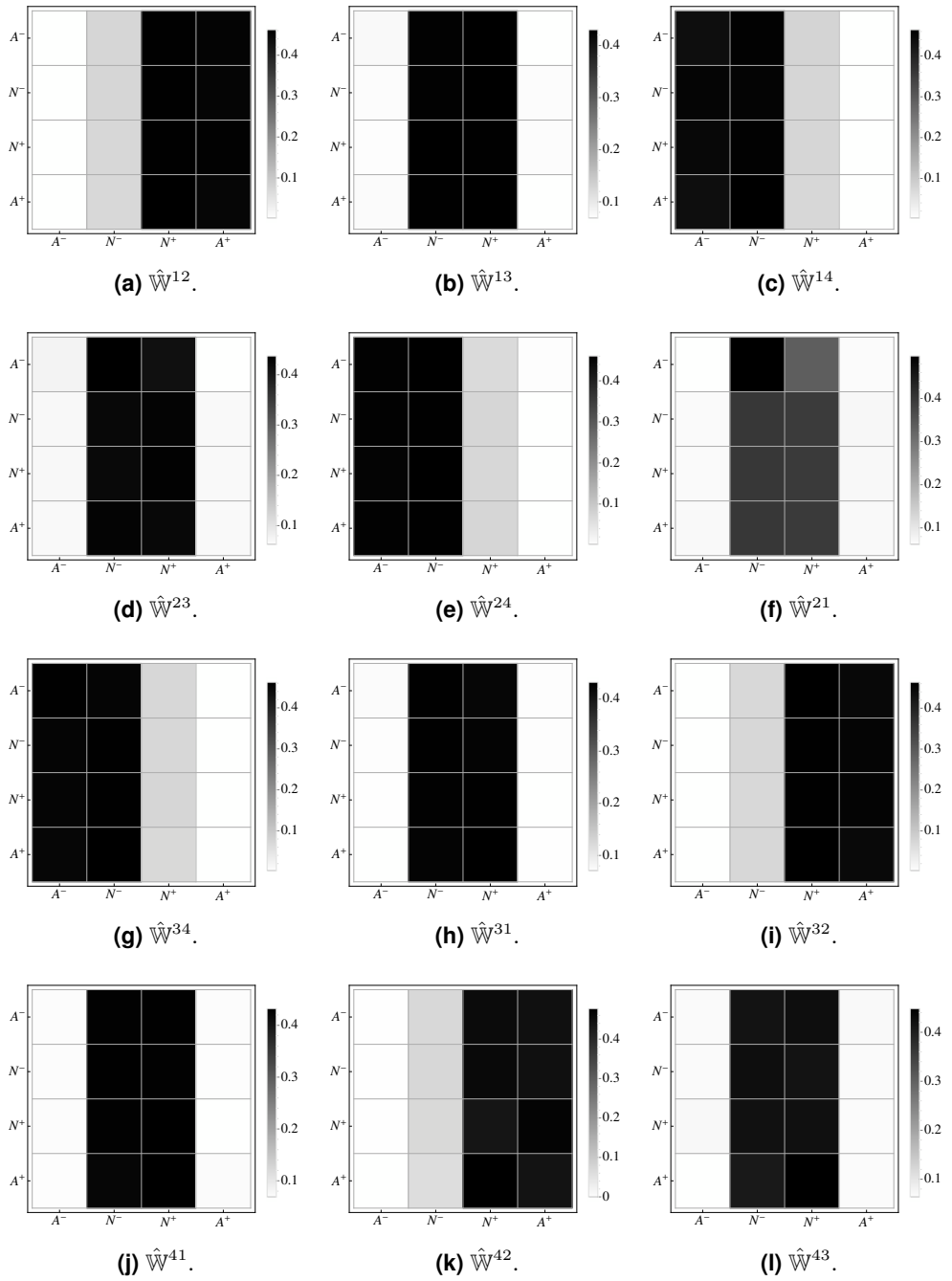

(a) $\hat{\mathbb{W}}^{12}$. **(b)** $\hat{\mathbb{W}}^{13}$. **(c)** $\hat{\mathbb{W}}^{14}$.

(d) $\hat{\mathbb{W}}^{23}$. **(e)** $\hat{\mathbb{W}}^{24}$. **(f)** $\hat{\mathbb{W}}^{21}$.

(g) $\hat{\mathbb{W}}^{34}$. **(h)** $\hat{\mathbb{W}}^{31}$. **(i)** $\hat{\mathbb{W}}^{32}$.

(j) $\hat{\mathbb{W}}^{41}$. **(k)** $\hat{\mathbb{W}}^{42}$. **(l)** $\hat{\mathbb{W}}^{43}$.

Figure 5.4: Transition probability matrices obtained from a time series generated with a simple sinusoidal function with one-year period and noise. The signal to noise ratio used here is 0.6.

In Fig. (5.5), the one-year transitions are shown. In this case, I have plotted the matrices using graphs, as usually done to represent a Markovian chain; this choice is due to the fact that the one-year transition matrices for the observation can be considered as Markovian, due to the exponential decreasing of the autocorrelation function for the NINO3.4 time series, and I have used this kind of plot in these cases.

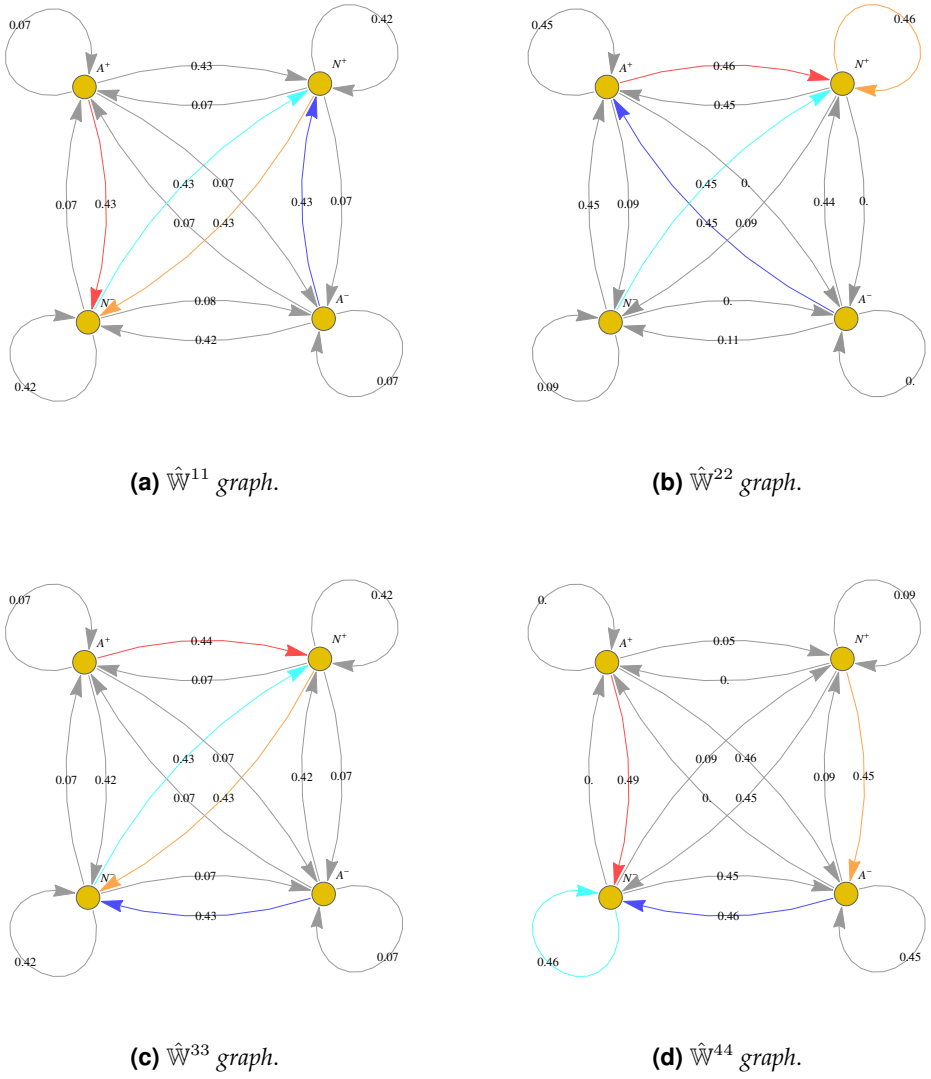

(a) $\hat{\mathbb{W}}^{11}$ *graph.*

(b) $\hat{\mathbb{W}}^{22}$ *graph.*

(c) $\hat{\mathbb{W}}^{33}$ *graph.*

(d) $\hat{\mathbb{W}}^{44}$ *graph.*

Figure 5.5: Transition probability matrices for the one-year transition. The typical graph plot is used to represent the Markov transition matrices. All the nodes (states) are connected each other; for this reason the same color (yellow) has been used to indicate them. The blue, cyan, orange and red arrows respectively highlight the most probable transition for the states A^-, N^-, N^+, A^+.

Some transitions are almost prohibited (and they are indicated by an arrow with zero value for the probability, since are reported values with just two digits in these plots), and the states tend to be non-persistent, the system prefers to transit in different states at every step.

Due to the high value of the noise variance that has been used, the entrance of this one-year transition matrices are all different from zero, and some values are really small but different from zero. For this reason, the states are recurrent, and these graphs

are irreducible. The states for these subchains result to be a-periodic, using the definition of the previous paragraph. The periodicity of the deterministic part of the oscillation is detected in the equivalence of some matrices, as explained above, and the fact that the states of the one-year transitions are a-periodic, is a consequence of the noisy part of the signal.

5.3.2 ENSO's transition probability matrices

In the following, I have treated the case of the NINO3.4 index computed from the observations. In Fig. 5.6, the transition probability matrices for transition period less than one year are shown. These matrices are found using Eq. (5.2), and the confidence interval with confidence level $CL = 95\%$ using Eq. (5.5). The numerical values of these matrices with the errors are shown in the appendix **??**. The first column of the figure shows the two-seasons transitions, which are the transitions that involve two seasons: the starting season and the ending one. The highest values of the probabilities are denser around the diagonal of these matrices. This means that this first set of matrices shows the persistence of the system. After one season, the system does not change too much; this is particularly true for the autumn-winter transition matrix $\hat{\mathbb{W}}^{14}$, while the less persistence is shown in the spring-summer transition matrix, $\hat{\mathbb{W}}^{23}$. This quick loss of information, in the sense that more final states are accessible now with a similar probability, is due to the SPB. This interesting feature also appears with just four states.

The second column shows the three seasons transition. The effect of the loss of information, due to the SPB, appears more evident here, in particular in the matrix $\hat{\mathbb{W}}^{24}$ where the loss of information due to the SPB has already started in the previous transition. For this matrix the state A^- is the most stable. In this column another interesting feature appears. The matrix $\hat{\mathbb{W}}^{42}$ seems to be again diagonal, or better still, the favored transitions are denser along the diagonal. In this case the a bit of persistence appears also here, although an inevitable homogenization of the probability has begun. The period autumn-winter is particularly stable.

The third column of the figure, the four-seasons transition, highlights the feature discussed above. The matrix $\hat{\mathbb{W}}^{14}$ has now the probabilities spread all around the matrices, this is because two seasons after spring are involved, while the matrix $\hat{\mathbb{W}}^{32}$, that passes through autumn and winter, tends to becomes more diagonal; the transi-

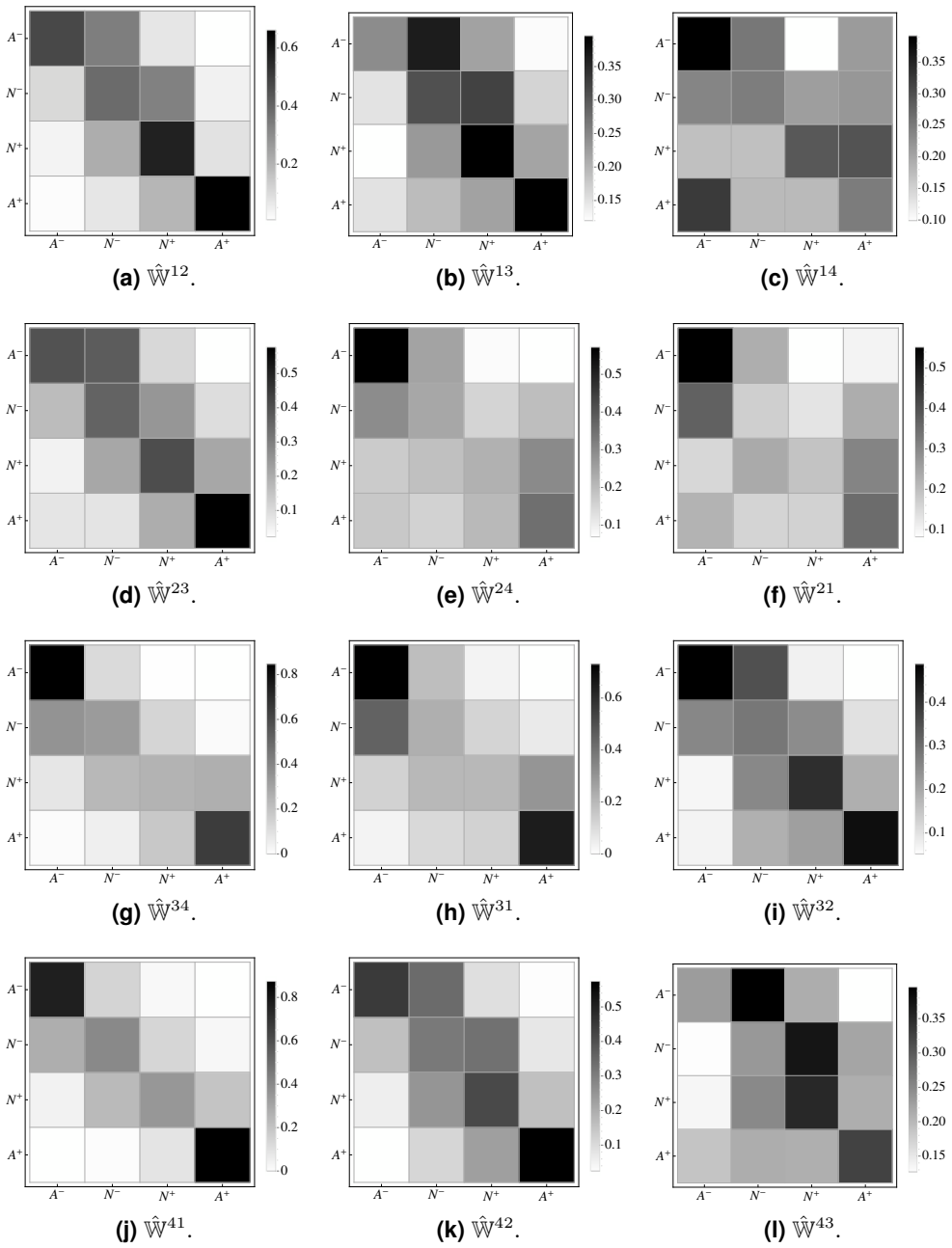

Figure 5.6: Transition probability matrices computed with Eq. (5.2) for the 159-years NINO3.4 time series. The period 1856-1949 is a reconstruction (Kaplan et al., 1998) while the period 1950-up to now derives by the NOAA Climate Prediction Center.

tions that have bigger probabilities values are the persistent ones, from one state to the same state. However, the discrete probability for every row of the matrix is always more uniform like.

In these matrices the information loss is continuos, while for an oscillations disturbed by noise, as in the simple experiment performed in the previous section, this is not true. The one-year transition matrices are shown, using graphs, in Fig. 5.7. The

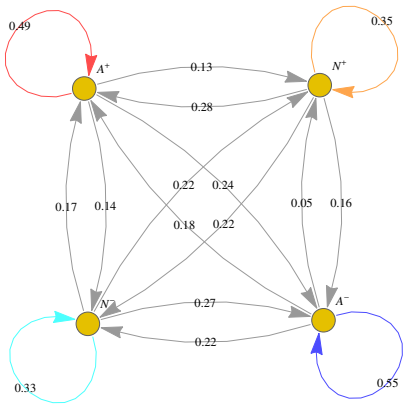

(a) $\hat{\mathbb{W}}^{11}$ *graph.*

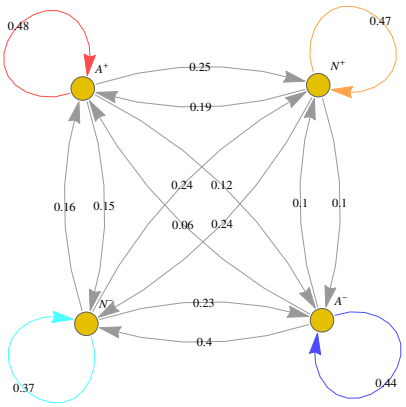

(b) $\hat{\mathbb{W}}^{22}$ *graph.*

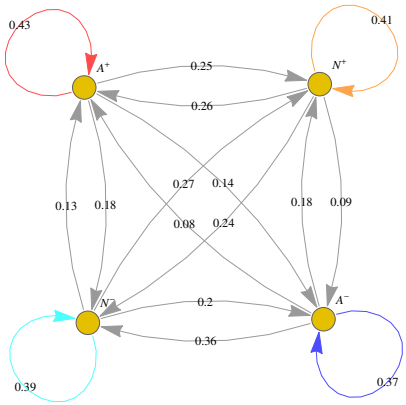

(c) $\hat{\mathbb{W}}^{33}$ *graph.*

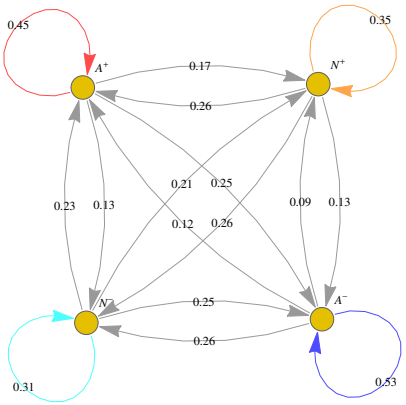

(d) $\hat{\mathbb{W}}^{44}$ *graph.*

Figure 5.7: As Fig. 5.5, but considering the NINO3.4 observations.

four states have again the same color because they are all related, being these matrices are irreducible. As before, the colored arrows highlight the highest probability transition for each states, and you can see another important difference from the experiment performed in the previous section. Here, all the Markovian subchains show that the persistence is the favorite transition. The preferred final state is the initial one, for all the states. For the matrices in the previous experiment the final preferred state is different from the initial one, except for one of the states. Something similar is obtained also if a lower frequency for the $\sin$ is used, not shown here.

Since the probability distribution for the winter and autumn period is larger, as shown in Fig. 5.1, El Niño and La Niña events appear more frequently in the subchains represented by the matrices $\hat{\mathbb{W}}^{11}$ and $\hat{\mathbb{W}}^{44}$. This is why the value of the probability for the persistence in these two plots is higher than in the matrices $\hat{\mathbb{W}}^{22}$ and $\hat{\mathbb{W}}^{33}$ for the spring and summer subchains where the PDF is more gaussian.

All these matrices turn out to be irreducible, with recurrent and a-periodic states. The role of the stochastic forcing in the ENSO phenomenon is really important.

All these processes admit a limit discrete PDF,

$$\pi^{nn} = \lim_{l \to +\infty} [\hat{\mathbb{W}}^{nn}]^l, \tag{5.21}$$

shown in Fig. 5.8. In these pictures the discrete PDF computed directly from the data is shown for comparison, Fig 5.1b. All the matrices seem to be able to describe the behavior of ENSO in the four seasons. Even though the time series used, is not really long, just 159 years, the matrices obtained provide a valid estimate of the real ones. Applying Eq. (5.10), I have been able to compute a clear index for the predictability of the ENSO evolution, as shown in Fig. 5.9. For every starting season, ordered in the abscissa, I have computed the ENSO$_{idx}$ for each transition, represented with a different color line. The longer the period of the transition is, the less information remains in the system, that means that the phenomenon is less predictable. Actually, this is not completely true, since the yellow line, that represents the five-season transition, appears to be above the three and two-seasons transition for the first two-season, s_1 and s_2, and above the four-seasons transition if starting from season s_4. This could be the consequence of the probability of the persistence in these subchains.

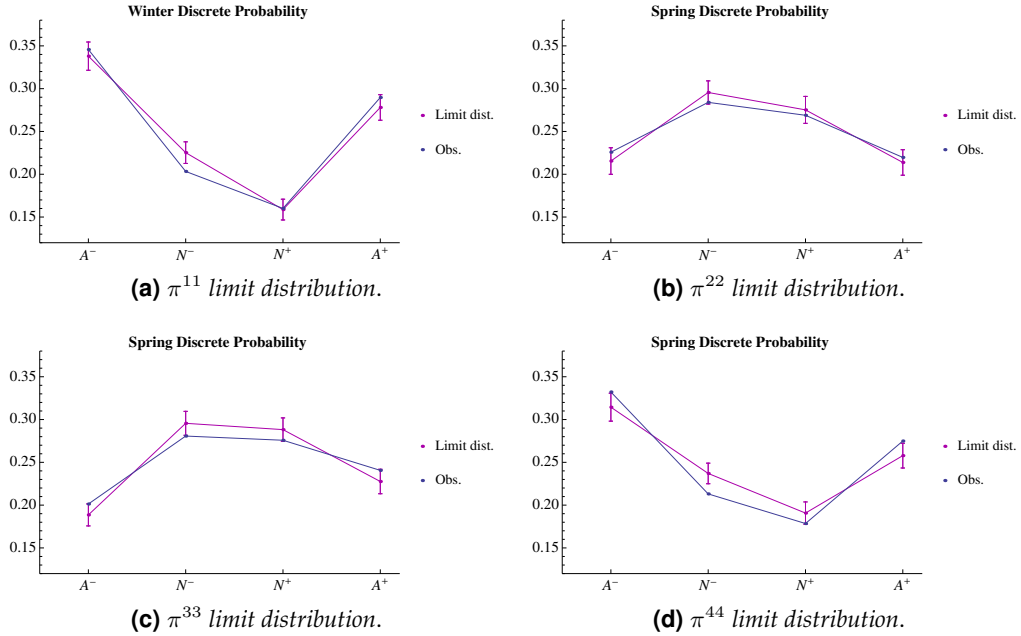

(a) π^{11} *limit distribution.* **(b)** π^{22} *limit distribution.*

(c) π^{33} *limit distribution.* **(d)** π^{44} *limit distribution.*

Figure 5.8: Comparison between the limit distributions of the one-year transitions probability matrices and the one directly obtained from the observation as in Fig. 5.1b. The limit distribution plotted is the mean of a distribution ensemble obtained varying the matrices according to their 95% confidence level interval. The error on each state of the limit distribution is one standard deviation of the obtained ensemble of states.

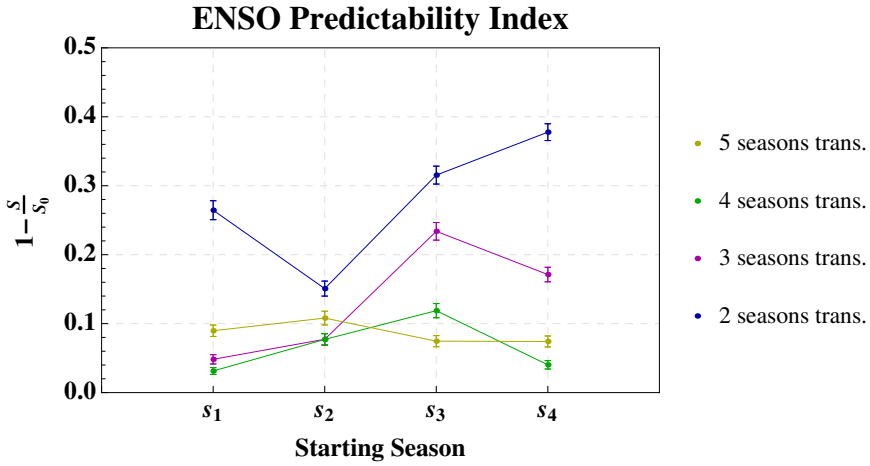

Figure 5.9: ENSO index computed using Eq. (5.10). On the abscissa the starting seasons are indicated, while different lines represent the number of seasons involved in the transition. The entropy used for every matrix is the mean of the entropy ensembles obtained varying the matrices according to their 95% confidence level interval. The errors on the entropies are one standard deviation of these ensembles.

But the most interesting things are in the blue and magenta curves, that show the index for the two and three-season transition. The effect of the SPB is clearly evident in the two-season transition starting from spring, s_2. In fact, for this matrix the curve has a well-defined minimum. The stability of the autumn-winter transition can be appreciated looking at the maximum of the blue line.

The effect of the SPB is also evident in the magenta line, three-seasons transition. Now it is the first point of the line that passes through spring and loses more information in respect to the other starting point, while the transition involving summer, as starting point, goes through the autumn-winter transition and limits more the loss of information than the others.

Looking at this index, an accurate long time prediction of ENSO seem to be impossible. This index gives an idea of the predictability for different transition periods, starting in different periods of the year. This is useful to compare the different seasons of the year. Clearly, in this plot is contained the global information of the different matrices. The index gives a relative information between different seasons transitions, but for different matrices the real discriminating for a good prediction is the initial state. Let us consider the matrix $\hat{\mathbb{W}}^{41}$. If you start considering the initial state in autumn that is a strong event, A^-, A^+, the peaks in the probability for the final favorite state in winter can reach the 90% of the total probability, but if you consider as initial states the neutral ones, the peaks in the final probability represent just the 40%, more or less, of the total probability. This is the reason why the global index shown in the plot for this matrix is the highest one but the value is small.

The matrix $\hat{\mathbb{W}}^{14}$ exhibits the maximum loss of information in respect to all the other matrices. Just as a further test, presented by the Eq. (5.11), I have tried to compute the long-time distribution using this matrix, Fig. 5.10. Also with this matrix, it is possible to recover the right result.

The mean sojourn time and variance can be computed using Eqs. (5.14). The right sojourn time, as explained, should be read from the matrices $\hat{\mathbb{W}}^{22}$ and $\hat{\mathbb{W}}^{33}$. The value can vary from six months to three years into a standard deviation, and that is a reasonable estimate.

Finally, it is shown a little example of forecast using these matrices. I have tried to analyze the year 1997, in which a strong ENSO event was missed by models. Only

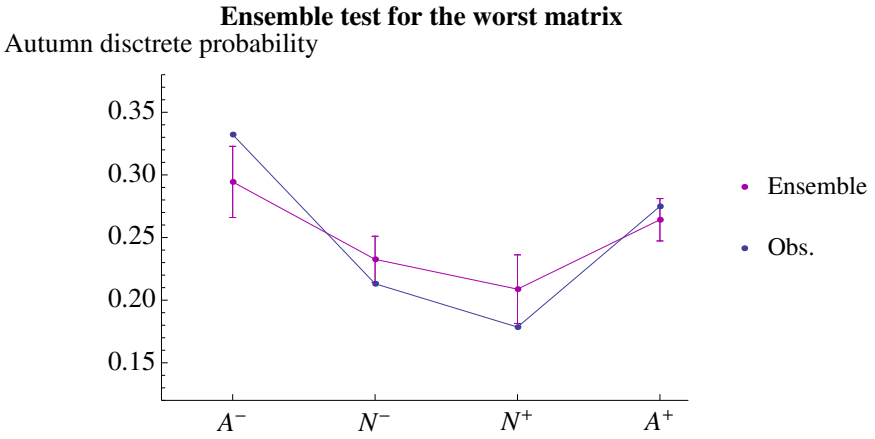

Figure 5.10: Comparison between of the seasonal probability obtained with Eq. (5.11) and one of the worst (in terms of distance from the uniform matrix) probability transition matrices, $\mathbb{W}^{1,4}$. The mean distribution is computed considering 10^4 random initial distributions, that are multiplied by variations of $\mathbb{W}^{1,4}$ according to the 95% confidence level interval. The error is one standard deviation computed from this ensemble for each state.

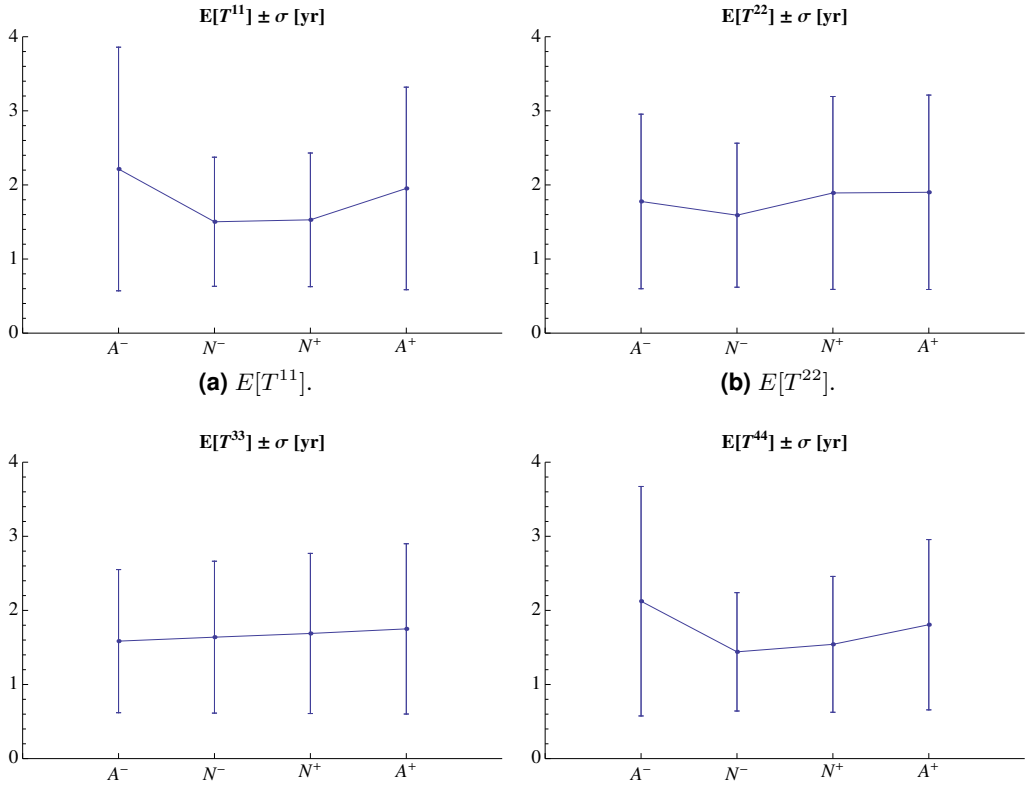

(a) $E[T^{11}]$. **(b)** $E[T^{22}]$.

(c) $E[T^{33}]$. **(d)** $E[T^{44}]$.

Figure 5.11: Mean sojourn time and standard deviation for the one-year transition matrices. Here the means and standard deviations of the sojourn time are plotted considering the means of mean sojourn time and variance ensembles obtained varying the matrices according to their 95% confidence level interval.

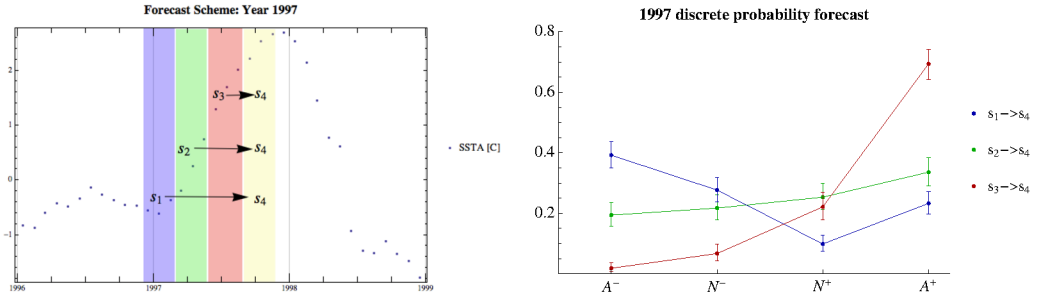

(a) *Forecast scheme for the year 1997. Season s_4 is forecasted starting from s_1, s_2, s_3.*

(b) *Discrete probability distribution of the s_4's states starting from s_1, s_2, s_3.*

Figure 5.12: Forecast of the preferred state of s_4 season starting from three antecedents seasons for the year 1997. Only the forecast $s_3 \to s_4$ is able to give a really peaked probability on the right state.

the forecast $s_3 \to s_4$ is able to give a really peaked probability on the right state. This is true not only for the year 1997, but it will be true for all the transition that start with similar condition. Clearly with the advance of the computation power, and with models that are able to take into account more physics, better results those obtained in 1997 could be reached; anyway this simple computation shows a sort of intrinsic un-predictability of this phenomenon, basically due to the strong noise forcing that sustains its oscillation.

5.3.3 Model comparison

The procedure applied to the observations above is repeated also for a 500-years run of the old coupled CMCC-CMS model, used in Davini et al. (2013). That model had a horizontal and vertical resolution of T63 L95. The top of the atmosphere was at 0.01 hPa. The ocean, OPA 8.2, had 2^{deg} resolution, as the sea ice grid simulated with LIM. This long run was made with pre-industrial conditions. The model used allows us to make a comparison with the observations, and easily evaluate if the model is able to reproduce the same transitions as the real phenomenon. From the model it is obtained the NINO3.4 index averaging the temperature (between $5°\text{N} - 5°\text{S}$ and $170°\text{W} - 120°\text{W}$) and subtracting the climatological cycle. Fig.5.13 shows the transition probabilities matrices for transitions that occur in a period shorter than one year. The first column shows the two-seasons transitions. As for the observation, the model shows a persistent behaviour also if the matrix $\hat{\mathbb{W}}^{23}$ seems to be affected quite quickly by the SPB. The autumn-winter transition, $\hat{\mathbb{W}}^{42}$, seems to be the most stable one again.

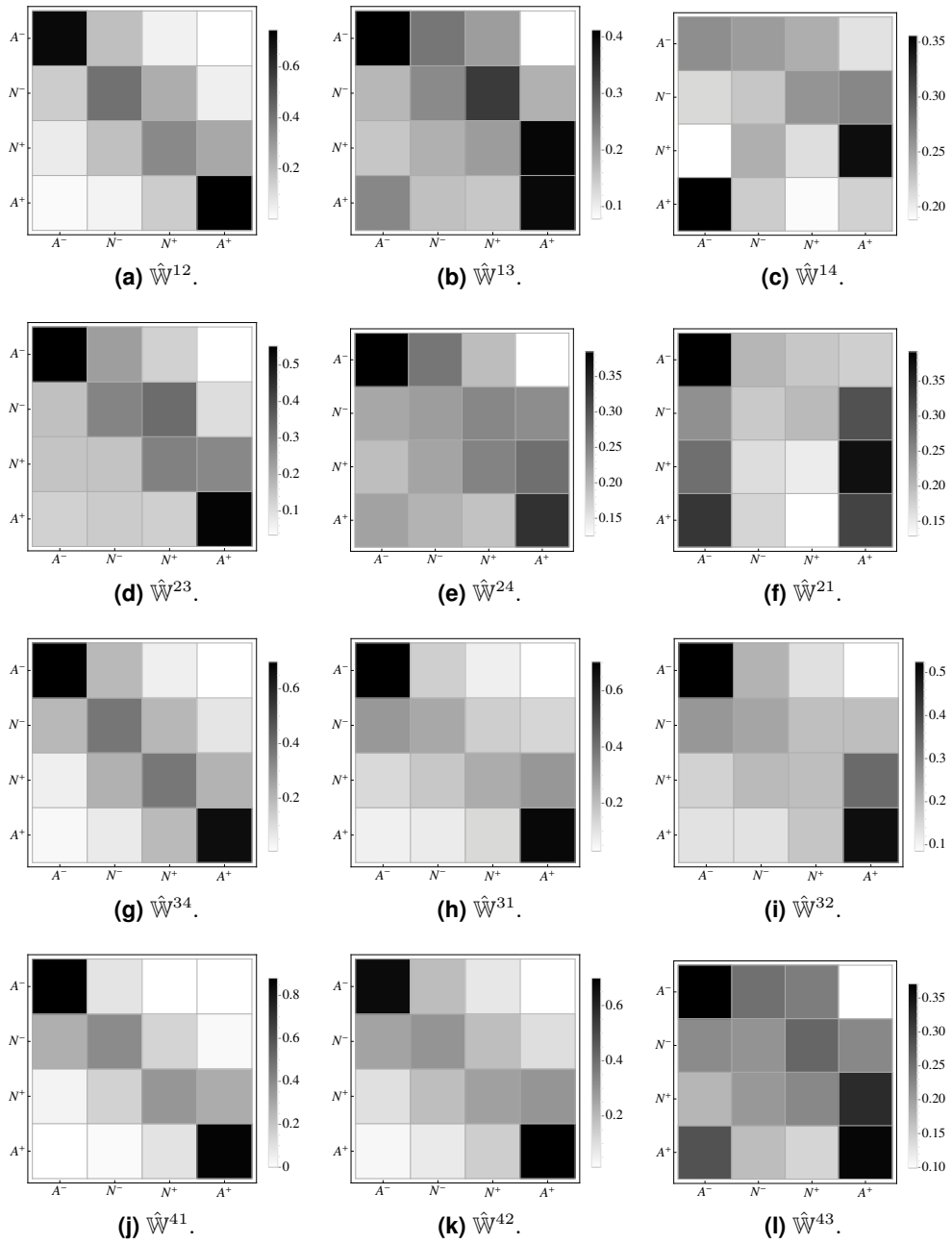

(a) $\hat{\mathbb{W}}^{12}$. **(b)** $\hat{\mathbb{W}}^{13}$. **(c)** $\hat{\mathbb{W}}^{14}$.

(d) $\hat{\mathbb{W}}^{23}$. **(e)** $\hat{\mathbb{W}}^{24}$. **(f)** $\hat{\mathbb{W}}^{21}$.

(g) $\hat{\mathbb{W}}^{34}$. **(h)** $\hat{\mathbb{W}}^{31}$. **(i)** $\hat{\mathbb{W}}^{32}$.

(j) $\hat{\mathbb{W}}^{41}$. **(k)** $\hat{\mathbb{W}}^{42}$. **(l)** $\hat{\mathbb{W}}^{43}$.

Figure 5.13: Transition probability matrices for the SSTA obtained with CMCC-CMS model.

The general behavior of these matrices seems to be good but there is a too fast deterioration in the information brought by these matrices. This can be appreciated in the Tab. 5.2 in which the distance Eq. (5.8) is used to compare the matrices obtained from the observation and the matrices obtained from the model. In Fig. 5.14, they are shown the graphs that represent the one-year transition matrices for the CMCC-CMS run. The persistence is present also here for almost all the states. Only the $\hat{\mathbb{W}}^{44}$ matrix exhibits for all the states a preference for the persistence. The problem here is the

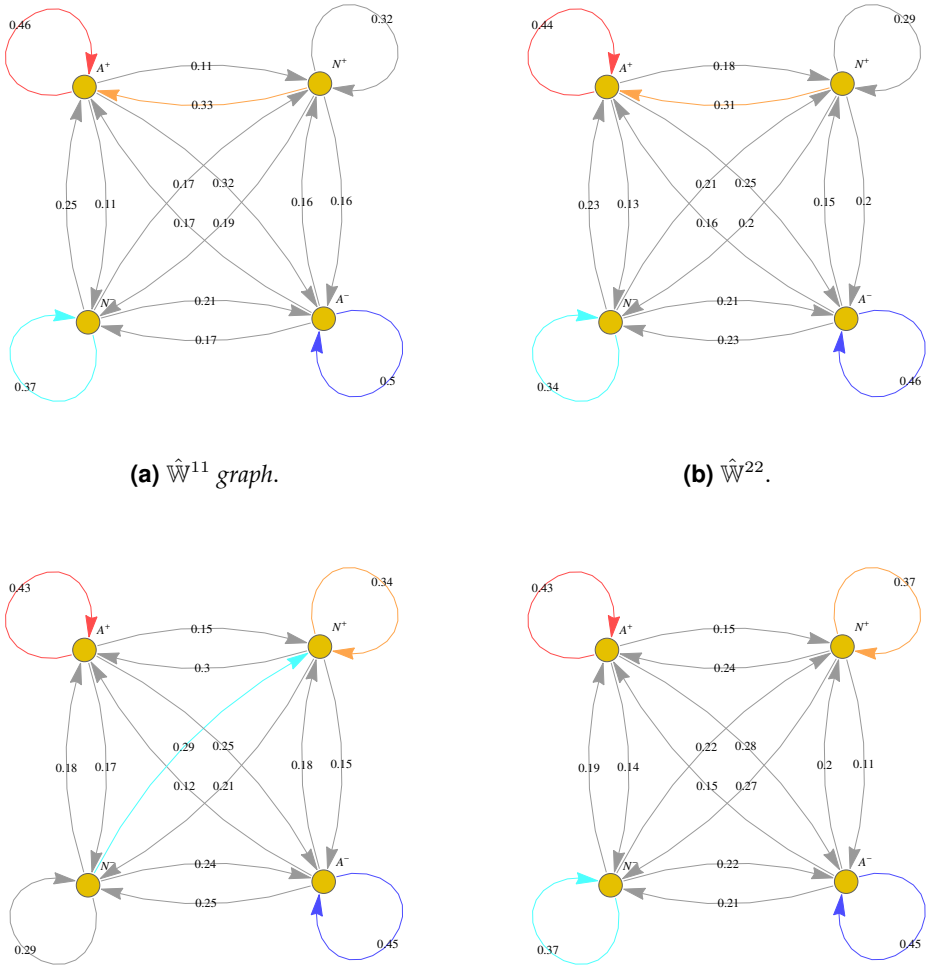

(a) $\hat{\mathbb{W}}^{11}$ *graph.* **(b)** $\hat{\mathbb{W}}^{22}$.

(c) $\hat{\mathbb{W}}^{33}$. **(d)** $\hat{\mathbb{W}}^{44}$ *graph.*

Figure 5.14: As Fig. 5.7, but considering the SSTA time series obtained from the CMCC-CMS model experiment.

same: these values are smaller than in the observation. The model changes state in an easier way in respect to the observations, but at the same time the negative states are always preferred. This is evident looking at the limit distribution for the four seasons, Fig. 5.15. Also during spring and summer the preferred states are not the neutral ones, as in the observation.

In Tab. 5.2, it is shown the distance between the probability transition matrix computed from the observations and the one computed from the CMCC-CMS model. It is remarkable that the transition that brings the system into spring presents the biggest distance. This is because in the model the effect of the SPB is quicker than in the observations and spring is a critical season.

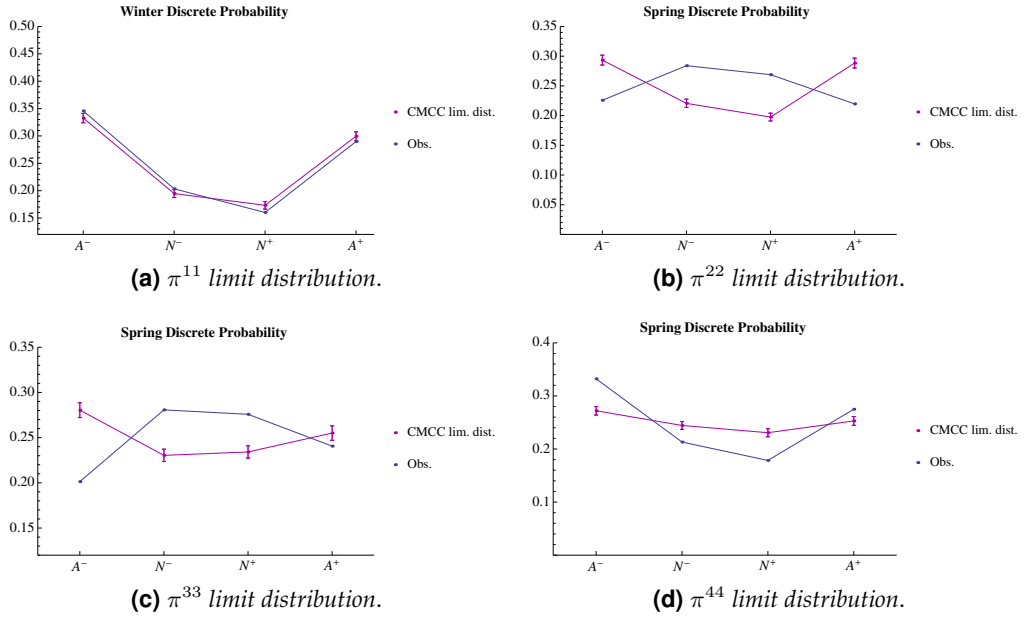

(a) π^{11} *limit distribution.* **(b)** π^{22} *limit distribution.*

(c) π^{33} *limit distribution.* **(d)** π^{44} *limit distribution.*

Figure 5.15: As Fig. 5.8, but considering the SSTA time series obtained from the CMCC model experiment.

$d_2(\hat{\mathbb{W}}^{nk}_{Obs}, \hat{\mathbb{W}}^{nk}_{CMCC})$		k			
		1	2	3	4
n	1	0.29 ± 0.02	1.13 ± 0.03	0.17 ± 0.02	0.41 ± 0.02
	2	0.19 ± 0.02	0.48 ± 0.03	0.37 ± 0.02	0.41 ± 0.02
	3	0.65 ± 0.03	0.59 ± 0.02	0.18 ± 0.01	1.05 ± 0.03
	4	1.28 ± 0.05	0.94 ± 0.03	0.13 ± 0.02	0.49 ± 0.03

Table 5.2: Summary table of comparison between the transition probability matrices computed from the NINO3.4 series and the one computed from the SSTA series of the CMCC model. The numbers in the table are the mean distances of the distances ensembles generated varying the two matrices according to the their 95% confidence level interval. The error is one standard deviation computed from these ensembles. The gray background highlights the highest distance once the starting seasons have been chosen.

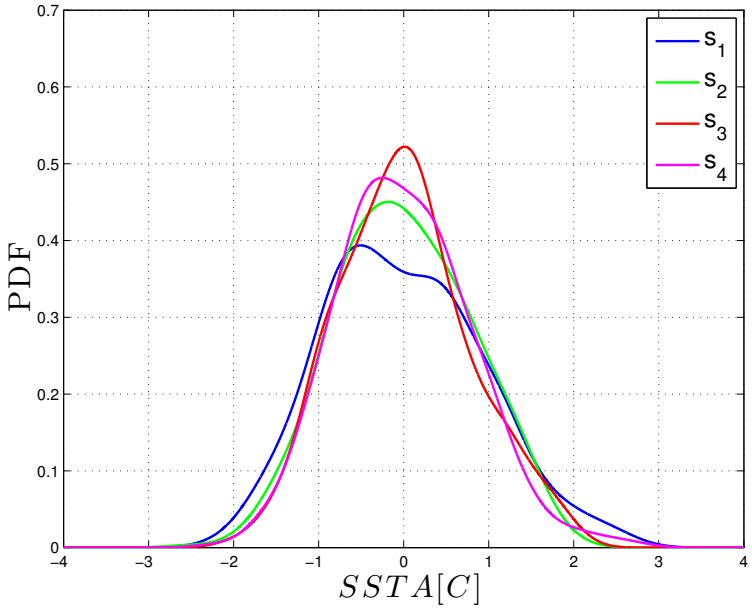

Figure 5.16: Long-time seasonal PDF computed from the NINO3.4 index, computed from the model time-series.

These asymmetries in the seasonal distribution can be highlighted also looking at the PDF for each season computed from the model time series, Fig. 5.16. The advantage of the transition probability matrices is that the whole process is seen in a more detailed way.

5.4 Discussion and Conclusion

I have tried to analyze an important climatic phenomenon, ENSO, by means of the probability transition matrices. For each season I have computed the transition probability matrices for the process that involves two, three, four and five (one-year transition) seasons. These matrices are not necessarily Markovian, even if with Markovian matrices more information could be extracted.

The values of the NINO3.4 series are grouped in four states, in such a way that the matrices considered have $4x4$ entrances. Since I have been able to compute the probability considering a time series of only 159 years, a more fine discretization did not make sense. Using only four states the statistic for small population was necessary to identify the confidence interval for the entries of the matrices, that represent the probability to move from one state to another one. Although this coarse discretization

is used, important features of the transitions are found and a general way to write index for the predictability of a phenomenon is presented.

The SPB appears clearly in these matrices and more clearly in the index found using the entropy of these matrices. The ENSO index for the predictability presented here brings the global information for the whole matrix considered. It is a measure of the predictability that considers all the possible initial and final states. Clearly if you are interested in a particular transition, for example the transition autumn-winter starting from a strong event, the peak of the final discrete probability density function could explain the 90% of the total probability. In this case the predictability should be really hight; however, if you consider all the possible transitions, from all the possible states this is not true, neither for the two-seasons transition matrices. The intrinsic unpredictability of ENSO, due to the strong stochastic component in its signal, is highlighted with a little fast forecast for the preferred state of the SSTA in the autumn of 1997, starting from one, two and three seasons before. In this particular case, the-two seasons transition, from summer to autumn, is the only forecast that is really able to catch the right final state with a clear peak in the probability distribution for that state.

Another feature, as the persistence or the capability of the system to move in others states starting from different seasons, appears clearly using these matrices. In particular, using the one-year transition matrices, that it is possible to suppose to be Markovian since the exponential decreasing of the autocorrelation function for the NINO3.4 index, the mean sojourn time for the four states can be estimated. The values obtained are reasonable, and this time scale arises naturally from the matrices without the use of Fourier analysis. This mean sojourn time, however, has also a big standard deviation; in fact, this time can vary into a standard deviation, from six months to three years. The scale appears to be reasonable looking at the time series, but highlights again the difficulties in ENSO prediction.

From the one-year transition matrices, it is computed also the limit distribution that matches with the one computed directly from the observations. This has been done to check ulteriorly the validity of these matrices.

To understand the trace left from an oscillatory signal disturbed by noise, a time series of this kind has been reproduced and the transition matrices have been used. One of the important differences between a signal of this kind and the one generated by

ENSO is that the probability transition matrices of ENSO tend to become uniform after long time transition, while for the other one this does not occur. Also the persistence of the four states is really different; this is to indicate that ENSO signal is generated by a more complex mechanism than a simple oscillation.

Finally, the transition matrices have been used to compare the NINO3.4 index computed from a GCM and the one obtained with the observations. Once computing the distance from the respective matrices, you can have an idea of how the phenomenon under study is well represented by the model, observing in a more detailed way in which state and in which period the model has a different behavior.

This tool is extendible to the study of the characterization of each climatic phenomenon and it is able to give a clear index regarding the predictability of the phenomenon under study.

This work can be extended to consider time series of field. Instead of studying a simple time series of a temporal varying quantity, it is possible to consider how it is varying a full field, that has also spatial information. One of the possible way should be to consider as states a certain set of Empirical Orthogonal Function (EOF), and looking at the probability that these particular states have to transit in another one. This could be an interesting subject to elaborete in a future work.

CHAPTER 6

CONCLUSIONS

The Stochastic Partial Differential Equations result to be a very important tool in the understanding of Climate System. The resolution of this kind of problems is far from trivial. In order to address these problems, I have proposed three different methods of investigation and I have applied them to Climate Dynamics with a particular focus on ENSO used as a model to test those ideas.

The first method, discussed in chapter 2, has been inspired by the Statistical Mechanics and Quantum Field Theory. Its power resides in the fact that it introduces a generating functional, from whom, using functional differentiation, all the n-points functions of the problem can be found. The generating functional is defined in terms of Path Integral, generally hard to evaluate. However, the computation can be carry out dividing the stochastic equation in two parts: the first one that involves linear differential operators (eventually also a linear term in the fields) and the other one, the interaction, that involves all the other terms also non-linear, but does not contain time derivatives. In this case, if a parameter, that can be used to label the interaction as a perturbation term into the equation, can be found, the computation of the generating functional can be related to the problem of finding a few Green's functions.

This method has been used in Navarra et al. (2013b) to find correlation and variance

of a (0d+1) simple model of ENSO with stochastic forcing. In this work, I have applied this method to a more complicated system, (2d+1), described by the Stochastic Barotropic Vorticity Equation into a channel. Periodic boundaries in the longitudinal direction and rigid walls bounding the channel to the north and south are used. I have solved the problem of finding the generating functional and I have used it to get analytical expressions for variance and correlation functions. In general, with this method I have been able to find all the n-points functions of the problem. I have presented here the study for three configurations of the SBPVE, obtained adding or neglecting damping and mean flow:

1. $\bar{\psi} = 0 \quad \mu^{-1} = 0$,
2. $\bar{\psi} = 0 \quad \mu^{-1} \neq 0$,
3. $\bar{\psi} \neq 0 \quad \mu^{-1} \neq 0$,

where μ^{-1} is the damping and $\bar{\psi}$ the mean flow. For each of these configurations I have found the analytic form that describes the variance and correlation of the stochastic field. When $\mu^{-1}t \ll 1$, i.e. damping for the time is small, the expression for the variance is reduced to the one found for the first configuration. Initially there is a linear increase of the variance before changing behavior when time increases. This is a typical behavior of the system subjected to Gaussian white noise. This framework could be extended to other kinds of noise. For the third case, if a mean flow profile, depending only on the meridional direction, the correction to the variance and correlation is basically reduced to the computation of an integral over the meridional direction. The interacting part considered here is the Jacobian, that appears in the SBPVE linearized around the mean flow. I have had to assume that the fluid is stable, but also in case of instability, if you know the typical time scale associated with it, τ_i, you could apply this method considering $t < \tau_i$ for an initial investigation.

I have shown that this technique is applicable to the SBPVE but with many technical difficulties. For this reason, instead of using the generating functional to analyze a more complicated model of ENSO, in respect to the one already treated in Navarra et al. (2013b), I have chosen others methods to study in depth a simpler ENSO model.

The second method, discussed in chapter 3 and 4, is based on the resolution of the Fokker-Planck equation, related to the stochastic system, via eigenfunctions expan-

sion. The content of chapter 3 has been published in Journal of Climate, (Navarra et al., 2013a). The ENSO model studied has been derived using a rotation in the space of variables of the Recharge Oscillator. This starting model is based on the positive Bjerknes feedback and does not consider explicitly delayed waves, but their cumulative effect into the parameters definitions. The stochastic forcing has been added to the rotated model to sustain the oscillation otherwise damped. This damping is granted thanks to the strong coupling between atmosphere and ocean used and the non-linear term into the equation. It is suggested a new way to consider ENSO, as a system that can jump between two states, one positive and one negative, represented by a potential which arises by the non-linearity that damps the system. The jumps are possible thanks to the stochastic fluctuations.

A probability distribution with many properties similar to the observed NINO3.4 can be obtained also in a regime that does not support self-sustained oscillations, characterized by large values of the coupling constant between stress and surface temperature. This regime has usually been neglected in the past as a regime where ENSO dynamics could not be deployed because of the absence of oscillations, but we have shown that indeed this may be the case if stochastic forcing is included. The theoretical probability distribution allows the calculation of time correlation and other quantities, showing that the asymmetry is necessary to achieve the time scales that are typical of ENSO.

Taking into account the MJO effect into the equation, we are able to set the different depth of the double well potential that describes the system, generating in this way a probability density that is asymmetric. The presence of the forcing breaks the symmetry, producing a more realistic asymmetric probability distribution between cold and warm states that also explains the gap in the probability of the warm to cold and cold to warm transition. The skewness of the distribution is increasing with the coupling parameter and realistic values can be obtained. We suggest MJO as a possible cause of the asymmetry in NINO3.4 probability distribution.

Using this model, I have also tried to exploit a periodic growth rate as cause of the predictability barrier, another important feature of ENSO. It is important to remark that before the rotation in the variable space, we modify the growth rate maintaining it positive to respect the positive Bjerknes hypothesis. The predictability barrier could

be explained by means the potential well. During autumn it becomes more and more asymmetric and gradually becomes parabolic in spring. This behavior influences the probability density function periodically and it is able to modify the persistence of the initial conditions. In particular, when the potential is more parabolic, the initial conditions result to be more persistent. It is impossible to obtain the exactly values of all the observables that characterize ENSO using more sophisticated CGCM, so there is no hope to explain exactly ENSO using such a simple model. A perfect reproduction of ENSO is not the aim of this work but rather trying to highlight all the mechanisms that, together with the Bjerknes positive feedback, are able to characterize ENSO, in particular the asymmetry of the probability density function and the spring predictability barrier.

The investigation prompted the idea that ENSO could be a system described by a sequence of state, rather than a simple oscillation. To check this idea, I have presented a third method of study discussed in chapter 5. It shows how the transition probability matrices can be used to deal climatic phenomena. Temperature anomalies are divided into four blocks, states, and the probability to move from one state to another has been calculated both for observations and General Circulation Model. In particular, these matrices have been used to define a predictability index of ENSO using their entropy. This index shows clearly the effect of the spring predictability barrier. For each season I have computed the transition probability matrices for the process that involves two, three, four and five (one-year transition) seasons. These matrices are not necessarily Markovian, even if with Markovian matrices more information could be extracted. Since I have been able to compute the probability considering a time series of only 159 years, a more fine discretization did not make sense. Using only four states the statistic for small population has been necessary to identify the confidence interval for the entries of the matrices, that represent the probability to move from one state to another one.

From these matrices one can read the capability of the system to transit or the persistence of the states. These matrices turned out to be a possible instrument for check models in respect to the observations. In particular, not only the the long-time seasonal probability density function could be checked, but also the single transitions for different states in different periods. Furthermore to understand the trace left from an

oscillatory signal disturbed by noise, a time series of this kind has been reproduced and the transition matrices have been used. One of the most important differences between a signal of this kind and the one generated by ENSO, is that the probability transition matrices of ENSO tend to become uniform after a long time transition, while for the other one this does not occur. Also the persistence of the four states is really different. This is to indicate that ENSO signal is generated by a more complex mechanism than a simple oscillation.

This work can be extended to consider time series of field. Instead of studying a simple time series of a temporal varying quantity, I could consider how it is varying a full field, that has also spatial information. One of the possible way should be to consider as states a certain set of Empirical Orthogonal Function (EOF), and looking at the probability that these particular states have to transit in another one. This could be an interesting subject to elaborate in a future work.

APPENDIX A

A BRIEF DESCRIPTION OF ENSO PHENOMENON

During the ENSO cycle, the two opposite phenomena, El Niño and La Niña, refer to the coherent and annual effects in sea-surface temperature, convective rainfalls, surface air pressure and atmospheric circulation that take place across the equatorial Pacific Ocean (`http://www.cpc.ncep.noaa.gov`). El Niño represents the warm phase of the ENSO cycle, and it takes place when the above-average sea-surface temperatures periodically develop across the east-central equatorial Pacific. On the contrary, La Niña refers to the periodic cooling of sea-surface temperatures and it represents the cold phase of the ENSO cycle. The periods when neither El Niño nor La Niña are present, are called ENSO-neutral and often coincide with the transition between El Niño and La Niña events. During these neutral phases, the ocean temperatures, tropical rainfall patterns, and atmospheric winds over the Equatorial Pacific Ocean are near the long-term average. During El Niño phase, the ocean presents a deep layer of warm water across the east-central equatorial Pacific, with sea-surface temperatures that exceed $1.5 - 2.5\,^{\circ}$C the average, and subsurface ocean temperatures typically $3 - 6^{\circ}$C above average at the depth of the oceanic thermocline. NOAA's Climate Prediction Center, which is part of the National Weather Service of the USA, considers the beginning of an El Niño episode when the 3-month average sea-surface temperature departure exceeds $0.5\,^{\circ}$C in the east-central equatorial Pacific (between 5°N $- 5^{\circ}$S and

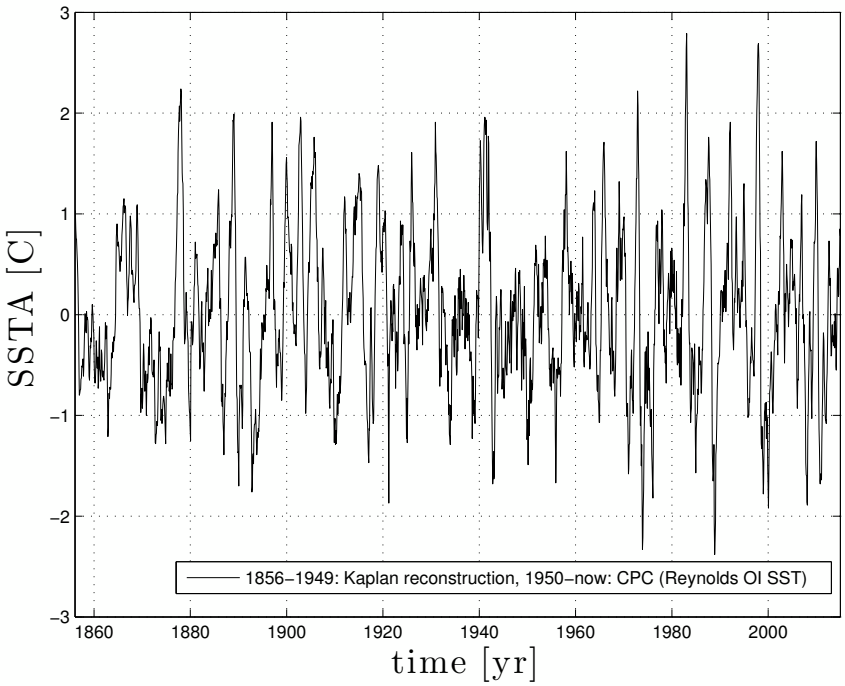

Figure A.1: NINO3.4 index, SST anomalies in $5°\text{N} - 5°\text{S}$ and $170°\text{W} - 120°\text{W}$, 1856-1949: Kaplan reconstruction, 1950-now: CPC (Reynolds OI SST), SSTA [C]

$170°\text{W} - 120°\text{W}$). This average, when the climatological cycle is removed, is also called NINO3.4 index. During this period, also a deeper than average oceanic thermocline (with depths typically ranging from $150 - 175$m) crosses the east-central equatorial Pacific. This phase lasts $9 - 12$ months (even though some prolonged episodes of El Niño have lasted $2 - 4$ years) and, as the opposite phase La Niña, typically develops during March-June; it is more intense during December-April (because the equatorial Pacific sea-surface temperatures are normally warmest at this time of the year), and then weakens during May-July. La Niña, the opposite phenomenon, tends to develop, reaches peak intensity and weaken during the same periods in the year as El Niño, but it typically lasts 1-3 years. It is characterized by a deep layer of cooler ocean temperatures that crosses the east-central equatorial Pacific; sea-surface temperatures are typically 2-4C below average at the depth of the oceanic thermocline which is shallower than average and it crosses the east-central equatorial Pacific, with depths ranging from $50 - 100$m. In Fig. A.1, it is shown the NINO3.4 index since 1856 up to now. Data in the period 1856-1949 derive from a reconstruction (Kaplan et al., 1998) and the ones from 1950 up to now from the observation of the Climate Prediction Center of the NOAA, (`http://www.cpc.noaa.gov/data/indices/`).

Changes in the ocean surface temperatures influence tropical rainfall patterns and atmospheric winds, which in turn impact the ocean temperatures and currents, changing the weather patterns; during December-April, when the equatorial Pacific sea-surface temperatures are normally warmest, a slight warming of the waters due to El Niño can result in a major redistribution of tropical convective rainfall, whereas a slight cooling due to La Niña can restrict the tropical convection to Indonesia. Furthermore, in the period December-April, during El Niño, the Pacific warm pool and associated area of deep tropical convection expand to well east of the date line, while during La Niña they are confined to well west of the date line; the tropical easterly trade winds are weakest during El Niño, while they are strongest during La Niña. The fact that El Niño and La Niña-related sea-surface temperature and tropical rainfall anomalies have effects on the wind patterns that in turn further amplify the sea-surface temperature anomalies, is a very important aspect of both the phenomena. These extreme climate episodes have an huge impact on the economic costs of the United States; advances in improved climate predictions could save a large amount of dollars in damage costs and they could also result in heightened economic opportunities for agriculture (plan for, avoid or mitigate potential losses), fishing, forestry, energy sectors and social benefits.

A.1 ENSO as a damped oscillation sustained by the noise

If ENSO must be simulated, what are the main elements that have to be taken into account? How the parameters of the model have to be chosen? Must a simple model have parameters set up to sustain the neutral oscillations, that make grow indefinitely the trajectory and needs stochastic forcing to recover oscillations, or must they set up to obtain a damped or stable oscillator? What is the regime of this model? Probably, real ENSO must be described by parameters that change in time, that are able to bring the system in different regimes in different periods of time.

However, Burgers et al. (2005) showed that a linear fit to observations leads to the remarkably simple picture of ENSO represented by a classical damped oscillator, with sea surface temperature and thermocline depth playing the roles of momentum and position, respectively.

There is also evidence that random atmospheric disturbances could influence the development of El Niño in some occasions (McPhaden and Yu, 1999), as happened in 1997.

ENSO could have its source of irregularities given by non-linear terms in its dynamics, but that is not the only cause.

ENSO should be seen as a damped oscillator sustained by the noise. In Fig. A.2, it is shown a phase diagram considering the sea surface temperature anomalies (SSTA) and its first derivative in time. There is not evidence of deterministic cycles, but it is possible to appreciate a region that seems to contain at least an attractor fixed point, around which stochastic forcing stretches the system. In Fig. A.3, it is shown a phase-

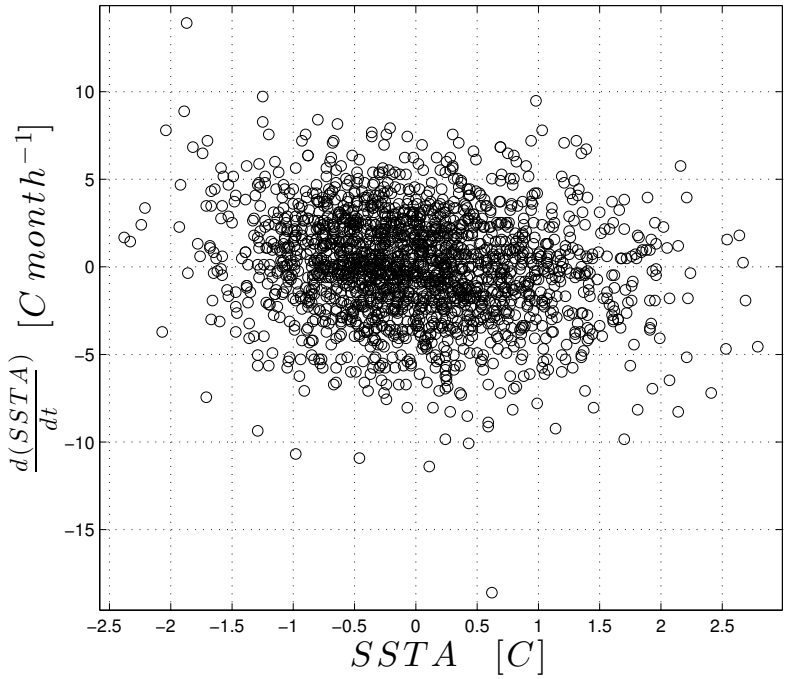

Figure A.2: Phase plot considering SSTA and its first derivative in time. There is not evidence of deterministic cycles , but it is possible to appreciate a region that seems to contain an attractor fixed point, around which, stochastic forcing stretches the system.

space diagram obtained by plotting the SSTA(t) versus SSTA(t-τ), where τ is a delay time chosen here to be one year. The time series for the SSTA has been subsampled at the frequency of one year, that is the frequency of the annual cycle forcing. There is no evidence here of natural oscillation, that should be manifested here as a single point in the plot, or cycle, that should rise as a consequence of a second frequency incommensurate with the frequency of the annual cycle. There is not even evidence of pure

chaos, usually highlighted by some patterns that manifest the mixing property of the system. Here, there is strong irregularity. This does not mean that chaos, or locking between the annual cycle forcing and frequency of the non-linear system describing ENSO, are not important for this system, but that noise must be an important component of it. The time series used considers the NINO3.4 index since 1856 up to now. The data related to the period 1856-1949 derive from a reconstruction (Kaplan et al., 1998) and the ones from 1950 up to now from observation NOAA. To further empha-

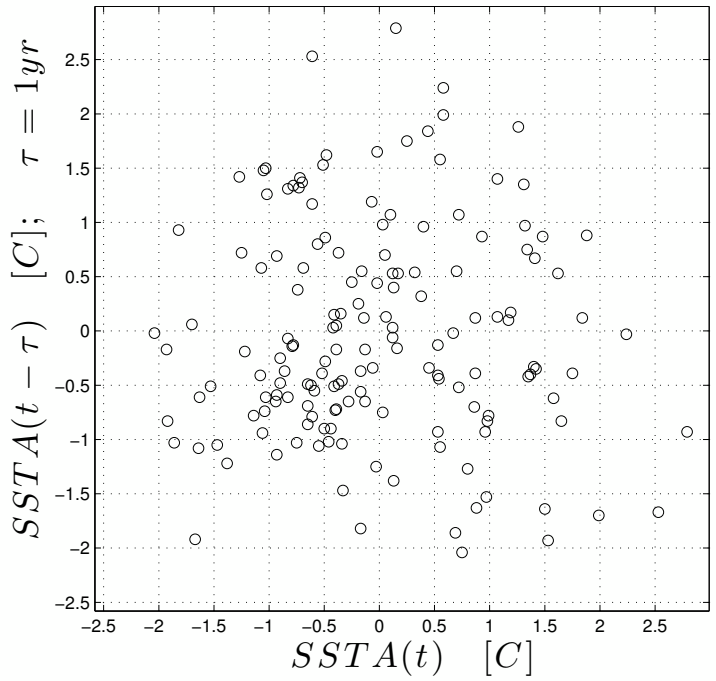

Figure A.3: Phase-space diagram obtained by plotting the $SSTA(t)$ versus $SSTA(t-\tau)$, where τ is a delay time chosen here to be one year. The time series for the $SSTA$ has been subsampled at the frequency of one year.

size these features, it is possible looking at the observed western anomaly depth of the thermocline, h_w, and the observed sea surface temperature anomaly (SSTA) of the NINO3.4 zone. For the anomaly depth, it is considered the average of it over the region $120°\text{E} - 180°\text{E}$ and $10°\text{S} - 10°\text{N}$ above the $20\,°\text{C}$ isotherm. It has been considered the period from February 1982 to August 2014, using the data of the IRI/LDEO Climate Data Library. These are considered the key variables for the explanation of the El Niño Southern Oscillation. In Fig. A.4, it is shown how the system described by these two variables, h_w and SSTA, could be summarized by a damped oscillator subject to some stochastic forcing.

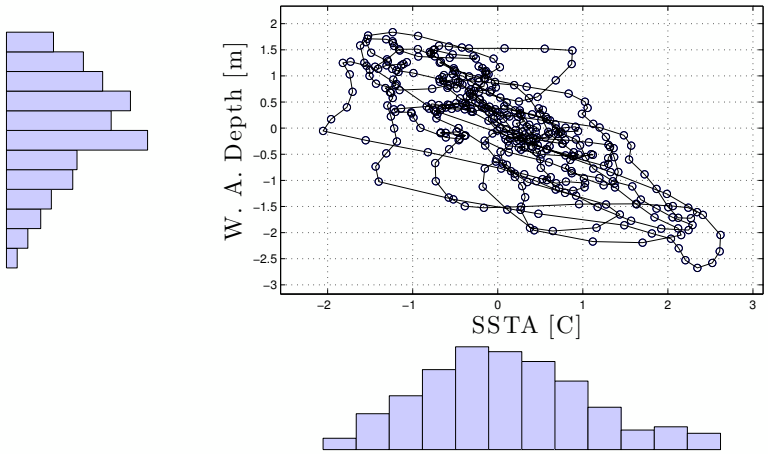

Figure A.4: Scatter plot of the two most important variables supposed to describe the ENSO system. There is not a clear sustained oscillation, but rather lots of damped oscillations exited stochastically. Along the axis is also plotted the histogram distribution for the variable considered. These histograms show an important asymmetry that characterizes ENSO.

A.2 Recharge Oscillator as starting point for the ENSO explanation

With the instrument briefly discussed in the previous section, I have studied the simple model discussed in Navarra et al. (2013a). Let's start with the Recharge Oscillator (RO) (Jin, 1997a). This model can be theoretically derived using the shallow water model under the long wave approximation on the equatorial β-plane (Jin, 1997b). One of the peculiarity of the RO is that no time-delay must be introduced. The description of slow ocean dynamics differs from the one introduced for example by Battisti and Hirst (1989), in which the western thermocline h_w is simply proportional to $\hat{f}(t-\tau)$ where $\hat{f}$ is proportional to the zonal integrated wind stress in the ENSO region and τ is a delay (the time for Rossby waves from the center of the forced region to the western boundary). This wave-delay, empirically added, can be theoretically justified with the two-strips model (Jin, 1997b) only neglecting the eastern boundary reflection, which means neglecting South America. This is a very strong hypothesis; moreover, this time-delay introduces an infinite number of degrees of freedom, each of them representing the different spatial scales of the Rossby waves. In the RO, the pressure gradient force accompanying the thermocline depth tilt along the equator is considered in Sverdrup balance with the equatorial wind stress, this is written as

$h_E - h_W = \hat{f}$ (h_E and h_W are the eastern and western thermocline depth). The last relation fits very well the observation, and no wave-delay appears. Here the explicit waves propagation is omitted, and the collective role of the equatorial wave in achieving the quasi-equilibrium adjustment dynamics is accounted with a proper parameter that represents the time scale of the process. Because of these reasons, in my opinion, the RO is a good starting point to find out a simple model of ENSO, described with just one variable. In the following, the subscript E, for the eastern SSTA, that from here is indicated with T , and W for the western thermocline depth variable are neglected.

The modified RO can be written as

$$\frac{dh}{dt} = -rh - \alpha\mu b_0 T + \gamma_h + \eta' \tag{A.1}$$

$$\frac{dT}{dt} = (\gamma\mu b_0 - c)T + \gamma h - (\mu b_0 T + h)^3 + \gamma_T + \eta' \,. \tag{A.2}$$

$\frac{1}{r}$ is interpreted as a damping timescale for the wave adjustment process, α is the proportional parameter between the wind stress and $\hat{f}$ the zonal integrated wind stress, while b_0 is the proportional parameter between the wind stress forcing and the temperature. The coupling constant μ regulates the strength of the interaction between the ocean and atmosphere. The parameter γ takes into account the thermocline upwelling process, while $\frac{1}{c}$ is the timescale for the relaxation of the SSTA toward the climatology (or zero anomaly). The parameters described above are also presented in the original system, and the same non-dimensional values are used (Jin, 1997a), while γ_T, γ_h are the idealized effect of the MJO on the equatorial dynamics. Here η' is the Gaussian white noise that has to be characterized by the value of its correlation strength.

APPENDIX B

STABILITY ANALYSIS

In this appendix, I have discussed some features not shown in the published paper (Navarra et al., 2013a), in particular in the following, a stability analysis of the rotated model is presented

$$\frac{dz}{dt} = -\frac{20\mu}{25\mu^2+16}z^3 + \frac{15\mu-16}{25\mu^2+16}z + \frac{25\mu^2\gamma_h - 20\mu\gamma_T}{25\mu^2+16}. \tag{B.1}$$

For the sake of simplicity the equation above has been written as

$$\frac{dz}{dt} = -a(\mu)\, z^3 + d(\mu)\, z + g(\mu), \tag{B.2}$$

with the obvious values of the parameters.

This stability analysis is carried out with a linear analysis of the behavior of the Eq. (B.1) around a fixed point $\bar{z}$. If

$$f(z) = -a\, z^3 + d\, z + g\,, \tag{B.3}$$

a fixed point for the deterministic system is defined to be one point $\bar{z}$ for which

$$f(\bar{z}) = 0\,. \tag{B.4}$$

This means that the time derivative of z around these kinds of points is zero, $\bar{z}$ is an equilibrium point. Expanding $f(z)$ around one of these points, ignoring terms more than linear order in z, gives

$$f(z) \approx f(\bar{z}) + \frac{df(z)}{dz}|_{z=\bar{z}}(z-\bar{z}) + \mathcal{O}(z-\bar{z})^2 \tag{B.5}$$

$$= \frac{df(z)}{dz}|_{z=\bar{z}}(z-\bar{z}) + \mathcal{O}(z-\bar{z})^2\,, \tag{B.6}$$

and then

$$\frac{dz}{dt} \approx \frac{df(z)}{dz}|_{z=\bar{z}}(z-\bar{z})\,. \tag{B.7}$$

The approximate solution should be

$$z \approx c\, e^{t\frac{df(z)}{dz}|_{z=\bar{z}}} + \bar{z}\,, \tag{B.8}$$

which shows that if $\frac{df(z)}{dz}|_{z=\bar{z}}$ is real and negative, or a complex quantity with negative real part, the fixed point $\bar{z}$ is a stable equilibrium point, while if the contrary occurs, the equilibrium point becomes unstable and the system grows indefinitely.

From Eq. (B.4), three solutions have been obtained. In Fig. B.1, it is shown the real part of these three fixed points. If the equilibrium point is complex, the real part is reported in red. Initially just one of the point is real, the other two are complex conjugate. Around $\mu \approx 1.14$ the solutions become different and real. In Fig. B.2 the values of $\frac{df(z)}{dz}|_{z=\bar{z}}$ computed for the different equilibrium points (the same marker is used for the fixed point and its derivative) are shown. After $\mu \approx 1.14$, the fixed point nearest to zero becomes unstable while the other two are stable.

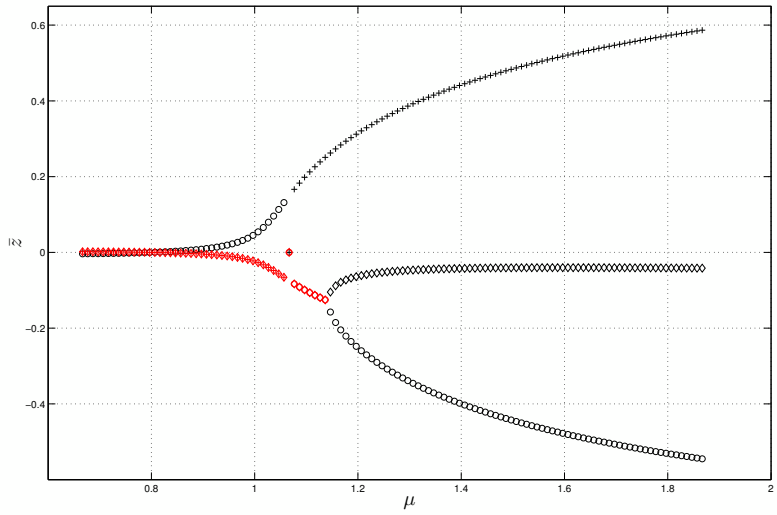

Figure B.1: Fixed point obtained by solving the third degree equation (B.4). Until $\mu \approx 1.14$ there is just one real solution; the other two are complex conjugate, for two values of μ these solutions cross the $\bar{z} = 0$ axis. Then arise three different real solutions. In red it is shown the real part of the two complex solutions. The three solutions are marked with the diamond, the cross and the circle.

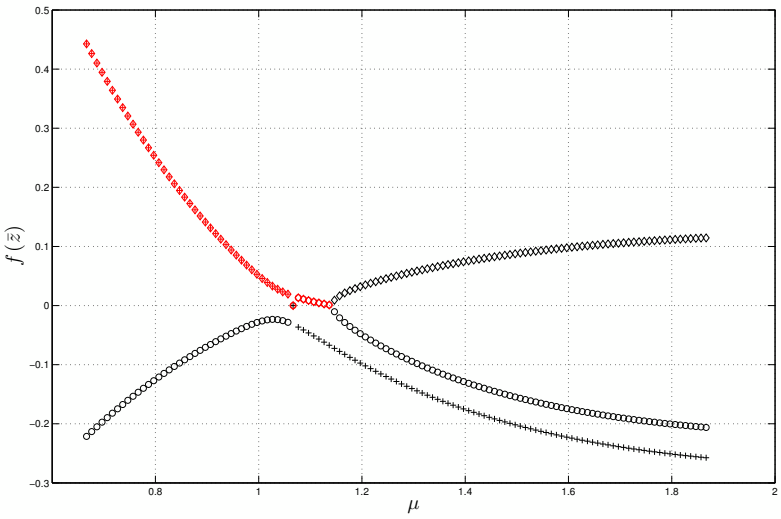

Figure B.2: $\frac{df(z)}{dz}|_{z=\bar{z}}$ computed for the different equilibrium points, the same marker is used for the fixed point and its derivative. After $\mu \approx 1.14$, the fixed point nearest to zero, denoted with the diamond in Fig. B.1, gives real positive derivative of f. This means that this point, when the coupling increases, becomes unstable while the other two, one positive (cross) and one negative (circle), become stable.

APPENDIX C

OBSERVED TRANSITION PROBABILITY MATRICES

Two seasons transition (Persistence):

$$\mathbb{W}^{12} = \begin{bmatrix} 0.52^{+0.04}_{-0.05} & 0.39^{+0.04}_{-0.04} & 0.09^{+0.03}_{-0.02} & 0.01^{+0.01}_{-0.01} \\ 0.13^{+0.04}_{-0.03} & 0.44^{+0.06}_{-0.05} & 0.38^{+0.05}_{-0.05} & 0.05^{+0.03}_{-0.02} \\ 0.05^{+0.03}_{-0.02} & 0.26^{+0.06}_{-0.05} & 0.60^{+0.06}_{-0.07} & 0.10^{+0.04}_{-0.03} \\ 0.02^{+0.02}_{-0.01} & 0.09^{+0.03}_{-0.03} & 0.23^{+0.04}_{-0.04} & 0.66^{+0.05}_{-0.05} \end{bmatrix} \quad \mathbb{W}^{23} = \begin{bmatrix} 0.43^{+0.06}_{-0.05} & 0.42^{+0.06}_{-0.05} & 0.13^{+0.04}_{-0.03} & 0.02^{+0.02}_{-0.01} \\ 0.20^{+0.04}_{-0.04} & 0.40^{+0.05}_{-0.05} & 0.29^{+0.05}_{-0.04} & 0.11^{+0.03}_{-0.03} \\ 0.06^{+0.03}_{-0.02} & 0.25^{+0.05}_{-0.04} & 0.44^{+0.05}_{-0.05} & 0.25^{+0.04}_{-0.04} \\ 0.09^{+0.04}_{-0.03} & 0.10^{+0.04}_{-0.03} & 0.23^{+0.05}_{-0.04} & 0.60^{+0.05}_{-0.06} \end{bmatrix}$$

$$\mathbb{W}^{34} = \begin{bmatrix} 0.85^{+0.04}_{-0.05} & 0.15^{+0.05}_{-0.04} & 0.00^{+0.01} & 0.00^{+0.01} \\ 0.42^{+0.05}_{-0.05} & 0.40^{+0.05}_{-0.05} & 0.17^{+0.04}_{-0.03} & 0.02^{+0.02}_{-0.01} \\ 0.10^{+0.03}_{-0.03} & 0.28^{+0.05}_{-0.04} & 0.30^{+0.05}_{-0.04} & 0.32^{+0.05}_{-0.04} \\ 0.02^{+0.02}_{-0.01} & 0.07^{+0.03}_{-0.02} & 0.22^{+0.05}_{-0.04} & 0.70^{+0.05}_{-0.05} \end{bmatrix} \quad \mathbb{W}^{41} = \begin{bmatrix} 0.79^{+0.04}_{-0.04} & 0.18^{+0.04}_{-0.03} & 0.03^{+0.02}_{-0.01} & 0.00^{+0.01} \\ 0.33^{+0.05}_{-0.05} & 0.47^{+0.05}_{-0.05} & 0.17^{+0.04}_{-0.04} & 0.03^{+0.02}_{-0.02} \\ 0.06^{+0.03}_{-0.02} & 0.28^{+0.06}_{-0.05} & 0.42^{+0.06}_{-0.06} & 0.24^{+0.05}_{-0.05} \\ 0.00^{+0.01} & 0.01^{+0.02}_{-0.01} & 0.11^{+0.04}_{-0.03} & 0.87^{+0.03}_{-0.04} \end{bmatrix}$$

These are the two-seasons transition probability matrices computed for the observed NINO3.4 series of 159 years. The confidence level used to find the error is $CL = 95\%$.

Three seasons transition:

$$\mathbb{W}^{13} = \begin{bmatrix} 0.26^{+0.04}_{-0.04} & 0.37^{+0.04}_{-0.04} & 0.24^{+0.04}_{-0.04} & 0.13^{+0.03}_{-0.03} \\ 0.16^{+0.04}_{-0.04} & 0.33^{+0.05}_{-0.05} & 0.34^{+0.05}_{-0.05} & 0.18^{+0.04}_{-0.04} \\ 0.12^{+0.05}_{-0.04} & 0.25^{+0.06}_{-0.05} & 0.40^{+0.07}_{-0.06} & 0.24^{+0.06}_{-0.05} \\ 0.16^{+0.04}_{-0.03} & 0.21^{+0.04}_{-0.04} & 0.24^{+0.04}_{-0.04} & 0.40^{+0.05}_{-0.05} \end{bmatrix} \quad \mathbb{W}^{24} = \begin{bmatrix} 0.57^{+0.05}_{-0.06} & 0.28^{+0.05}_{-0.05} & 0.08^{+0.03}_{-0.03} & 0.07^{+0.03}_{-0.02} \\ 0.33^{+0.05}_{-0.04} & 0.27^{+0.04}_{-0.04} & 0.17^{+0.04}_{-0.03} & 0.22^{+0.04}_{-0.04} \\ 0.19^{+0.04}_{-0.04} & 0.22^{+0.04}_{-0.04} & 0.25^{+0.05}_{-0.04} & 0.36^{+0.05}_{-0.05} \\ 0.20^{+0.05}_{-0.04} & 0.18^{+0.05}_{-0.04} & 0.23^{+0.05}_{-0.04} & 0.39^{+0.06}_{-0.05} \end{bmatrix}$$

$$\mathbb{W}^{31} = \begin{bmatrix} 0.73^{+0.05}_{-0.06} & 0.22^{+0.05}_{-0.05} & 0.04^{+0.03}_{-0.02} & 0.00^{+0.01} \\ 0.50^{+0.05}_{-0.05} & 0.27^{+0.04}_{-0.04} & 0.15^{+0.04}_{-0.03} & 0.08^{+0.03}_{-0.02} \\ 0.16^{+0.04}_{-0.03} & 0.24^{+0.04}_{-0.04} & 0.24^{+0.04}_{-0.04} & 0.36^{+0.05}_{-0.05} \\ 0.05^{+0.03}_{-0.02} & 0.13^{+0.04}_{-0.03} & 0.15^{+0.04}_{-0.04} & 0.67^{+0.05}_{-0.05} \end{bmatrix} \quad \mathbb{W}^{42} = \begin{bmatrix} 0.48^{+0.05}_{-0.05} & 0.38^{+0.05}_{-0.04} & 0.11^{+0.03}_{-0.03} & 0.03^{+0.02}_{-0.01} \\ 0.19^{+0.04}_{-0.04} & 0.35^{+0.05}_{-0.05} & 0.37^{+0.05}_{-0.05} & 0.09^{+0.03}_{-0.03} \\ 0.07^{+0.04}_{-0.03} & 0.29^{+0.06}_{-0.05} & 0.45^{+0.06}_{-0.06} & 0.19^{+0.05}_{-0.04} \\ 0.02^{+0.02}_{-0.01} & 0.13^{+0.04}_{-0.03} & 0.27^{+0.05}_{-0.04} & 0.57^{+0.05}_{-0.05} \end{bmatrix}$$

These are the three-seasons transition probability matrices computed for the observed NINO3.4 series of 159 years. The confidence level used to find the error is $CL = 95\%$.

Four seasons transition:

$$\mathbb{W}^{14} = \begin{bmatrix} 0.39^{+0.04}_{-0.04} & 0.28^{+0.04}_{-0.04} & 0.10^{+0.03}_{-0.02} & 0.23^{+0.04}_{-0.04} \\ 0.26^{+0.05}_{-0.05} & 0.27^{+0.05}_{-0.05} & 0.23^{+0.05}_{-0.04} & 0.24^{+0.05}_{-0.04} \\ 0.19^{+0.05}_{-0.05} & 0.19^{+0.05}_{-0.05} & 0.31^{+0.06}_{-0.06} & 0.32^{+0.06}_{-0.06} \\ 0.34^{+0.05}_{-0.05} & 0.19^{+0.04}_{-0.04} & 0.19^{+0.04}_{-0.04} & 0.27^{+0.05}_{-0.04} \end{bmatrix} \quad \mathbb{W}^{21} = \begin{bmatrix} 0.55^{+0.06}_{-0.06} & 0.26^{+0.05}_{-0.05} & 0.08^{+0.03}_{-0.03} & 0.11^{+0.04}_{-0.03} \\ 0.41^{+0.05}_{-0.05} & 0.19^{+0.04}_{-0.04} & 0.14^{+0.04}_{-0.03} & 0.26^{+0.04}_{-0.04} \\ 0.17^{+0.04}_{-0.04} & 0.27^{+0.05}_{-0.04} & 0.21^{+0.04}_{-0.04} & 0.34^{+0.05}_{-0.05} \\ 0.25^{+0.05}_{-0.05} & 0.18^{+0.05}_{-0.04} & 0.18^{+0.05}_{-0.04} & 0.39^{+0.06}_{-0.05} \end{bmatrix}$$

$$\mathbb{W}^{32} = \begin{bmatrix} 0.49^{+0.06}_{-0.06} & 0.38^{+0.06}_{-0.06} & 0.08^{+0.04}_{-0.03} & 0.05^{+0.03}_{-0.02} \\ 0.29^{+0.04}_{-0.04} & 0.32^{+0.05}_{-0.04} & 0.28^{+0.04}_{-0.04} & 0.12^{+0.03}_{-0.03} \\ 0.07^{+0.03}_{-0.02} & 0.29^{+0.05}_{-0.04} & 0.43^{+0.05}_{-0.05} & 0.21^{+0.04}_{-0.04} \\ 0.08^{+0.03}_{-0.03} & 0.21^{+0.05}_{-0.04} & 0.25^{+0.05}_{-0.04} & 0.46^{+0.05}_{-0.05} \end{bmatrix} \quad \mathbb{W}^{43} = \begin{bmatrix} 0.25^{+0.04}_{-0.04} & 0.40^{+0.05}_{-0.04} & 0.23^{+0.04}_{-0.04} & 0.13^{+0.03}_{-0.03} \\ 0.13^{+0.04}_{-0.03} & 0.25^{+0.05}_{-0.04} & 0.38^{+0.05}_{-0.05} & 0.24^{+0.05}_{-0.04} \\ 0.14^{+0.05}_{-0.04} & 0.27^{+0.06}_{-0.05} & 0.36^{+0.06}_{-0.06} & 0.23^{+0.05}_{-0.05} \\ 0.20^{+0.04}_{-0.04} & 0.23^{+0.05}_{-0.04} & 0.23^{+0.05}_{-0.04} & 0.34^{+0.05}_{-0.05} \end{bmatrix}$$

These are the four-seasons transition probability matrices computed for the observed NINO3.4 series of 159 years. The confidence level used to find the error is $CL = 95\%$.

One year probability transition matrices:

$$\mathbb{W}^{11} = \begin{bmatrix} 0.55^{+0.04}_{-0.05} & 0.22^{+0.04}_{-0.04} & 0.05^{+0.02}_{-0.02} & 0.18^{+0.04}_{-0.03} \\ 0.27^{+0.05}_{-0.05} & 0.33^{+0.05}_{-0.05} & 0.22^{+0.05}_{-0.04} & 0.17^{+0.04}_{-0.04} \\ 0.16^{+0.05}_{-0.04} & 0.22^{+0.06}_{-0.05} & 0.35^{+0.06}_{-0.06} & 0.28^{+0.06}_{-0.06} \\ 0.24^{+0.04}_{-0.04} & 0.14^{+0.04}_{-0.03} & 0.13^{+0.04}_{-0.03} & 0.49^{+0.05}_{-0.05} \end{bmatrix} \quad \mathbb{W}^{22} = \begin{bmatrix} 0.44^{+0.06}_{-0.06} & 0.40^{+0.06}_{-0.05} & 0.10^{+0.04}_{-0.03} & 0.06^{+0.03}_{-0.02} \\ 0.23^{+0.04}_{-0.04} & 0.37^{+0.05}_{-0.05} & 0.24^{+0.04}_{-0.04} & 0.16^{+0.04}_{-0.03} \\ 0.10^{+0.03}_{-0.03} & 0.24^{+0.04}_{-0.04} & 0.47^{+0.05}_{-0.05} & 0.19^{+0.04}_{-0.04} \\ 0.12^{+0.04}_{-0.03} & 0.15^{+0.04}_{-0.04} & 0.25^{+0.05}_{-0.05} & 0.48^{+0.06}_{-0.06} \end{bmatrix}$$

$$\mathbb{W}^{33} = \begin{bmatrix} 0.37^{+0.06}_{-0.06} & 0.36^{+0.06}_{-0.06} & 0.18^{+0.05}_{-0.04} & 0.08^{+0.04}_{-0.03} \\ 0.20^{+0.04}_{-0.04} & 0.39^{+0.05}_{-0.05} & 0.27^{+0.04}_{-0.04} & 0.13^{+0.04}_{-0.03} \\ 0.09^{+0.03}_{-0.02} & 0.24^{+0.04}_{-0.04} & 0.41^{+0.05}_{-0.05} & 0.26^{+0.04}_{-0.04} \\ 0.14^{+0.04}_{-0.03} & 0.18^{+0.04}_{-0.04} & 0.25^{+0.05}_{-0.04} & 0.43^{+0.05}_{-0.05} \end{bmatrix} \quad \mathbb{W}^{44} = \begin{bmatrix} 0.53^{+0.05}_{-0.05} & 0.26^{+0.04}_{-0.04} & 0.09^{+0.03}_{-0.02} & 0.12^{+0.03}_{-0.03} \\ 0.25^{+0.05}_{-0.04} & 0.31^{+0.05}_{-0.05} & 0.21^{+0.05}_{-0.04} & 0.23^{+0.05}_{-0.04} \\ 0.13^{+0.04}_{-0.04} & 0.26^{+0.06}_{-0.05} & 0.35^{+0.06}_{-0.06} & 0.26^{+0.06}_{-0.05} \\ 0.25^{+0.05}_{-0.04} & 0.13^{+0.04}_{-0.03} & 0.17^{+0.04}_{-0.04} & 0.45^{+0.05}_{-0.05} \end{bmatrix}$$

These are the one-year transition probability matrices computed for the observed NINO3.4 series of 159 years. The confidence level used to find the error is $CL = 95\%$.

BIBLIOGRAPHY

An, S.-I., Y.-G. Ham, J.-S. Kug, F.-F. Jin, and I.-S. Kang, 2005: El niño–la niña asymmetry in the coupled model intercomparison project simulations*. *Journal of Climate*, **18 (14)**, 2617–2627, doi:10.1175/JCLI3433.1, URL http://dx.doi.org/10.1175/JCLI3433.1.

An, S.-I. and F.-F. Jin, 2004: Nonlinearity and asymmetry of enso*. *Journal of Climate*, **17 (12)**, 2399–2412, doi:10.1175/1520-0442(2004)017<2399:NAAOE>2.0.CO;2, URL http://dx.doi.org/10.1175/1520-0442(2004)017<2399:NAAOE>2.0.CO;2.

Battisti, D. S. and A. C. Hirst, 1989: Interannual variability in a tropical atmosphere–ocean model: Influence of the basic state, ocean geometry and nonlinearity. *Journal of the Atmospheric Sciences*, **46 (12)**, 1687–1712, doi:10.1175/1520-0469(1989)046<1687:IVIATA>2.0.CO;2, URL http://dx.doi.org/10.1175/1520-0469(1989)046<1687:IVIATA>2.0.CO;2.

Berner, J., 2005: Linking nonlinearity and non-gaussianity of planetary wave behavior by the fokker-planck equation. *J. Atmos. Sci.*, **62**, 2098–2117.

Bjerknes, J., 1969: Atmospheric teleconnections from the equatorial pacific. *Mon. Wea. Rev.*, **97**, 163–172.

Boutle, I., R. H. . S. Taylor, and R. A. Römer, 2007: El niño and the delayed action oscillator. *Am. J. Phys..*, **75 (15)**.

Brown, J. N. and A. V. Fedorov, 2010: How much energy is transferred from the winds to the thermocline on enso time scales? *Journal of Climate*, **23 (6)**, 1563–1580, doi:10.1175/2009JCLI2914.1, URL http://dx.doi.org/10.1175/2009JCLI2914.1.

Burgers, G., F.-F. Jin, and G. J. van Oldenborgh, 2005: The simplest enso recharge oscillator. *Geophys. Res. Lett.*, **32**.

Burgers, G. and D. Stephenson, 1999: The "normality" of el nino. *Geophysical Research Letters*, **26 (8)**, 1027–1030.

Cane, M. and S. Zebiak, 1985: A theory for el nino and the southern oscillation. *Science*, **228**, 1085–1087.

Cane, M. A., S. E. Zebiak, and S. C. Dolan, 1986: Experimental forecasts of el nino. *Nature*, **321 (6073)**, 827–832, URL http://dx.doi.org/10.1038/321827a0.

Chang, P., L. Ji, H. Li, and M. Flugel, 1996: Chaotic dynamic versus stochastic processes in enso in coupled ocean- atmosphere models. *Physica D*, **9**, 301–320.

Choi, K.-Y. and G. Vecchi, 2012: Yet another mechanism for enso asymmetry. *in preparation*.

Davini, P., C. Cagnazzo, P. G. Fogli, E. Manzini, S. Gualdi, and A. Navarra, 2013: European blocking and atlantic jet stream variability in the ncep/ncar reanalysis and the cmcc-cms climate model. *Clim. Dyn.*

DelSole, T., 2001: A simple model for transient eddy momentum fluxes in the upper troposphere. *Journal of the Atmospheric Sciences*, **58 (20)**, 3019–3035, doi:10.1175/1520-0469(2001)058<3019:ASMFTE>2.0.CO;2.

Duane, G. and J. Tribbia, 2004: Weak Atlantic-Pacific teleconnections as synchronized chaos. *Journal of the Atmospheric Sciences*, **61 (17)**, 2149–2168.

Epstein, E. S., 1969: The role of initial uncertainties in prediction. *Journal of Applied Meteorology*, **8 (2)**, 190–198.

Farrell, B. F. and P. J. Ioannou, 1995: Stochastic dynamics of the midlatitude atmospheric jet. *Journal of the Atmospheric Sciences*, **52 (10)**, 1642–1656.

Fedorov, A. V., S. L. Harper, S. G. Philander, B. Winter, and A. Wittenberg, 2003: How predictable is el niño? *Bulletin of the American Meteorological Society*, **84 (7)**, 911–919, doi:10.1175/BAMS-84-7-911, URL http://dx.doi.org/10.1175/BAMS-84-7-911.

Fraedrich, K., 1988: El niño/southern oscillation predictability. *Mon. Wea. Rev.*

Galanti, E. and E. Tziperman, 2000: Enso's phase locking to the seasonal cycle in the fast-sst, fast-wave, and mixed-mode regimes. *Journal of the Atmospheric Sciences*.

Gritsun, A. and G. Branstator, 2007: Climate response using a three-dimensional operator based on the fluctuation–dissipation theorem. *Journal of the Atmospheric Sciences*, **64 (7)**, 2558–2575, doi:10.1175/JAS3943.1.

Gualdi, S., E. Guilyardi, P. Delecluse, S. Masina, and A. Navarra, 2003: The role of the indian ocean in a coupled model. *Climate Dynamics*, **20**, 567–582.

Gualdi, S., A. Navarra, and H. von Storch, 1997: Tropical intraseasonal oscillation appearing in operational analyses and in a family of general circulation models. *J. Atmos. Sci.*, **54**, 1185–1202.

Haken, H., 1976: Generalized onsager-machlup funtion and classes of path integral of the fokker-planck equation and the master equation. *Z. Physil*, **24**, 321–326.

Hasselmann, K., 1976: Stochastic climate models. part i: Theory. *Tellus*, **28**, 473–485.

Hendon, H. H., M. C. Wheeler, and C. Zhang, 2007: Seasonal dependence of the mjo–enso relationship. *Journal of Climate*, **20 (3)**, 531–543, doi:10.1175/JCLI4003.1, URL http://dx.doi.org/10.1175/JCLI4003.1.

Hochberg, D., C. Molina-Paris, J. Perez-Mercader, and M. Visser, 1999: Effective action for stochastic partial differential equations. *Physical Review E*, **60 (6, Part A)**, 6343–6360.

Hochberg, D., C. Molina-Parisc, J. Perez-Mercaderb, and M. Visserd, 2000a: Effective potential for the massless kpz equation. *PHYSICA A-STATISTICAL MECHANICS AND ITS APPLICATIONS*.

Hochberg, D., C. Molina-Parisc, J. Perez-Mercaderb, and M. Visserd, 2000b: Effective potential for the reaction-diffusion-decay system. *J. Statist. Phys.*

Jin, F. F., 1996: Tropical ocean-atmosphere interaction, the pacific cold tongue, and the el niño-southern oscillation. *Science*, **274 (5284)**, 76–78, doi:10.1126/science.274.5284.76, URL http://www.sciencemag.org/content/274/5284/76.abstract, http://www.sciencemag.org/content/274/5284/76.full.pdf.

Jin, F. F., 1997a: An equatorial ocean recharge paradigm for enso. part i: Conceptual model. *J Atmosph Sci*, **54**, 811–829.

Jin, F.-F., 1997b: An equatorial ocean recharge paradigm for enso. part ii: Stripped-down coupled model. *Journal of the Atmospheric Sciences*.

Jin, F.-F., S.-I. An, A. Timmermann, and J. Zhao, 2003: Strong el niòo events and nonlinear dynamical heating. *Geophys. Res. Lett.*, **30 (3)**, 1120, doi:10.1029/2002GL016356, URL http://dx.doi.org/10.1029/2002GL016356.

Jin, F.-F. and J. D. Neelin, 1993: Modes of interannual tropical ocean–atmosphere interaction—a unified view. part i: Numerical results. *Journal of the Atmospheric Sciences*, **50 (21)**, 3477–3503, doi:10.1175/1520-0469(1993)050<3477:MOITOI>2.0.CO;2, URL http://dx.doi.org/10.1175/1520-0469(1993)050<3477:MOITOI>2.0.CO;2.

Jin, F.-F., J. D. Neelin, and M. Ghil, 1994a: El niño on the devil's staircase: Annual subharmonic steps to chaos. *Science*, 70–72.

Jin, F.-F., J. D. Neelin, and M. Ghil, 1994b: El niño on the devil's staircase: Annual subharmonic steps to chaos. *Science*, **264 (5155)**, 70–72, doi:10.1126/science.264.5155.70, URL http://www.sciencemag.org/content/264/5155/70.abstract, http://www.sciencemag.org/content/264/5155/70.full.pdf.

Jin, F.-F., J. D. Neelin, and M. Ghil, 1996: El niño/southern oscillation and the annual cycle: subharmonic frequency locking and aperiodicity. *Physica D*, **98**, 442–465.

Kang, I.-S. and J.-S. Kug, 2002: El niño–la niña sea surface temperature anomalies: Asymmetry characteristics associated with their wind stress anomalies. *J. Geophys. Res.*, **107 (D19)**, 4372, doi:10.1029/2001JD000393, URL http://dx.doi.org/10.1029/2001JD000393.

Kaplan, A., M. Cane, Y. Kushnir, A. Clement, M. Blumenthal, and B. Rajagopalan, 1998: Analyses of global sea surface temperature 1856-1991. *J. Geophys. Res.*

Kapur, A., C. Zhang, J. Zavala-Grey, and H. Hendon, 2012: Role of stochastic forcing in enso in observations and a coupled gcm. *Clim. Dyn.*, **38**, 87–107.

Kleeman, R., 2010: Stochastic theories for the irregularity of the enso. *Stochastic Physics and Climate Modelling*, T. Palmer and P. Williams, Eds., Cambridge University Press.

Kravtsov, S., D. Kondrashov, and M. Ghil, 2005: Multilevel regression modeling of nonlinear processes: Derivation and applications to climatic variability. *Journal of Climate*, **18 (21)**, 4404–4424, doi:10.1175/JCLI3544.1, URL `http://journals.ametsoc.org/doi/abs/10.1175/JCLI3544.1`, `http://journals.ametsoc.org/doi/pdf/10.1175/JCLI3544.1`.

Leith, C. E., 1974: Theoretical skill of monte carlo forecasts. *Monthly Weather Review*, **102 (6)**, 409–418.

Lengaigne, M., E. Guilyardi, J.-P. Boulanger, C. Menkes, P. Delecluse, P. Inness, J. Cole, and J. Slingo, 2004: Triggering of el niño by westerly wind events in a coupled general circulation model. *Climate Dynamics*, **23**, 601–620, URL `http://dx.doi.org/10.1007/s00382-004-0457-2`, 10.1007/s00382-004-0457-2.

Levine, A. F. Z. and M. J. McPhaden, 2015: The annual cycle in enso growth rate as a cause of the spring predictability barrier. *Geophys. Res. Lett.*

Lorenz, E. N., 1963: Deterministic nonperiodic flow. *Journal of the Atmospheric Sciences*, **20 (2)**, 130–141.

Lorenz, E. N., 1969: Atmospheric predictability as revealed by naturally occuring analogues. *Journal of the Atmospheric Sciences*.

Lorenz, E. N., 1984: Some aspects of atmospheric predictability. *Problems and prospects in long and medium-range weather forecasting*.

Lorenz, E. N., 1987: Deterministic and stochastic aspects of atmospheric dynamics. *Irreversible phenomena and dinamical systems analysis in geosciences*.

Madden, R. A. and P. R. Julian, 1971a: Detection of a 40–50 day oscillation in the zonal wind in the tropical pacific. *Journal of the Atmospheric Sciences*, **28 (5)**, 702–708, doi:10.1175/1520-0469(1971)028<0702:DOADOI>2.0.CO;2, URL `http://dx.doi.org/10.1175/1520-0469(1971)028<0702:DOADOI>2.0.CO;2`.

Madden, R. A. and P. R. Julian, 1971b: Detection of a 40-50 day oscillation in the zonal wind in the tropical pacific. *Journal of the Atmospheric Sciences*.

Majda, A., A., I. Timofeyev, and E. Vanden-Eijnden, 2006: Stochastic models for selected slow variables in large deterministic systems. *Nonlinearity*, **19**, 769–794.

Martin, P. C., E. D. Siggia, and H. A. Rose, 1973: Statistical dynamics of classical systems. *Phys. Rev. A*, **8**, 423–437.

McPhaden, M. and X. Yu, 1999: Equatorial waves and the 1997-98 el niño. *Geophys. Res. Lett.*, **26**, 2961–64.

Meehl, G. A., et al., 2009: Decadal prediction, can it be skillful? *Amer. Meteor. Soc.*

Miyakoda, K., T. G. Gordon, R. Caverly, W. Stern, J. Siutis, and W. Bourke, 1983: Simulation of a blocking event in january 1977. *Mon. Wea. Rev*.

Monahan, A. H. and A. Dai, 2004: The spatial and temporal structure of enso nonlinearity. *Journal of Climate*, **17 (15)**, 3026–3036, doi:10.1175/1520-0442(2004)017<3026:TSATSO>2.0.CO;2, URL http://dx.doi.org/10.1175/1520-0442(2004)017<3026:TSATSO>2.0.CO;2.

Moore, A. M. and R. Kleeman, 1999a: The nonnormal nature of el niño and intraseasonal variability. *Journal of Climate*, **12 (10)**, 2965–2982, doi:10.1175/1520-0442(1999)012<2965:TNNOEN>2.0.CO;2, URL http://dx.doi.org/10.1175/1520-0442(1999)012<2965:TNNOEN>2.0.CO;2.

Moore, A. M. and R. Kleeman, 1999b: Stochastic forcing of enso by the intraseasonal oscillation. *Journal of Climate*, **12 (5)**, 1199–1220, doi:10.1175/1520-0442(1999)012<1199:SFOEBT>2.0.CO;2, URL http://dx.doi.org/10.1175/1520-0442(1999)012<1199:SFOEBT>2.0.CO;2.

Munnich, M., M. Cane, and S. E. Zebiak, 1990: A study of self-excited oscillations of the tropical ocean-atmosphere system. partii: Nonlinear cases. *J. Atmos. Sci.*, **48 (10)**, 1238–1248.

Navarra, A., J. Tribbia, and G. Conti, 2012: The path integral formulation of climate dynamics. Tech. Rep. RP130, Centro Euromediterraneo sui Cambiamenti Climatici.

Navarra, A., J. Tribbia, and G. Conti, 2013a: Atmosphere–ocean interactions at strong couplings in a simple model of el niño. *J. Climate*, **26**, 9633–9654.

Navarra, A., J. Tribbia, and G. Conti, 2013b: The path integral formulation of climate dynamics. *Plos One*.

Navarra, A., et al., 2008: Atmospheric horizontal resolution affects tropical climate variability in coupled models. *Journal of Climate*, **21 (4)**, 730–750, doi:10.1175/2007JCLI1406.1, URL http://dx.doi.org/10.1175/2007JCLI1406.1.

Neale, R. B., J. H. Richter, and M. Jochum, 2008: The impact of convection on enso: From a delayed oscillator to a series of events. *Journal of Climate*, **21 (22)**, 5904–5924, doi:10.1175/2008JCLI2244.1, URL http://dx.doi.org/10.1175/2008JCLI2244.1.

Neelin, J. D., D. S. Battisti, A. C. Hirst, F.-F. Jin, Y. Wakata, T. Yamagata, and S. E. Zebiak, 1998: Enso theory. *J. Geophys. Res.*, **103 (C7)**, 14 261–14 290, doi:10.1029/97JC03424, URL http://dx.doi.org/10.1029/97JC03424.

Neelin, J. D., M. Latif, and F. Jin, 1994: Dynamics of coupled ocean-atmosphere models: The tropical problem. *Annual Review of Fluid Mechanics*, **26 (1)**, 617–659, doi:10.1146/annurev.fl.26.010194.003153, URL http://dx.doi.org/10.1146/annurev.fl.26.010194.003153.

Nicolis, C., 1990: Chaotic dynamics, markov processes and climate predictability. *Tellus*.

Pedlosky, J., 1996: *Ocean Circulation Theory*. Springer.

Penland, C., 1996: A stochastic model of indopacific sea surface temperature anomalies. *Physica D*, **98**, 534–558.

Penland, C., 2003: Noise out of chaos and why it won't go away. *Bulletin of the American Meteorological Society*, **84 (7)**, 921–925, doi:10.1175/BAMS-84-7-921.

Penland, C. and P. D. Sardeshmukh, 1995: The optimal growth of tropical sea surface temperature anomalies. *Journal of Climate*, **8 (8)**, 1999–2024, doi:10.1175/1520-0442(1995)008<1999:TOGOTS>2.0.CO;2, URL http://dx.doi.org/10.1175/1520-0442(1995)008<1999:TOGOTS>2.0.CO;2.

Philander, S. and A. V. Fedorov, 2003: Is el niño sporadic or cyclic? *Ann. Rev. of Earth and Planetary Sciences*, **31**, 579–594.

Philander, S. G. H., 1990: *El Niño, La Niña, and the Southern Oscillation*. Academic Press, 293 pp.

Picaut, J., F. Masia, and Y. du Penhoat, 1997: An advective-reflective conceptual model for the oscillatory nature of the enso. *Science*, **277 (5326)**, 663–666, doi: 10.1126/science.277.5326.663, URL `http://www.sciencemag.org/content/277/5326/663.abstract`, `http://www.sciencemag.org/content/277/5326/663.full.pdf`.

Pinardi, N., A. Bonazzi, E. Scoccimarro, S. Dobricic, A. Navarra, A. Ghiselli, and P. Veronesi, 2008: Very large ensemble ocean forecasting experiment using the grid computing infrastructure. *Bulletin of the American Meteorological Society*, **89 (6)**, 799–804.

Rayner, N. A., D. E. Parker, E. B. Horton, C. K. Folland, L. V. Alexander, D. P. Rowell, E. C. Kent, and A. Kaplan, 2003: Global analyses of sea surface temperature, sea ice, and night marine air temperature since the late nineteenth century. *J. Geophys. Res.*, **108**, 4407.

Risken, H., 1989: *The Fokker-Planck equation*. Springer, New York.

Rodwell, M. J. and F. J. Doblas-Reyes, 2006: Medium-range, monthly, and seasonal prediction for europe and the use of forecast information. *Journal of Climate*, **19 (23)**, 6025–6046.

Rotondi, A., P. Pedroni, and A. Pievatolo, 2001: *Probabilità Statistica e Simulazione*. Springer.

Schneider, E. K. and M. Fan, 2007: Weather noise forcing of surface climate variability. *Journal of the Atmospheric Sciences*, **64 (9)**, 3265–3280.

Schopf, P. and M. J. Suarez, 1988: Vacillations in a coupled ocean-atmosphere model. *J. Atmos. Sci.*, **45**, 549–566.

Shukla, J., 1981: Dynamical predictability of monthly means. *Journal of the Atmospheric Sciences*.

Shukla, J., 1985: Predictability. *Advances in Geophysics*.

Sperber, K., S. Gualdi, S. Legutke, and V. Gayler, 2005: The madden–julian oscillation in echam4 coupled and uncoupled general circulation models. *Climate Dynamics*, **25**, 117–140, URL http://dx.doi.org/10.1007/s00382-005-0026-3, 10.1007/s00382-005-0026-3.

Srinivasan, K. and W. R. Young, 2012: Zonostrophic instability. *J. Atmos. Sci.*

Stein, K., N. Schneider, and F.-F. Jin, 2010: Seasonal synchronization of enso events in a linear stochastic model. *J. Clim.*

Stern, W. and K. Miyakoda, 1995: Feasibility of seasonal forecasts inferred from multiple gcm simulations. *J. Climate*, **8**, 1071–1085.

Stewart, W. J., 2009: *Probability, Markov Chains, Queues, and Simulation: The Mathematical Basis of Performance Modeling*. Princeton University Press.

Stone, L., P. I. Saparin, A. Huppert, and C. Price, 1998: El niño chaos: The role of noise and stochastic resonance on the enso cycle. *Geophys. Res. Lett.*, **25**, 175–178.

Suarez, M. J. and P. S. Schopf, 1988: A delayed action oscillator for enso. *J. Atmos. Sci.*, **45**, 3283–3287.

Subramanian, A. C., M. Jochum, A. J. Miller, R. Murtugudde, R. B. Neale, and D. E. Waliser, 2011: The madden–julian oscillation in ccsm4. *Journal of Climate*, **24 (24)**, 6261–6282, doi:10.1175/JCLI-D-11-00031.1, URL http://dx.doi.org/10.1175/JCLI-D-11-00031.1.

Sura, P. and M. Newman, 2008: The impact of rapid wind variability upon air–sea thermal coupling. *Journal of Climate*, **21 (4)**, 621–637, doi:10.1175/2007JCLI1708.1.

Sura, P., M. Newman, C. Penland, and P. Sardeshmukh, 2005: Multiplicative noise and non-gaussianity: A paradigm for atmospheric regimes? *Journal of the Atmospheric Sciences*, **62 (5)**, 1391–1409, doi:10.1175/JAS3408.1, URL http://journals.ametsoc.org/doi/abs/10.1175/JAS3408.1, http://journals.ametsoc.org/doi/pdf/10.1175/JAS3408.1.

Thompson, C. J. and D. S. Battisti, 2000: A linear stochastic dynamical model of enso. part i: Model development. *Journal of Climate*, **13 (15)**, 2818–2832, doi:10.

1175/1520-0442(2000)013<2818:ALSDMO>2.0.CO;2, URL http://dx.doi.org/10.1175/1520-0442(2000)013<2818:ALSDMO>2.0.CO;2.

Thompson, C. J. and D. S. Battisti, 2001: A linear stochastic dynamical model of enso. part ii: Analysis. *Journal of Climate*, **14 (4)**, 445–466, doi:10.1175/1520-0442(2001)014<0445:ALSDMO>2.0.CO;2, URL http://dx.doi.org/10.1175/1520-0442(2001)014<0445:ALSDMO>2.0.CO;2.

Timmermann, A., F.-F. Jin, and J. Abshagen, 2003: A nonlinear theory for el niño bursting. *Journal of the Atmospheric Sciences*, **60 (1)**, 152–165, doi:10.1175/1520-0469(2003)060<0152:ANTFEN>2.0.CO;2, URL http://dx.doi.org/10.1175/1520-0469(2003)060<0152:ANTFEN>2.0.CO;2.

Toth, Z. and E. Kalnay, 1993: Ensemble forecasting at nmc: The generation of perturbations. *Bulletin of the American Meteorological Society*, **74 (12)**, 2317–2330.

Tziperman, E., L. Stone, M. Cane, and H. Jarosh, 1994a: El niño chaos: Overlapping of resonances between the seasonal cycle and the pacific ocean-atmosphere oscillator. *Science*, 72–74.

Tziperman, E., L. Stone, M. A. Cane, and H. Jarosh, 1994b: El niño chaos: Overlapping of resonances between the seasonal cycle and the pacific ocean-atmosphere oscillator. *Science*, **264 (5155)**, 72–74, doi:10.1126/science.264.5155.72, URL http://www.sciencemag.org/content/264/5155/72.abstract, http://www.sciencemag.org/content/264/5155/72.full.pdf.

Wang, C., 2001: A unified oscillator model for the el niño–southern oscillation. *Journal of Climate*, **14 (1)**, 98–115, doi:10.1175/1520-0442(2001)014<0098:AUOMFT>2.0.CO;2, URL http://dx.doi.org/10.1175/1520-0442(2001)014<0098:AUOMFT>2.0.CO;2.

Wang, C., C. Deser, J. Yu, P. DiNezio, and A. Clement, 2012: El niño and southern oscillation (enso): A review. *Coral Reefs of the Eastern Pacific*, 3–19.

Wang, W. and M. J. McPhaden, 2000: The surface-layer heat balance in the equatorial pacific ocean. part ii: Interannual variability*. *Journal of Physical Oceanography*, **30 (11)**, 2989–3008, doi:10.1175/1520-0485(2001)031<2989:TSLHBI>2.0.CO;2,

URL http://dx.doi.org/10.1175/1520-0485(2001)031<2989:TSLHBI>2.0.CO;2.

Webster, P. J., 1995: The annual cycle and the predictability of the tropical coupled ocean-atmosphere system. *Meteor. Atmos. Phys.*

Webster, P. J. and S. Yang, 1992: Monsoon and enso: Selectively interactive system. *Quart. J. Roy. Meteor. Soc.*

Zavala-Garay, J., C. Zhang, A. M. Moore, A. T. Wittenberg, M. J. Harrison, A. Rosati, J. Vialard, and R. Kleeman, 2008: Sensitivity of hybrid enso models to unresolved atmospheric variability. *Journal of Climate*, **21 (15)**, 3704–3721, doi:10.1175/2007JCLI1188.1, URL http://dx.doi.org/10.1175/2007JCLI1188.1.

Zebiak, S. E. and M. A. Cane, 1987: A model el niño–southern oscillation. *Monthly Weather Review*, **115 (10)**, 2262–2278, doi:10.1175/1520-0493(1987)115<2262:AMENO>2.0.CO;2, URL http://dx.doi.org/10.1175/1520-0493(1987)115<2262:AMENO>2.0.CO;2.

Zhang, C., 2001: Intraseasonal perturbations in sea surface temperatures of the equatorial eastern pacific and their association with the madden–julian oscillation*. *Journal of Climate*, **14 (6)**, 1309–1322.

Zhang, C. and J. Gottschalck, 2002: Sst anomalies of enso and the madden–julian oscillation in the equatorial pacific*. *Journal of Climate*, **15 (17)**, 2429–2445, doi:10.1175/1520-0442(2002)015<2429:SAOEAT>2.0.CO;2, URL http://dx.doi.org/10.1175/1520-0442(2002)015<2429:SAOEAT>2.0.CO;2.

Zinn-Justin, J., 1993: *Quantum field theory and critical phenomena*. 2d ed., Oxford University Press.